FINAL REPORT

Determining Detection and Classification Potential of Munitions using Advanced EMI Sensors in the Underwater Environment

SERDP Project MR-2412

NOVEMBER 2016

Stephen Billings
Black Tusk Geophysics Inc.

Lin-Ping Song
The University of British Columbia

SERDP
DOD ▪ EPA ▪ DOE

Page Intentionally Left Blank

Page Intentionally Left Blank

REPORT DOCUMENTATION PAGE

Form Approved
OMB No. 0704-0188

Public reporting burden for this collection of information is estimated to average 1 hour per response, including the time for reviewing instructions, searching existing data sources, gathering and maintaining the data needed, and completing and reviewing this collection of information. Send comments regarding this burden estimate or any other aspect of this collection of information, including suggestions for reducing this burden to Department of Defense, Washington Headquarters Services, Directorate for Information Operations and Reports (0704-0188), 1215 Jefferson Davis Highway, Suite 1204, Arlington, VA 22202-4302. Respondents should be aware that notwithstanding any other provision of law, no person shall be subject to any penalty for failing to comply with a collection of information if it does not display a currently valid OMB control number. **PLEASE DO NOT RETURN YOUR FORM TO THE ABOVE ADDRESS.**

1. REPORT DATE (DD-MM-YYYY)	2. REPORT TYPE	3. DATES COVERED (From - To)
03-11-2016	FINAL	SEP-2014 TO NOV-2016

4. TITLE AND SUBTITLE	5a. CONTRACT NUMBER
Determining Detection and Classification Potential of Munitions using Advanced EMI Sensors in the Underwater Environment	W912HQ-14-C-0008
	5b. GRANT NUMBER
	5c. PROGRAM ELEMENT NUMBER

6. AUTHOR(S)	5d. PROJECT NUMBER
Billings, Stephen D & Song, Lin-Ping	MR-2412
	5e. TASK NUMBER
	5f. WORK UNIT NUMBER

7. PERFORMING ORGANIZATION NAME(S) AND ADDRESS(ES)	8. PERFORMING ORGANIZATION REPORT NUMBER
Black Tusk Geophysics Inc 401 / 1755 West Broadway Vancouver, BC, V6J4S5 Canada	

9. SPONSORING / MONITORING AGENCY NAME(S) AND ADDRESS(ES)	10. SPONSOR/MONITOR'S ACRONYM(S)
Strategic Environmental and Research & Development Program 4800 Mark Center Drive, Suite Alexandria, VA 22350-3605	SERDP
	11. SPONSOR/MONITOR'S REPORT NUMBER(S)

12. DISTRIBUTION / AVAILABILITY STATEMENT

Approved for public release; distribution is unlimited

13. SUPPLEMENTARY NOTES

14. ABSTRACT
The project focuses on characterizing Electromagnetic Induction (EMI) responses in the underwater setting through numerical and experimental studies with the objective of obtaining a better understanding of the impact of underwater environments on EMI marine systems deployed to detect and characterize buried munitions. Based on the results of this project, we conclude that underwater detection and characterization of buried metal using EMI based sensor is feasible. While the conductive sea-water introduces complications to the measurement process, there are numerous practical options for mitigation of these effects. The conductive sea-water can impact the scattered field from a buried metallic object, but typically only at very early times and at large receiver to object offsets. Neither of these conditions are commonly encountered in practice. Thus apart from the practical considerations of operating underwater, the modelling techniques and methods that have been successfully demonstrated in terrestrial environments can be utilized for marine detection and characterization. The principle remaining challenge is the development and deployment of a practical and effective set of hardware for marine EMI sensing.

15. SUBJECT TERMS
Munitions Response, Electromagnetic Induction, Unexploded Ordnance, Classification

16. SECURITY CLASSIFICATION OF:			17. LIMITATION OF ABSTRACT	18. NUMBER OF PAGES	19a. NAME OF RESPONSIBLE PERSON
a. REPORT	**b. ABSTRACT**	**c. THIS PAGE**			Stephen Billings
				69	**19b. TELEPHONE NUMBER** (include area code) 720 306 1165

Standard Form 298 (Rev. 8-98)
Prescribed by ANSI Std. Z39.18

Page Intentionally Left Blank

Executive summary

We report the results for the limited scope project (MR-2412) tilted "Determining Detection and Classification Potential of Munitions using Advanced EMI Sensors in the Underwater Environment." The project focuses on characterizing Electromagnetic Induction (EMI) responses in the underwater setting through numerical and experimental studies with the objective of obtaining a better understanding of the impact of underwater environments on EMI marine systems deployed to detect and characterize buried munitions. In terrestrial settings, conduction currents can be ignored in most soil types (conductivity ~ 0.01 S/m). The measured magnetic fields from a subsurface metallic object in the low-frequency EMI regime can be modelled as if the object were in free-space. In contrast, marine environments are generally highly conductive with an average conductivity of seawater of around 4 - 5 S/m. For a survey in a conductive medium, the EMI response of a compact metallic target can deviate from its in-air response.

For our numerical studies we developed an integral equation approach for a layered medium that was able to account for the changing conductivity of the air, marine and sea-bottom. We extended the model so we could compute both the background and scattered field response from a highly conducting and permeable sphere for dipole and loop transmitters and receivers. We carried out a series of synthetic experiments by considering various factors that might influence EMI signals, including current channeling effects, sea depth, the size of a loop, lateral offset of the receiver, host conductivity, excitation waveform and antenna insulation.

For our marine measurements, we built a 2 m x 1 m x 1 m fiberglass frame and encased two receiver cubes in epoxy to make them waterproof. The transmitter loop comprised 12 turns of wire arranged in a 2 m by 1 m rectangle. A 24V power-supply was used to provide a maximum current of 11.4 A using a 25 Hz base-frequency with a 50% duty cycle waveform. A series of different measurements campaigns were conducted in sea-water depths of between 2 and 14 m either from a boat or by wading into water adjacent to a sandy beach.

The response from a metallic body immersed in a conductive medium is a combination of the eddy current response (ECR) due to currents generated in the target and the galvanic coupling of currents through the body (the current channeling response, CCR). In terrestrial environments only the ECR is important. Our simulations showed that the CCR from a highly conducting and permeable sphere embedded in the air-sea-sediment is far smaller than the ECR and decays much faster than the ECR at a rate of t^{-3}. For the interesting time range of 0.1 ms - 25 ms, the CCR contributes little to the target signals and thus can be ignored. Meanwhile, at times beyond several hundred microseconds, the ECR response approaches the value for the same object embedded in free space. These numerical observations were confirmed by measurements of an insulated and non-insulated 105 mm projectile at a range of different receiver, transmitter and object offsets.

When considering a survey close to seafloor, we found that the decay rate of the background response is affected by the sea depth, or equivalently by the distance of the sensor from the air-sea interface. Our results show that the background response in shallow water decay faster than in a deeper water. In deeper water where the sensor is far away from the air-sea interface, the corresponding background responses asymptotically approaches the response of a half-space. Our simulations demonstrated that sea depths don't impact the scattered field response from a buried metallic object. Measurements conducted in water depths between 2 and 14 m displayed the same general characteristics as our simulations with the response in shallower water (2 m) falling off faster than the measurements at 14 m. Observed decay rates were between $t^{-5/2}$ and t^{-3}.

The background responses measured inside and outside of a transmitter loop are very similar and at later times vary little with offset distance from the transmitter center. These aspects of the offset

background measurements might be usefully applied to calibrate a system that has an array of sensors.

EMI responses depend upon other geometry survey parameters like the transmitter loop size and stand-off distance. A large transmitter loop can excite a strong scattered response from a buried object but also induces a larger background response. The latter might be removed by subtraction of the fields from widely separated receivers. To test this type of background suppression method we considered two possible configurations of receivers: vertical and radial with respect to the transmitters. The experiments showed that the vertical offset configuration can be effective at removing the background signals but only at later times. On the other hand, the results with radially symmetric receivers showed that the differential total responses are identical with the differential scattered responses for all components across all time range. The radial receiving configuration provides an effective way to obtain the scattered response purely from free space models.

The conductive sea-water medium causes dispersion of electromagnetic fields and can delay and distort the primary and scattered fields. For the primary field our simulations showed significant distortion effects for an ideal rectangular waveform particularly at large offset distances. However, when the exponential rise time of the transmitter loop was considered, the distortion effects became much less significant and can be ignored for the time-ranges and offset distances typically encountered in UXO sensing. These theoretical predictions were supported by measurements of the primary field distortion conducted with a flux-gate magnetometer.

During the off-time field dispersion exhibits increased delay with an increase in host conductivity. Results with a simulated marine TEMTADS system showed that the scattered responses excited from a long pulse of 10 ms are stronger than those from a short pulse of 1 ms in particular for late times. This demonstrates one method to further enhance target signals, which is equally effective and equivalent in the terrestrial realm. Further tests with simulated marine TEMTADS data showed that a terrestrial dipole polarizability model could be used to successfully characterize the scattered data from a buried metallic object in the conducting underwater environment.

We also considered the impact of insulation of the receiver and/or transmitter on marine sensing. Our preliminary numerical investigation showed that the insulation had negligible effect on the background fields.

Our last set of measurements focused on the spectral content of noise and signals in the underwater environment. We used a 24-bit analog to digital converter to sample a receiver cube at a rate of 120 kHz. Measurements were conducted on land immediately adjacent to marine measurements collected at a water depth of 4 m. The underwater measurements with no transmitter present were lower noise across most of the frequency spectrum compared to the on-land measurements. When the transmitter was operating and sufficiently damped by a resistor, the spectrum and off-time behavior on land and in water were virtually identical. From these results we can conclude that there are no significant differences between on-land and in-water sensing from the perspective of the frequency content of the noise and signal.

Based on the results of this limited scope project, we conclude that underwater detection and characterization of buried metal using EMI based sensor is feasible. While the conductive sea-water introduces complications to the measurement process, there are numerous practical options for mitigation of these effects. The conductive sea-water can impact the scattered field from a buried metallic object, but typically only at very early times and at large receiver to object offsets. Neither of these conditions are commonly encountered in practice. Thus apart from the practical considerations of operating underwater, the modelling techniques and methods that have been successfully demonstrated in terrestrial environments can be utilized for marine detection and characterization. The principle remaining challenge is the development and deployment of a practical and effective set of hardware for marine EMI sensing.

Contents

List of Figures

Acronyms

CCR	Current Channeling Response
cm	centimeter
DMM	Discarded Military Munitions
ECR	Eddy Current Response
EMI	Electromagnetic Induction
ESTCP	Environmental Security Technology Certification Program
Hz	hertz
m	meter
μ**s**	microsecond
ms	millisecond
HED	Horizontal Electric Dipole
HMD	Horizontal Magnetic Dipole
MEC	Munitions and Explosives of Concern
MTADS	Multi-sensor Towed Array Detection System
NRL	Naval Research Laboratory
Rx	Receiver
SERDP	Strategic Environmental Research and Development Program
SNR	Signal-to-Noise Ratio
TEM	Transient Electromagnetic Induction
TT	Transient Multi-sensor towed array detection system
Tx	Transmitter
UXO	Unexploded Ordnance
UW	UnderWater
VED	Vertical Electric Dipole
VMD	Vertical Magnetic Dipole

1   Background and Objective

Hazardous ordnance items are present along coast-lines and in rivers and lakes in waters shallow enough to cause concerns for human recreational and industrial activities. The presence of water makes it difficult to detect and remove these hazardous legacies induced from wars, military training and deliberate disposal (Schwartz and Brandenburg, 2009). A number of techniques have been proposed to detect and characterize Unexploded Ordnances (UXO) and discarded military munitions (DMM) in the underwater environment including acoustic waves, magnetometery, and electromagnetic induction (EMI) (SERDP-Workshop, 2013; Keenan et al., 2010; Shubitidze, 2011).

In recent years, terrestrial munitions response has seen significant improvements in our capability to discriminate MEC items from benign metallic clutter. These advances have been primarily driven by the development of next-generation EMI sensors designed to interrogate small, near-surface targets. The research reported in this project concerns underwater sensing using EMI which is distinct from the terrestrial setting in several respects including positioning requirements and techniques, noise environment and practical constraints on deployment of sensor systems. For marine sites an even more fundamental difference between the two settings is the conductivity of the background. In terrestrial settings, conduction currents can be ignored in a typical UXO contaminated soil environment (conductivity around $\sim 0.01\ \mathrm{S/m}$) (Shubitidze et al., 2004). Thus the measured magnetic fields from a subsurface metallic object in the low-frequency EMI regime can be modelled as if the object were in free-space. In contrast, marine environments are generally highly conductive with an average conductivity of seawater of around $4 \sim 5\ \mathrm{S/m}$. For a survey in a conductive medium, the EMI response of a compact metallic target can deviate from its in-air response. Norton et al. (2005) studied the electromagnetic induction response to conducting anomalies of spheroidal shape embedded in a weakly conducting host medium. Shubitidze et al under the SERDP MR-1632 project (Shubitidze, 2011; Shubitidze et al., 2008, 2009) used the method of auxiliary sources (MAS) to study the scattered responses of a metallic object placed in a uniform conductive medium (Shubitidze et al., 2002, 2004). Their results showed that coupling effects between the metallic objects and the conductive surrounding can be important at early times (or at high frequencies) but that the scattered responses at late times are close to those in free space.

One limitation of this previous work is that any difference between the conductivity of ocean sediments and sea-water was ignored. Depending upon porosity, sea sediments may have a conductivity that is generally less than $1.0\ \mathrm{S/m}$ (Chave et al., 1991). Given the presence of the sea-sediment conductive interface, we speculate that a simple uniform conductive space (Norton et al., 2005; Shubitidze et al., 2009) may not provide an effective model of the EMI responses of a buried object when measurements are taken close to the seafloor. In addition, we lack understanding about how the background responses in a conducting medium might mask the scattered responses of a target of interest.

Within the project we aimed to establish the limitations and potential for detection and classification using EMI data in a variety of underwater environments through the use of modeling, simulation studies and empirical measurements. Our research has aspects in common with SERDP Project MR-2409 (Bell et al., 2016) where the principal focus is on empirical measurements of the background and target EMI response in the controlled environment of a large salt water tank. In addition, some of the research questions addressed in this project were motivated by measurements reported, or results obtained in (Bell et al., 2016).

In the first part of this report we describe the development of a numerical model that accounts for the influence of the conductive sea-water medium and the air-water and water-seafloor interfaces on EMI sensing. We then expand the model so it can be used to compute the scattered response from a compact metallic object due to currents induced within the object (the Eddy Current Response,

ECR) and galvanically coupled through the object (the Current Channeling Response, CCR). Using the model developed, we then report on a series of synthetic experiments designed to help understand a number of factors germane to underwater EMI sensing. These include: (i) the impact of sea-water depth on the background response; (ii) the lateral variation of background response around a given transmitter coil; (iii) the effect of transmitter size and stand-off on the background and scatted object responses; (iv) the use of differential measurements to remove background; (v) dispersion of the electromagnetic fields in sea-water; and (vi) inversion of simulated data. Motivated by some measurements inside insulated systems by (Bell et al., 2016) we then developed a model to understand the response of a Vertical Mangetic Dipole (VMD)[1] embedded in an insulated cavity. In the final part of the report we describe a number of empirical measurements which were conducted either from a boat or from the shore, in water depths between 2 and 14 m. We used a prototype EMI sensor comprising two receiver cubes and a 1 m by 2 m transmitter loop. These empirical measurements augment the theoretical work of the proceeding sections.

We expect that our results will offer a solid basis for future work of 1) adapting and developing the data processing, analysis and interpretation strategies for marine EMI sensor data; 2) designing and deploying advanced underwater EMI sensor systems; 3) improving the ability to characterize UW sites contaminated by UXO and performing cost-effective detection and classification in the UW realm.

---

[1]A VMD is a simple approximately to a physical transmitter loop

---

2 Integral equation technique in a Layered Medium

2.1 Problem formulation

Consider an underwater environment where the electromagnetic properties are different vertically. A simplified representation comprises a three-layer structure consisting of the upper half-space (region 1, air), the middle layer (region 2, seawater) and the lower half-space (region 3, sediment ground), as schematically shown in Fig. 1. Taking the positive z-axis downward in the right-handed coordinate system and choosing the origin of the z-axis at the ocean surface, we have the air-sea interface at $z_1 = 0$ and the sea-sediment interface z_2. Then the thickness of the seawater depth given as $d_{\text{sea}} = z_2$.

The electromagnetic properties for each horizontally infinite and homogeneous layer are characterized by the conductivity, permittivity, and permeability, denoted as $(\sigma_i, \epsilon_i, \mu_i)$. $\epsilon_i = \epsilon_0 \epsilon_{ri}$, $\mu_i = \mu_0 \mu_{ri}$, where $i = 1, 2, 3$ and ϵ_{ri} and μ_{ri} are the associated relative permittivity and permeability constants with $\epsilon_0 = 8.854 \times 10^{-12}$ (farads/meter) and $\mu_0 = 4\pi \times 10^{-7}$ (henries/meter). Assuming non-magnetic sediments, the magnetic permeability of each layer can be set to that of free space. For time-harmonic electromagnetic fields with $e^{j\omega t}$, where ω is an angular frequency, t time, and $j = \sqrt{-1}$, we use the complex conductivity $\hat{\sigma}$ defined as $\hat{\sigma} = \sigma + j\omega\epsilon$ to collectively describe conductivity and permittivity. Then the squared wavenumber is given as

$$k^2 = -j\omega\mu\hat{\sigma}. \tag{1}$$

Under the quasi-static approximation of low frequencies (Ward and Hohmann, 1988), displacement
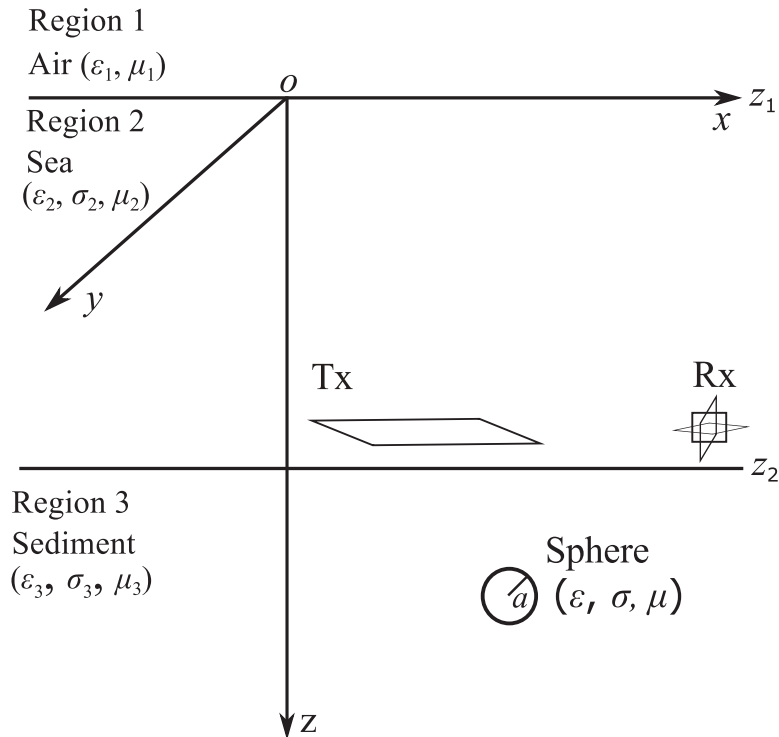
Figure 1: Geometric configuration of the problem. An underwater environment is represented by a three-layer structure that consists of the upper half-space (region 1, air), the middle layer (region 2, seawater), and the lower halfspace (region 3, sediment ground). Loop transmitter and receivers are immersed in the sea to interrogate a metallic object buried below seafloor.

currents are negligible (i.e., $\omega\epsilon \ll \sigma$) and the conductivity dominates in the computation. In this case, the squared wavenumber in Eq. (1) becomes purely imaginary and electromagnetic fields behave in a diffusive manner.

As with the terrestrial case, we assume that an array of transmitters and receivers can be deployed in the sea to interrogate a metallic target buried in underwater sediments. In the marine setting, the responses to be recorded are not only generated from targets of interest but also the diffusive interaction with the conductive surroundings. According to electromagnetic scattering theory (Ward and Hohmann, 1988; Chew, 1999), the measured responses in the seawater are described by

$$\mathbf{H}(t) = \mathbf{H}_{\text{inc}}(t) + \mathbf{H}_{\text{sca}}(t), \tag{2}$$

where the total responses $\mathbf{H}^T = [H_x \ H_y \ H_z]$ are the sum of the associated incident fields $\mathbf{H}_{\text{inc}}(t)$ in the conducting layered structure and the scattered fields $\mathbf{H}_{\text{sca}}(t)$ due to a buried target upon excitation. To compute the $\mathbf{H}_{\text{inc}}(t)$ and $\mathbf{H}_{\text{sca}}(t)$, we use an integration equation technique (Wait, 1970; Chew, 1999).

2.2 Field representation for fundamental sources

First, we describe the fundamental solutions of electromagnetic fields (Green's tensors) when the elementary sources like electric and magnetic current dipoles are used to generate exciting fields in a layered medium. The field expressions are formulated in the wavenumber and frequency domains and can be numerically transformed into the corresponding transient responses through the digital filtering techniques reported in Anderson (1982).

Consider the general case where both electric and magnetic sources are present in a medium. In terms of the magnetic and electric potentials $\mathbf{A}$ and $\mathbf{F}$ (Harrington, 2001; Ward and Hohmann, 1988), the electric and magnetic fields can be expressed as

$$\mathbf{E} = -\nabla \times \mathbf{F} - j\omega\mu\mathbf{A} + \frac{1}{\hat{\sigma}}\nabla(\nabla \cdot \mathbf{A})$$
$$\mathbf{H} = \nabla \times \mathbf{A} - \hat{\sigma}\mathbf{F} + \frac{1}{j\omega\mu}\nabla(\nabla \cdot \mathbf{F}) \tag{3}$$

where ∇ is a vectorial differential operator: $\frac{\partial}{\partial x}\hat{x} + \frac{\partial}{\partial y}\hat{y} + \frac{\partial}{\partial z}\hat{z}$, and $\hat{x}$, $\hat{y}$, $\hat{z}$ denote the three unit coordinate vectors. Both $\mathbf{A}$ and $\mathbf{F}$ satisfy the inhomogeneous Helmholtz equation

$$\nabla^2\mathbf{A} + k^2\mathbf{A} = -\mathbf{J}$$
$$\nabla^2\mathbf{F} + k^2\mathbf{F} = -\mathbf{M} \tag{4}$$

where $\mathbf{J}$ and $\mathbf{M}$ represents electric and magnetic sources, respectively. Hence finding $\mathbf{H}$ and $\mathbf{E}$ fields for arbitrary EM sources reduces to solving the governing equation (4) for the vector potential fields $\mathbf{A}$ and $\mathbf{F}$.

For elementary sources: a magnetic current dipole and electric current dipole oriented along a unit vector $\hat{\psi}$ with the strength p_m and p_e, we can have $\mathbf{M}(\mathbf{r}) = \hat{\psi}p_m\delta(\mathbf{r} - \mathbf{r}')$ and $\mathbf{J}(\mathbf{r}) = \hat{\psi}p_e\delta(\mathbf{r} - \mathbf{r}')$ in Eq. (4). δ is the Dirac delta function. $\mathbf{r}' = (x', y', z')$ and $\mathbf{r} = (x, y, z)$ represent the source and field point coordinates, respectively. p_m and p_e are given by (Wait, 1970, 1982; Ward and Hohmann, 1988),

$$p_m = \frac{j\omega\mu I dS}{4\pi}$$

$$p_e = \frac{I dl}{4\pi} \tag{5}$$

where I is the current flowing in a loop of area dS or a linear wire element dl. When $\hat{\psi}$ points in unit coordinate direction of $\hat{z}$ or $\hat{x}$ or $\hat{y}$, we say that these corresponds to the VMD (vertical magnetic dipole), or HMD (horizontal magnetic dipole), or VED (vertical electric dipole), or HED (horizontal electric dipole) sources. Applying the Fourier-Bessel transform to field equations Eq. (4) in a layered medium (Ward and Hohmann, 1988; Wait, 1970), we can obtain a spectral-domain representation of the potential fields that is a superposition of the upper and downward plane waves propagating in the z-direction, modulated by the oscillatory function at a given distance between the source and field points. In the source region, the total fields are written as the sum of primary and secondary upward/downward fields.

When a VMD is immersed in the seawater in Fig 1, we can write the spectral representation of the z-component potential $F_{jz}, j = 1, 2, 3$ in each layer as

$$F_{1z}(\rho, z) = m \int_0^\infty B_1 e^{\gamma_1(z-z_1)} J_0(\lambda\rho) d\lambda, \ z < z_1$$

$$F_{2z}(\rho, z) = m \int_0^\infty \left[A_2 e^{-\gamma_2(z-z_1)} + B_2 e^{\gamma_2(z-z_2)} + \frac{\lambda}{\gamma_2} e^{-\gamma_2|z-z'|} \right] J_0(\lambda\rho) d\lambda, \ z_1 < z < z_2, \tag{6}$$

$$F_{3z}(\rho, z) = m \int_0^\infty A_3 e^{-\gamma_3(z-z_2)} J_0(\lambda\rho) d\lambda, \ z > z_2$$

where $\rho = \sqrt{(x-x')^2 + (y-y')^2}$, $\gamma_j = (\lambda^2 - k_j^2)^{1/2}$, λ is a radial wavenumber, and $J_0(\lambda\rho)$ is the Bessel functions of the first kind of order 0. A_j and B_j denote the downward and upward field amplitudes in layer j, respectively. The expressions in Eq. (6) are the well-known Sommerfeld-type integral. Subscript 1, 2, or 3 is added to these quantities when they refer specifically to the upper half space, the sea, and the bottom, respectively. The exponential factors in the representation might be interpreted as upward and downward waves that attenuate to zero at $z = \pm\infty$. In layer 2, A_2 and B_2 are the coefficients for the downward and upward propagation waves from the air-ocean and seafloor interfaces, in addition with a direct wave term $e^{-\gamma_2|z-z'|}$. This direct term can be important for a UXO survey where the transmitter and receiver are generally close. When an observation is close to the seafloor, the upward propagation wave term $e^{\gamma_2(z-z_2)}$ can play an important role. Similarly, if an observation is near the ocean surface, the downward propagation wave term $e^{-\gamma_2(z-z_1)}$ would be dominant. In layer 1 and 3, B_1 and A_3 corresponding with the upward and downward propagating waves in the air and the sediment layer. There can be no wave coming from $z = \mp\infty$, therefore $A_1 = B_3 = 0$.

Amplitudes A_j and B_j can be determined by continuity of the tangential field components of $\mathbf{E}$ and $\mathbf{H}$ at the interface (Harrington, 2001; Chew, 1999). For the VMD excitation, the electromagnetic boundary conditions for $\mathbf{F}$ on layers j and $j-1$ are given as (Wait, 1970; Ward and Hohmann, 1988)

$$F_{z,j-1} = F_{z,j}$$

$$\frac{1}{\mu_{j-1}} \frac{dF_{z,j-1}}{dz} = \frac{1}{\mu_j} \frac{dF_{z,j}}{dz}. \tag{7}$$

In the case of VED excitation in the sea in Fig 1, the spectral representation for potential field $\mathbf{A}$ is exactly the same as those given in Eq. (6) but amplitude coefficients must satisfy the associated boundary conditions:

$$A_{z,j-1} = A_{z,j}$$
$$\frac{1}{\hat{\sigma}_{j-1}} \frac{dA_{z,j-1}}{dz} = \frac{1}{\hat{\sigma}_j} \frac{dA_{z,j}}{dz}. \tag{8}$$

When a VMD is in the lower half space in which a target is embedded, we can write the corresponding spectral representation of fields as

$$F_{1z}(\rho, z) = m \int_0^\infty B_1 e^{\gamma_1(z-z_1)} J_0(\lambda\rho)d\lambda, \ z < z_1$$
$$F_{2z}(\rho, z) = m \int_0^\infty \left(A_2 e^{-\gamma_2(z-z_1)} + B_2 e^{\gamma_2(z-z_2)} \right) J_0(\lambda\rho)d\lambda, \ z_1 < z < z_2 \tag{9}$$
$$F_{3z}(\rho, z) = m \int_0^\infty \left(A_3 e^{-\gamma_3(z-z_2)} + \frac{\lambda}{\gamma_3} e^{-\gamma_3|z-z'|} \right) J_0(\lambda\rho)d\lambda, \ z > z_2$$

The same form of the spectral representation of Eq. (9) applies to a VED source buried in region 3. The upper and downward amplitudes are found by imposing the correspondingly boundary conditions of either Eqs. (7) or (8).

A horizontally-directed magnetic (electrical) dipole, say pointing in x direction, NOT only induces a component of the potential along the dipole direction, $F_x(A_x)$, but also a component, $F_z(A_z)$, in the vertical direction. The derivation process of fields is similar to the above VMD (VED) cases. The expressions for a HMD (HED) excitation are more involved than a VMD (VED) case as we have four more downward and upward amplitudes related to a HMD (HED) to be determined due to electromagnetic inhomogeneities. For the complete HMD-related expressions we refer the interested reader to Song et al. (2016). Here we give the boundary conditions for HMD and HED that must be satisfied. For the x-oriented HMD, continuity of the tangential field components of $\mathbf{E}$ and $\mathbf{H}$ at the interface leads to the boundary conditions about the potential F (Wait, 1970; Ward and Hohmann, 1988):

$$F_{z,j-1} = F_{z,j}$$
$$\frac{1}{\mu_{j-1}} \left(\frac{dF_{x,j-1}}{dx} + \frac{dF_{z,j-1}}{dz} \right) = \frac{1}{\mu_j} \left(\frac{dF_{x,j}}{dx} + \frac{dF_{z,j}}{dz} \right)$$
$$\sigma_{j-1} F_{x,j-1} = \sigma_j F_{x,j} \tag{10}$$
$$\frac{dF_{x,j-1}}{dz} = \frac{dF_{x,j}}{dz}.$$

Similarly for the x-oriented HED, the boundary conditions of the potential A hold

$$A_{z,j-1} = A_{z,j}$$
$$\frac{1}{\hat{\sigma}_{j-1}} \left(\frac{\partial A_{x,j-1}}{\partial x} + \frac{\partial A_{z,j-1}}{\partial z} \right) = \frac{1}{\hat{\sigma}_j} \left(\frac{\partial A_{x,j}}{\partial x} + \frac{\partial A_{z,j}}{\partial z} \right)$$
$$\mu_{j-1} A_{x,j-1} = \mu_j A_{x,j} \tag{11}$$
$$\frac{\partial A_{x,j-1}}{\partial z} = \frac{\partial A_{x,j}}{\partial z}.$$
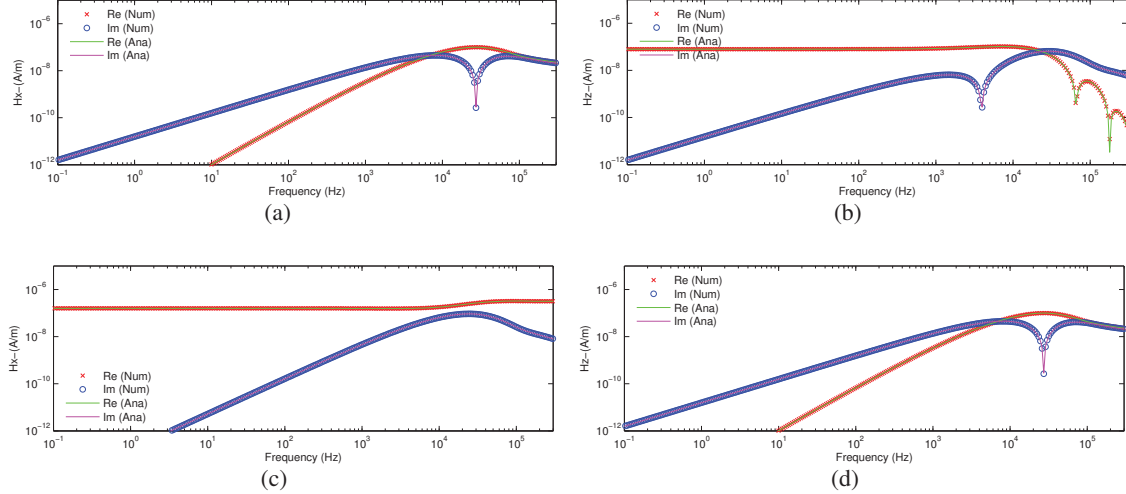
Figure 2: Check of numerical harmonic fields with analytical ones for the observation at 100 m on a 0.01 S/m of homogeneous half space. VMD: (a) H_x; (b) H_z. HMD: (c) H_x; (d) H_z.

Noticing the duality between the boundary conditions of VMD and VED, HMD and HED in Eqs. (7) and (8), Eqs. (10) and (11), we can easily obtain the upward and downward coefficients for VED and HED simply by exchanging μ_j and $\hat{\sigma}_j$ in those corresponding amplitude expressions to the VMD and HMD. All the above improper integrals in Eqs. (6) and (9) are evaluated through Anderson's digital filtering techniques (Anderson, 1982). Since the filtering technique was designed to have narrow bandlimited filter response over a logarithmically transformed abscissa range, the numerical integration with larger values of λ is adaptively contained in the algorithm.

To evaluate the accuracy of the numerical Hankel transformation, we compute the harmonic fields for an observation at 100 m on a 0.01 S/m homogeneous half space. In this case, analytical expressions for the harmonic horizontal and vertical components of a VMD and HMD are given by Eqs. (4.56) and (4.59), Eqs. (4.126) and (4.128)-(4.129) in Ward and Hohmann (1988). Our three-layer model is reduced to a half space model by setting $z_2 = 0$ and $\sigma_2 = \sigma_3 = 0.01$ S/m. Fig. 2 includes a check of the numerical and analytical results of H_x and H_z from VMD and HMD sources which are all in close agreement. With the same half space model, we also check the computation of transient fields by the digital filter technique described below. The analytical field expressions for a VMD are given by Eqs. (4.69a) and (4.70), (4.72) and (4.74) in Ward and Hohmann (1988). Fig. 3 (a)-(b) shows the numerical and analytical results by a VMD which are all in close agreement. For HMD, there are no analytical formulae available. However the z-component from HMD must be reciprocal with the x-component from VMD. Fig. 3 (c) shows the reciprocity by comparing the numerical results of HMD with the analytical ones of VMD.

Given the complete integral representations for the potentials in the three layers, the fundamental field components in any layer in Fig. 1 can be obtained through Eq. (3), including 1) the incident fields when source and receiver loops reside in the sea; 2) the incident fields that penetrate from the source in the sea down into the sediment layer; 3) Green's tensor transmitting a source in the ground upward into a receiver in the sea. Next we present the formulation to compute the scattered fields from an object buried in the sediment.
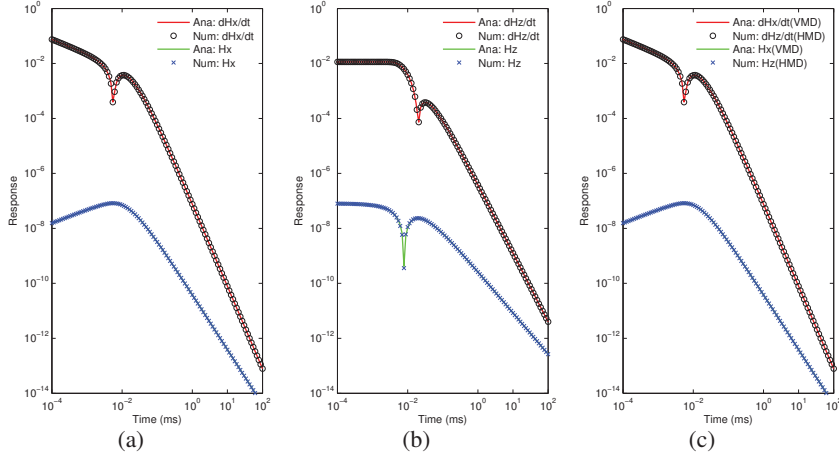
Figure 3: Check of numerical transient fields with analytical ones for the observation at 100 m on a 0.01 S/m of homogeneous half space. VMD: (a) H_x and dH_x/dt; (b) H_z and dH_z/dt. (c) HMD components H_z and dH_z/dt vs.VMD components H_x and dH_x/dt.

2.3 Scattered field from a buried metallic object: ECR and CCR

Following the terrestrial case, we also consider a underwater UXO survey where the dimension of a target of interest is small relative to the target-sensor distance such that the primary fields around the target can be assumed to be approximately uniform. Further, for sufficiently low frequencies, it is possible to represent the transient scattering of a metallic object by an equivalent induced dipole. This concept has been successfully used in the interpretation of land-based EMI sensing of metallic objects (Das et al., 1990; Carin et al., 2001; Pasion and Oldenburg, 2001; Barrow and Nelson, 2001; Bell et al., 2001; Miller et al., 2001; Pasion, 2007; Gasperikova et al., 2008; Billings et al., 2010; Beran et al., 2013). Norton et al. (2005) noted that the scattered field from a spheroid immersed in a uniform conducting medium appear dipole-like if the target size is small compared to the sensor-target range. That is, we use an induced magnetic dipole to model the so-called eddy current response (ECR) due to currents generated in the target. For a conducting medium, the perturbation of electric field due to a body in principle would produce an additional EMI response that is called the current channeling response (CCR). That can be modelled by an electric dipole.

For an isolated object that can be treated like a point-target in the low-frequency regime, we use magnetic and electric polarizability tensors $\mathbf{P}_m(\omega)$ and $\mathbf{P}_e(\omega)$ to characterize the scattering property of an object. Based upon the Green's function method, we express the scattered field $\mathbf{H}_{\mathrm{sca}}(\mathbf{r}_{Rx}, \omega)$ at $\mathbf{r}_{Rx}$ as

$$\mathbf{H}_{\mathrm{sca}}(\mathbf{r}_{Rx}, \omega) = \mathbf{G}_{HH}(\mathbf{r}_{Rx}, \mathbf{r}', \omega)\mathbf{P}_m(\omega)\mathbf{H}(\mathbf{r}', \mathbf{r}_{Tx}, \omega) + \mathbf{G}_{HE}(\mathbf{r}_{Rx}, \mathbf{r}', \omega)\mathbf{P}_e(\omega)\mathbf{E}(\mathbf{r}', \mathbf{r}_{Tx}, \omega),$$
$$(12)$$

where the product $\mathbf{P}_m(\omega)\mathbf{H}(\mathbf{r}', \mathbf{r}_{Tx}, \omega)$ is the induced magnetic dipole moment (Das et al., 1990; Carin et al., 2001; Bell et al., 2001) in a target by the illuminating field $\mathbf{H}(\mathbf{r}', \mathbf{r}_{Tx}, \omega)$ from a transmitting antenna at $\mathbf{r}_{Tx}$. Correspondingly, the product $\mathbf{P}_e(\omega)\mathbf{E}(\mathbf{r}', \mathbf{r}_{Tx}, \omega)$ is the induced electric dipole moment. $\mathbf{G}_{HH}(\mathbf{r}_{Rx}, \mathbf{r}, \omega)$ specifies the magnetic Green tensor in the background relating the field at $\mathbf{r}_{Rx}$ due to the target at $\mathbf{r}$ radiating into the sea; $\mathbf{G}_{HE}(\mathbf{r}_{Rx}, \mathbf{r}, \omega)$ a mixed magnetic Green tensor in the background produced by the electric sources. The primary $\mathbf{H}$ and $\mathbf{E}$ fields and Green's tensors $\mathbf{G}_{HH}$ and $\mathbf{G}_{HE}$ are calculated using the three-layered formulae presented in Section 3.1 for vertical and horizontal electrical and magnetic dipoles. Eq. (12) is a simplified form of a full volume integral

equation (Wannamaker et al., 1984; Ward and Hohmann, 1988; Chew, 1999; Song and Liu, 2005; Farquharson et al., 2006) where we replace the total fields internal to a body by the induced dipole moments at a point target.

For the above approximation to be used in a underwater setting, we neglect the possible interactions between a buried object and the seafloor assuming that the object is not close to the interface. This makes (12) easily implemented to compute the scattered field response of an object when its magnetic and electric polarizabilities are known. For a general case, one might resort to solving a full domain integral equation (Wannamaker et al., 1984; Ward and Hohmann, 1988; Chew, 1999; Song and Liu, 2005; Farquharson et al., 2006), which can be challenging for very high conductivity and permeablilty.

For a highly conducting and permeable object, its conductivity and relative permeability can be $6 \sim 7$ and $2 \sim 3$ orders of magnitude larger than those of its surrounding medium such as the sea-sediment layers of interest. Therefore, it might be reasonable to assume a relatively weakly conducting, non-magnetic background in the simulation. With this assumption, we use a sphere as our object of interest for the analytic form of its magnetic polarizability under the quasi-static regime (i.e., displacement current is ignored) (Wait, 1951; Ward, 1959; Grant and West, 1965). Given a sphere with a radius of a, relative permeability μ_r, $\mu = \mu_0 \mu_r$, and conductivity σ, the polarizabiltiy tensor can be expressed as

$$\mathbf{P}_m = -2\pi a^3 R_m \mathbf{I}, \tag{13}$$

where $\mathbf{I}$ is a 3×3 identity matrix and the complex response function R_m is given by

$$R_m = -\frac{2\mu_r(\tanh \alpha - \alpha) + (\tanh \alpha - \alpha + \alpha^2 \tanh \alpha)}{\mu_r(\tanh \alpha - \alpha) - (\tanh \alpha - \alpha + \alpha^2 \tanh \alpha)} \tag{14}$$

and

$$\alpha = (i\omega\mu\sigma)^{1/2} a.$$

Following the procedure in the magnetic case where an alternating uniform magnetic field is applied (Grant and West, 1965), we can derive the electric polarizabiltiy tensor of a conducting and permeable sphere assuming that an alternating uniform electric field is applied, i.e.,

$$\mathbf{P}_e = -2\pi a^3 \sigma_1 R_e \mathbf{I}, \tag{15}$$

where R_e the electric complex response function is given by

$$R_e = -\frac{2\hat{\sigma}_2(\tanh \alpha - \alpha) + \hat{\sigma}_1(\tanh \alpha - \alpha + \alpha^2 \tanh \alpha)}{\hat{\sigma}_2(\tanh \alpha - \alpha) - \hat{\sigma}_1(\tanh \alpha - \alpha + \alpha^2 \tanh \alpha)}. \tag{16}$$

Using the small argument approximation of the hyperbolic function $\tanh(\cdot)$, for a small α we have

$$R_e \longrightarrow 2\frac{\sigma_1 - \sigma_2}{2\sigma_1 + \sigma_2}$$

and thus

$$\mathbf{P}_e = -4\pi a^3 \sigma_1 \frac{\sigma_1 - \sigma_2}{2\sigma_1 + \sigma_2} \mathbf{I}. \tag{17}$$

Further when $\sigma_2 \gg \sigma_1$, Eq. (17) reduces to

$$\mathbf{P}_e = 4\pi a^3 \sigma_1 \mathbf{I}. \tag{18}$$

This result is the same as the one derived for an electrical dipole moment when an uniform plane wave illuminating a perfectly conducting sphere in Harrington (2001); Norton et al. (2005). For an insulating object in a conducting medium, $\sigma_2 \ll \sigma_1$, we see either from (16) or (17),

$$\mathbf{P}_e = -2\pi a^3 \sigma_1 \mathbf{I}. \tag{19}$$

Thus, the response to a spherical void is half the magnitude and opposite in sign to the response to a perfectly conducting sphere (Norton et al., 2005).

Having obtained the steady-state solutions to the background and secondary response, we now proceed with the computation of the associated transient scattering responses. In time-domain EMI sensing of UXO, the data are in general collected as a series of voltages after the transmitting current is shut off. The voltage measurements are related to the time derivatives of magnetic field (Harrington, 2001; Ward and Hohmann, 1988). For an idealized step-off current excitation, the time derivatives of magnetic fields are the impulse responses measured in a receiver coil. Denote an EM field quantity $H(\omega)$ in the frequency domain, representing either the background fields or secondary ones in our case. The corresponding impulse response $h(t)$ with an implied causality constraint, i.e., $h(t) = 0$, $t < 0$, can be expressed as an inverse sine transform (Newman et al., 1986; Arfken and Weber, 1995),

$$h(t) = -\frac{2}{\pi} \int_0^\infty \mathrm{Im}\left[H(\omega)\right] \sin \omega t \, d\omega, \tag{20}$$

where $\mathrm{Im}[\cdot]$ is an imaginary operation over a complex field $H(\omega)$. The sine transform of (20) is similarly evaluated with the digital filtering techniques (Anderson, 1982). For a general current excitation, the transient response can be calculated via a convolution of the impulse response and the transmitter waveform (Wait, 1982; Song et al., 2008).

We are interested to know whether the CCR is small enough to be ignored compared to the ECR. In the following numerical studies, we compare the ECR and CCR. We model a marine environment by using the electromagnetic parameters: $\sigma_1 = 0$ S/m, $\mu_{r1} = 1$; $\sigma_2 = 4$ S/m, $\mu_{r2} = 1$; $\sigma_3 = 0.4$ S/m, $\mu_{r3} = 1$, which represent the air, sea, and the sediment, respectively. The air-sea and sea-sediment interfaces are at $z_1 = 0$ m, $z_2 = 20$ m. The seawater depth $d_2 = 20$ m. A steel sphere with a radius of $a = 0.3$ m, $\sigma = 10^6$ S/m, and $\mu_r = 300$ is buried below the sediment at a depth of 3.25 m. The sphere is located at $\mathbf{r} = (0.05, 0.05, 23.25)$ m in the coordinate system. This simulates a deep object scenario in the underwater setting. Transmitters and receivers are positioned 0.1 m above the seafloor. In the experiment, we assumed two Tx-Rx offsets: (1) a transmitting source located at $\mathbf{r}_{Tx} = (0.10, -0.10, 19.9)$ m and a receiver at $\mathbf{r}_{Rx} = (-0.10, 0.10, 19.9)$ m; to provide a distance between the Tx and Rx points of 0.28 m; and (2) $\mathbf{r}_{Tx} = (1.0, -1.0, 19.9)$ m and $\mathbf{r}_{Rx} = (-1.0, 1.0, 19.9)$ m; the distance between the Tx and Rx points of about 2.83 m. Figs. 4 (a)-(b) and (c)-(d) show the ECR and CCR for x- and z- components when Tx-Rx offsets are at 0.28 m and 2.8 m. We see that CCR can be larger than ECR earlier than 0.1 ms and decays fast, at a rate of t^{-3}.

Our numerical results are consistent with the study (Norton et al., 2005) and the recent experimental results (Bell et al., 2016). Norton et al. (2005) argued that the CCR might be significant when sensor-target distance is larger than the skin depth in a host medium or equivalently when measurements are concerned with earlier times. Given that the earliest time interested in the UXO survey is about 0.1 ms and with the frequency of 10 kHz and the conductivity 0.4 S/m of sea-sediment, we estimate a minimum skin depth of 8 m. This is sufficiently greater than the deepest possible detection distance $2 \sim 3$ m in the underwater. Bearing in mind these survey parameters and the numerical comparison of ECR and CCR, we consider that the CCR or electric dipole contribution to the EMI response is negligible in our case and thus ignore the second term of Eq. (12) in the following simulations.
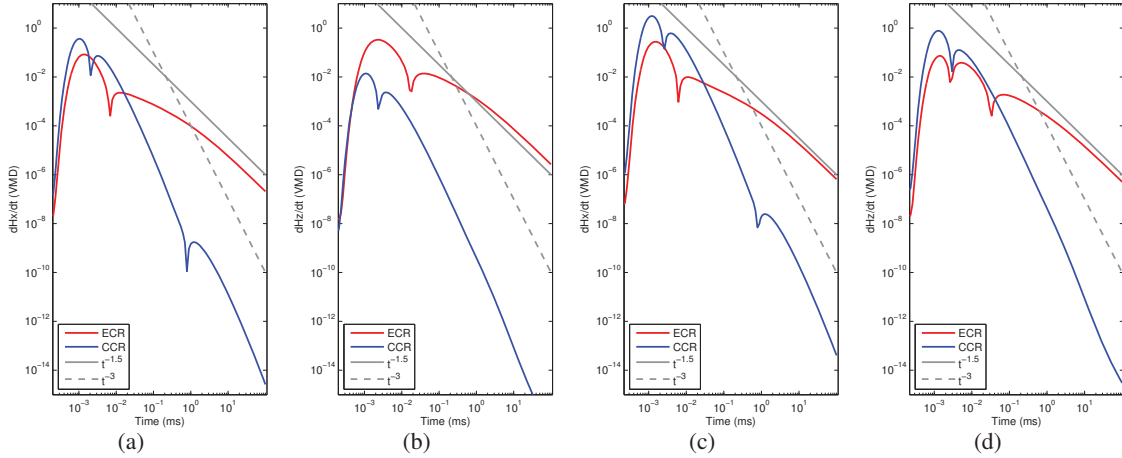
Figure 4: Comparing eddy current response and current channeling response. Tx-Rx offset = 0.28 m: (a) x-component; (b) z-component. Tx-Rx offset = 2.8 m: (c) x-component; (d)z-component.

2.4 Computing fields for a loop transmitter and receiver

In EMI sensing of UXO, either rectangular or circular loop transmitters and receivers are commonly used. To compute the fields generated from a transmitter loop immersed in the sea, we might simply do a surface integration over a transmitter loop Tx, i.e.,

$$\hat{\mathbf{H}}(\mathbf{r}, \mathbf{r}_{Tx}, \omega) = \int\int_{Tx} \mathbf{H}_m(\mathbf{r}, \mathbf{r}_{Tx}, \omega) dS_{Tx}, \tag{21}$$

where dS_{Tx} is a surface element and is equal to $dxdy$, $dxdz$, and $dydz$ for a z-, y-, and x-directed rectangular loop, respectively. $\mathbf{H}_m$ denotes the field at $\mathbf{r}$ generated by a associated unit magnetic dipole. In other words, we view a loop as consisting of many elementary magnetic dipoles and numerically convert Eq. (21) into a discrete summation over each individual dipole source contribution. An alternative way is to use the electric-type source formulation in terms of the $\mathbf{A}$-potential in Sec. 2.2. The field of a rectangular loop in the sea can be expressed as a line integral

$$\hat{\mathbf{H}}(\mathbf{r}, \mathbf{r}_{Tx}, \omega) = \int_{Tx} \mathbf{H}_e(\mathbf{r}, \mathbf{r}_{Tx}, \omega) dl_{Tx}, \tag{22}$$

where $\mathbf{H}_e$ is a magnetic field produced by an electric dipole and dl_{Tx} the differential element along the loop edge. For a z-directed Tx loop, we need x-and y-directed electrical dipole elements to compute the primary field $\mathbf{H}$ and $\mathbf{E}$ at a specified location $\mathbf{r}$. For a x-directed Tx loop, we need y-and z-directed electrical dipole line integrations.

To verify the loop formulations, we assume a square Tx loop of 88.62 m × 88.62 m sitting on the surface of a half space of 0.01 S/m. For a unit step-off excitation, Fig. 5 (a) shows the transient dH_z/dt fields at the center of the loop computed with Eqs. (21) and (22). The numerical results are obtained by using the midpoint integration rule (100 intervals) and digital linear filter technique. The analytical field is calculated by using Eq. (4.97) in Ward and Hohmann (1988) with a circular loop of radius 50 m. The circular loop has the same surface area as the square loop. Both analytical and numerical results agree well with each other with an error of less than 2% after 0.01 ms (Fig. 5(b)). To save computational time, it is preferred to use Eq. (22) performing a one-dimensional integration along loop edges.

To compute the primary magnetic flux received over a receiver loop, we need to carry out an integral over the surface of an Rx loop:

$$\Phi(\mathbf{r}_{Rx}, \mathbf{r}_{Tx}, \omega) = \int_{Rx} \hat{\mathbf{H}}(\mathbf{r}_{Rx}, \mathbf{r}_{Tx}, \omega) \cdot d\mathbf{S}_{Rx}, \tag{23}$$

where $d\mathbf{S}_{Rx}$ is the directed surface element of a Rx loop and $\hat{\mathbf{H}}$ is given either by Eq. (21) or (22). Eq. (23) involves a quadruple or triple numerical integration. However it can be simplified by using the relationship $\mathbf{H}_e = \nabla \times \mathbf{A}$ and the Stoke theorem,

$$
\begin{aligned}
\Phi(\mathbf{r}_{Rx}, \mathbf{r}_{Tx}, \omega) &= \int_{Rx} \hat{\mathbf{H}}(\mathbf{r}_{Rx}, \mathbf{r}_{Tx}, \omega) \cdot d\mathbf{S}_{Rx} \\
&= \int_{Tx} \left[\int_{Rx} \mathbf{A}(\mathbf{r}_{Rx}, \mathbf{r}_{Tx}, \omega) \cdot d\mathbf{l}_{Rx} \right] dl_{Tx},
\end{aligned}
\tag{24}
$$

where $d\mathbf{l}_{Rx}$ is a directed line element. The calculation of the primary flux passing through a receiver loop becomes a double line integration along Tx and Rx loop with the potential $\mathbf{A}$. Similarly, we assume a square Tx loop of 88.62 m × 88.62 m sitting on the surface of a half space of 0.01 S/m. For a unit step-off excitation, Fig. 5 (c) shows the computed voltages for a centered receiver loop of 0.1 m × 0.1 m. This verifies the A-potential based integral in Eq. (24).

We now turn to the problem of computing the secondary magnetic flux or voltage induced by an object. Considering only the ECR term in Eq. (12) and integrating over the loop surface oriented in a unit direction $\mathbf{n}$, we have

$$\int_{Rx} \mathbf{H}_{\text{sca}}(\mathbf{r}_{Rx}, \omega) \cdot \mathbf{n} dS_{Rx} = \left[\int_{Rx} \mathbf{n} \cdot \mathbf{G}_{23}(\mathbf{r}_{Rx}, \mathbf{r}', \omega) dS_{Rx} \right] \mathbf{P}_m(\mathbf{r}', \omega) \hat{\mathbf{H}}(\mathbf{r}', \mathbf{r}_{Tx}, \omega), \tag{25}$$

where dS_{Rx} is the area element of a receiver loop. Here $\mathbf{G}_{23}(\mathbf{r}_{Rx}, \mathbf{r}', \omega)$ is specifically used to represent a magnetic Green's tensor for a case where a source is in region 3 and a field point in region 2 (Fig. 1).

Recall the Lorentz reciprocity theorem (Harrington, 2001),

$$\mathbf{G}_{23}^T(\mathbf{r}_{Rx}, \mathbf{r}', \omega) = \mathbf{G}_{32}(\mathbf{r}', \mathbf{r}_{Rx}, \omega),$$

which states that the fields in medium 2 for source in medium 3 can be obtained as the fields $\mathbf{G}_{32}$ received in medium 3 as the source is in medium 2. Thus we can transform the term in the bracket of Eq. (25) to

$$\int_{Rx} \mathbf{G}_{23}^T(\mathbf{r}_{Rx}, \mathbf{r}', \omega) \mathbf{n} dS_{Rx} = \int_{Rx} \mathbf{G}_{32}(\mathbf{r}', \mathbf{r}_{Rx}, \omega) \mathbf{n} dS_{Rx} = \int_{Rx} \mathbf{H}_{m,\mathbf{n}}(\mathbf{r}', \mathbf{r}_{Rx}, \omega) dS_{Rx}, \tag{26}$$

where $\mathbf{H}_{m,\mathbf{n}} = \mathbf{G}_{32}(\mathbf{r}', \mathbf{r}_{Rx}, \omega) \mathbf{n}$ is the vectorial field generated by a magnetic dipole source oriented in $\mathbf{n}$, i.e., parallel to the normal of the Rx loop. Similar to Eq. (21) that is for a Tx loop, we perform a surface integration over a tri-axial Rx loop with its normal direction given in three coordinates $\mathbf{n} = \hat{\mathbf{x}}, \hat{\mathbf{y}}, \hat{\mathbf{z}}$. Again, the 2-dimensional surface computation in Eq. (26) can be converted into a line integral along a Rx loop, i.e.,

$$\hat{\mathbf{H}}(\mathbf{r}', \mathbf{r}_{Rx}, \omega) = \int_{Rx} \mathbf{H}_{m,\mathbf{n}}(\mathbf{r}', \mathbf{r}_{Rx}, \omega) dS_{Rx} = \int_{Rx} \mathbf{H}_{e,\mathbf{n}}(\mathbf{r}', \mathbf{r}_{Rx}, \omega) dl_{Rx}, \tag{27}$$

where $\mathbf{H}_{e,\mathbf{n}}(\mathbf{r}', \mathbf{r}_{Rx}, \omega)$ is the field that would be produced by the electric current elements associated with a $\mathbf{n}$-directed loop. For a z-directed rectangular Rx loop, we perform numerical integrations over four line segments along x and y directions; for a x-directed rectangular Rx loop, we need y-and z-directed electrical dipole line integrations. $\hat{\mathbf{H}}(\mathbf{r}', \mathbf{r}_{Rx}, \omega)$ in Eq. (27) can be viewed as the magnetic field at the target location $\mathbf{r}'$ produced by a $\mathbf{n}$-directed receiver loop as if a unit current is flowing. With Eq. (27), the secondary flux of Eq. (25) can be re-written compactly as

$$\Phi_{\mathrm{sca}}(\mathbf{r}_{Rx}, \omega) = \hat{\mathbf{H}}(\mathbf{r}', \mathbf{r}_{Rx}, \omega) \cdot \mathbf{P}_m(\mathbf{r}', \omega)\hat{\mathbf{H}}(\mathbf{r}', \mathbf{r}_{Tx}, \omega), \qquad (28)$$

where $\Phi_{\mathrm{sca}}(\mathbf{r}_{Rx}, \omega) = \int_{Rx} \mathbf{H}_{sca}(\mathbf{r}_{Rx}, \omega) \cdot \mathbf{n} dS_{Rx}$. Note that the polarizability tensor $\mathbf{P}_m(\mathbf{r}', \omega)$ in Eq. (28) is spatially invariant. The argument $\mathbf{r}'$ in it is used to merely indicate where an associated object is present.

We have had a complete description of the integral equation technique in a layered medium for loop transmitters and receivers. Next we present various synthetic experiments that aim to improve our understanding of the transient responses that occur in the marine UXO sensing.
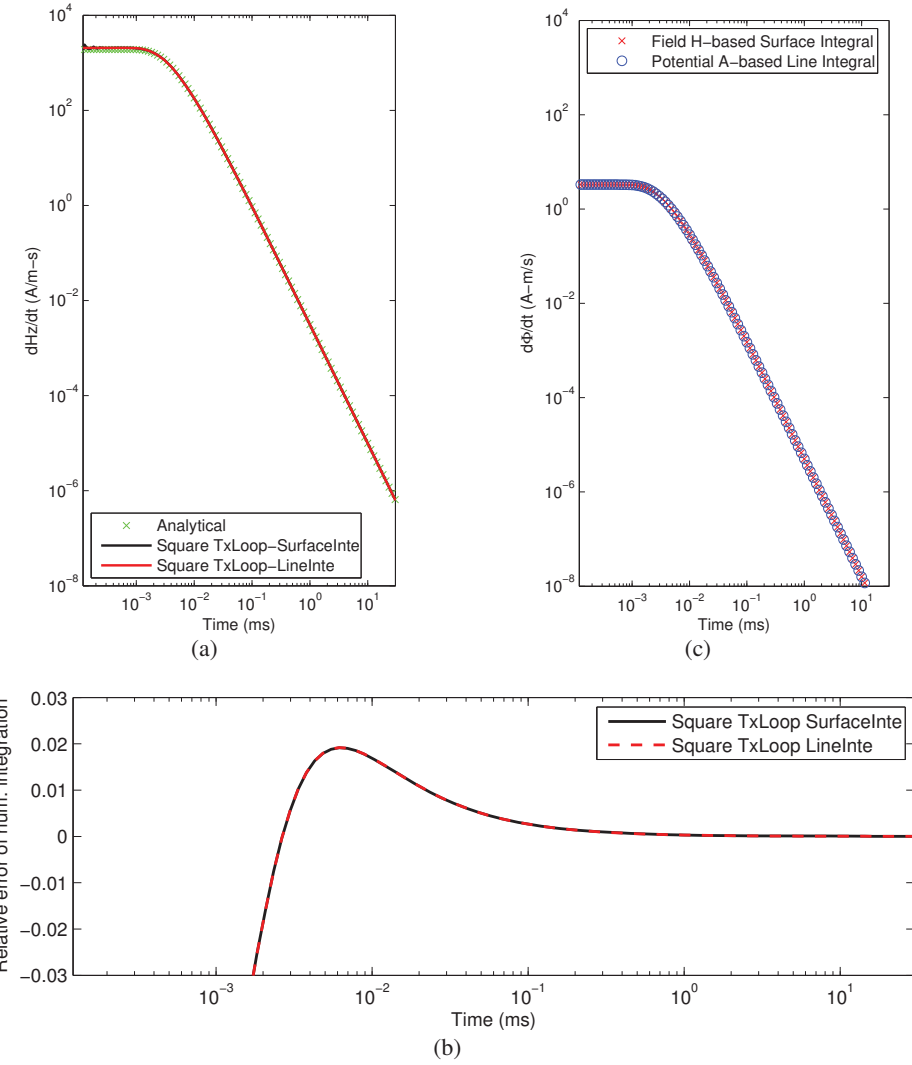
Figure 5: A check of computing fields at the center of a circular loop of radius 50 m on a 0.01 S/m of homogeneous half space. (a) Surface and line numerical integrations and analytical responses. (b) Calculating primary voltage with Eq. (24). (c) Relative errors between numerical and analytical results in (a).

3 Synthetic Experiments

In the following numerical studies, we model the marine environment by using the electromagnetic parameters: $\sigma_1 = 0$ S/m, $\mu_{r1} = 1$; $\sigma_2 = 4$ S/m, $\mu_{r2} = 1$; $\sigma_3 = 0.4$ S/m, $\mu_{r3} = 1$, which represent the air, sea, and the sediment, respectively. The air-sea interface is set at $z_1 = 0$ m and the sea-sediment interface z_2 (and hence d_{sea} the water depth) can vary from 2 m to 20 m in the simulation. Fig. 6 schematically shows the three underwater sensing setups where we will investigate how background and scattered responses behave and vary with respect to the conductivity and depth of the seawater, the size of a transmitter loop, sensing height and offset. In addition, we will study the field dispersion with respect to pulse width and shape of an excitation current and field characteristics of an insulated VMD. We also invert simulated marine TEMTADS 2x2 scattered data.

3.1 Effects of sea depths on responses

First, we test how the background and scattered responses will be affected by increasing sea depth d_{sea} from 2 m to 20 m while other parameters are fixed. In Fig. 6 (a), a square Tx loop of 0.35 m
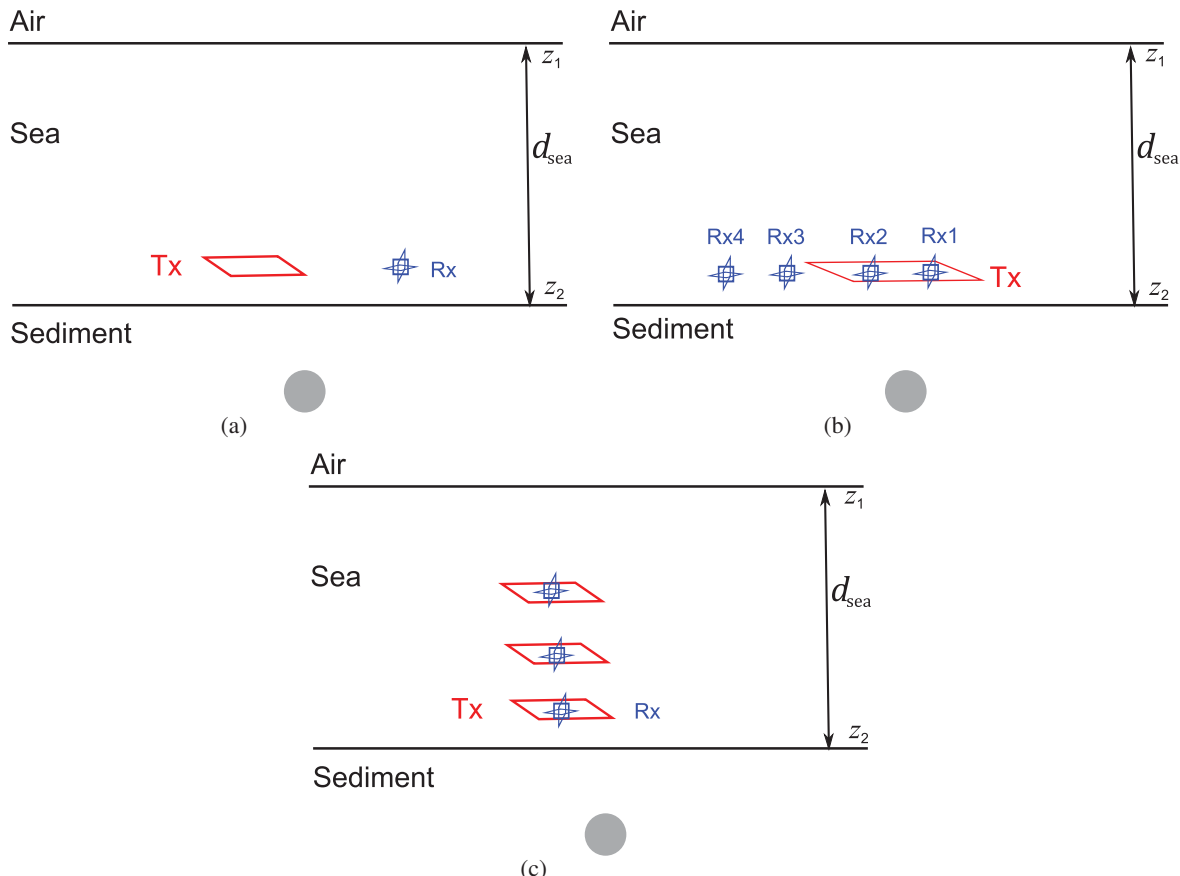
Figure 6: Schematic setups of Tx and Rx loops immersed in the seawater for synthetic experiments. (a) Studying responses by varying sea depths $d_{\text{sea}} = 2, 5, 10, 20$ m. (b) Studying responses by varying $x_{\text{Rx}} = 0.4$ m, -0.4 m, -1.2 m, and -1.7 m. $d_{\text{sea}} = 6$ m. (c) Studying the responses by varying sensor height $h = 0.5$ m, 1.0 m, and 1.5 m and using the Tx loop size: 0.5 m × 0.5 m, 1 m × 1 m, and 2 m × 2 m. $d_{\text{sea}} = 10$ m. The conductivity of seawater is $\sigma_2 = 4$ S/m and the sediment $\sigma_3 = 0.4$ S/m.
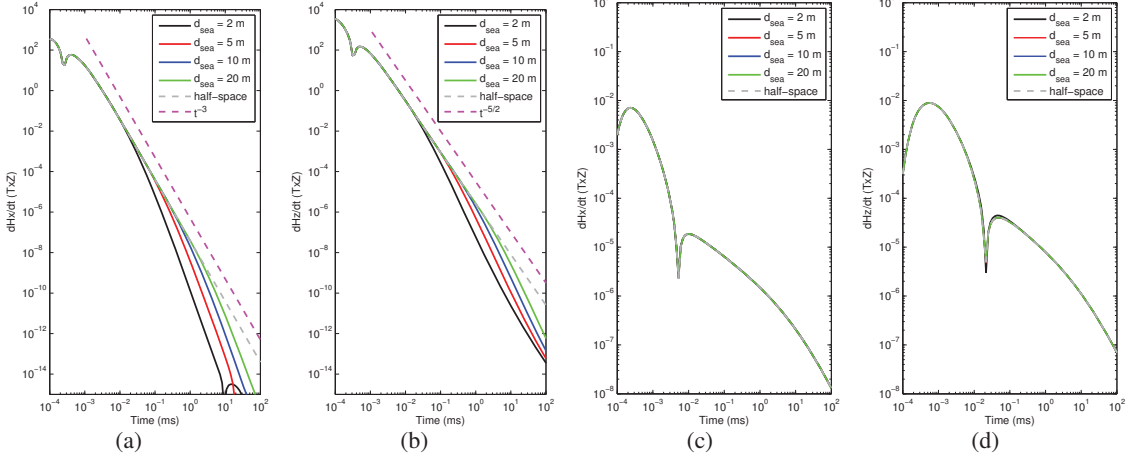
Figure 7: Effects of sea depths on the responses with the setup in Fig. 6 (a). Background: (a) dH_x/dt; (b) dH_z/dt. Scattered: (a) dH_x/dt; (b) dH_z/dt. A square Tx loop of 0.35 m × 0.35 m and a small tri-axial cube of 0.1m^3 are used. The center of the Tx is at $\mathbf{r}_{Tx} = (-0.2, 0.2, h)$ m, the center of the Rx at $\mathbf{r}_{Rx} = (0.2, -0.2, h)$ m, sensor height $h = 0.2$ m. The sphere is with the radius of $a = 0.30$ m, $\sigma = 3.5 \times 10^7$; $\mu_r = 300$. Its center is at $\mathbf{r} = (0.05, 0.05, d_{\text{sea}} + 2)$ m. The half space represents a sea-sediment, approximately equivalent to a very deep sea scenario.

× 0.35 m and a small tri-axial cube of 0.1m^3 are immersed in the sea. The sensor height is $h = 0.2$ m above the seafloor. The center of the Tx is at $\mathbf{r}_{Tx} = (-0.2, 0.2, d_{\text{sea}} - h)$, the center of the Rx at $\mathbf{r}_{Rx} = (0.2, -0.2, d_{\text{sea}} - h)$ m. A deep steel sphere is buried at a depth of 2 m below the seafloor with the radius of $a = 0.30$ m and $\sigma = 3.5 \times 10^7$ and $\mu_r = 300$. The object is located at $\mathbf{r} = (0.05, 0.05, d_{\text{sea}} + 2)$ m.

For the background responses shown in Figs. (7) (a) and (b), we see that after ~ 0.1 ms both dH_x/dt and dH_z/dt decay at different rates for different sea depths. The shallower the sea depth, the faster the decay of the background response. With increasing sea depth, the horizontal and vertical background responses increase and asymptotically approach those of a half-space (gray dashed: resembling a deep sea of greater than 50 m water depth) with decay rate following t^{-3} and $t^{-5/2}$. The results illustrate that the air-sea interface effects become apparent after a time dictated by the sea depth. The deeper the sea, the later in time before the interface effect becomes apparent. For a deep sea, the decreasing effect of the air-ocean interface may be explained by the significant reduction of the downward amplitude coefficient A_2 in Sec 2.2. For a shallow water case, the presence of the air-sea interface diminishes the background response.

3.2 Effects of receiver offset position on background response

We now examine how the EMI background and target signals can vary with different Tx-Rx offset and sensor-target distance. In this test (Fig. 6 (b)), we simulate a rectangular Tx loop of 2 m × 1 m immersed in the sea ($d_{\text{sea}} = 6$ m). The center of the Tx is at $\mathbf{r}_{Tx} = (0.0, 0.0, d_{\text{sea}} - h)$. The measurements are taken along the x-axis at $x_{Rx} = 0.4$ m, -0.4 m, -1.2 m, -1.7 m and are marked as Rx_1, Rx_2, Rx_3, Rx_4. The sensor height is $h = 0.5$ m above the seafloor.

Figs. 8 (a) show the horizontal component response. Outside the Tx loop, the response appears to shift slightly to late time relative to those inside. The sign reversals occur twice in this time range. Overall, the background responses inside and outside the transmitter loop decay with a similar pattern.
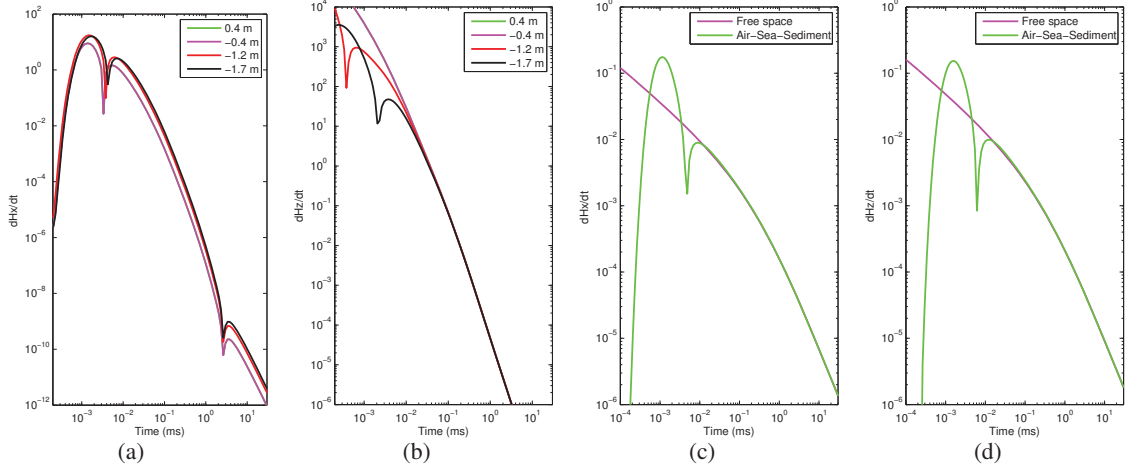
Figure 8: Background responses varying with the Rx offsets in Fig. 6 (b): (a) dH_x/dt; (b) dH_z/dt. Scattered response at Rx2 in Fig. 6 (b) in free space and air-sea-sediment media: (c) dH_x/dt. (d) dH_z/dt. A z-directed Tx loop of 2 m × 1 m and and a small tri-axial cube of 0.15m^3 are used. The sensor height h = 0.5 m. The center of the Tx is at $\mathbf{r}_{Tx} = (0.0, 0.0, h)$ m, the center of the Rx at $\mathbf{r}_{Rx} = (x_{\text{Rx}}, 0.0, h)$ m. The sphere is with the radius of $a = 0.05$ m, $\sigma = 3.5 \times 10^7$; $\mu_r = 300$. Its center is at $\mathbf{r} = (0.05, 0.05, d_{\text{sea}} + 0.3)$ m.

The pattern of the vertical component responses in Figs. 8 (b) looks different from the horizontal ones. The sign reversals of the fields only occur for the measurements outside the Tx loop and appear at different times for different Rx horizontal offset. These can be explained by the concept of the "smoke ring" that qualitatively describe the diffusion of the induced current loop when a primary current is turned off (Nabighian, 1979). As the smoke ring diffuses outward and its maximum passes through an observation point, the associated magnetic field flips sign. For the observation farther away from the Tx, say $x_{Rx} = -1.7$ m, the corresponding sign changes significantly later than the one at $x_{Rx} = -1.2$ m. But after about 0.3 ms in this example, all vertical background responses either inside or outside are virtually identical. This would be expected physically as those observations sense the diffusion from a smoke ring of ever increasing diameter. These results indicate that background removal for the vertical field may be quite straightforward in the marine environment, for times greater than 0.3 ms.

For the same Tx-Rx loop setup, we consider the scattered responses measured at Rx2 from a sphere buried at a depth of 0.3 m below the seafloor. The sphere is with the radius of $a = 0.05$ m and $\sigma = 3.5 \times 10^7$ and $\mu_r = 300$. It is located at $\mathbf{r} = (0.05, 0.05, d_{\text{sea}} + 0.3)$ m. Figs 8 (c) and (d) show the horizontal and vertical fields for the two backgrounds: free space and the air-sea-sediment. The scattered responses of the sphere embedded in the air-sea-sediment exhibit early-time sign reversals. After ~ 0.1 ms, the scattered response for the sphere in the full marine environment approaches the response observed in free space. These scattered field observations are consistent with the results for point transmitters and receivers immersed in the sea (Song et al., 2016), other numerical investigations in a uniform conducting medium (Shubitidze et al., 2008), and recent experimental observations (Bell et al., 2016) in a large salt water tank. Namely, the transient scattered responses of the sphere embedded in free-space or within a uniform or layered conducting backgrounds all have approximately the same late-time behaviour. Again, this implies that we can assume a free-space background to compute the secondary field response.

3.3 Effects of Tx loop size and stand-off distance

In this section, we investigate the EMI response in an underwater environment with a transmitter loop having different sizes: 0.5 m × 0.5 m; 1 m × 1 m; and 2 m × 1 m. The measurements in Fig. 6 (c) are simulated at three stand-off distances above the sea floor: $h = 0.5$ m, $h = 1$ m, and $h = 1.5$ m for each Tx loop. Figs. 9 (a) and (d) shows the horizontal and vertical background and scattered responses at $h = 0.5$ m. Since the Rx cube is centered at the Tx loop, there is no horizontal background response. One can see that a large Tx loop (e.g. 2 m × 1 m) excites a stronger scattered response than with a small loop (e.g. 0.5 m × 0.5 m). In particular, for the larger stand-off distance of 1 m and 1.5 m, the benefit of increasing scattered response becomes pronounced with a larger Tx loop (see Figs. 9 (b)-(e) and Figs. 9 (c)-(f)). However, a larger Tx loop can also generate a larger background response as well. But this side effect can be mitigated by an appropriate background removal approach. We will discuss this in the next section.

When increasing the sensor-target distance, we know that the amplitude response from a target will decrease for a given loop. There are other effects of the conductive background as can be seen in Figs. 9 (a)-(c) for the horizontal responses and Figs. 9 (d)-(f) for the vertical responses at the three sensor heights: $h = 0.5$ m to $h = 1$ m to $h = 1.5$ m. As the stand-off distance increases we see a "delay propagation" effect in a conducting medium for the target response. This is most evident by looking at the times when the responses change sign. For the 2 m × 1 m loop case, sign reversal of the vertical component occurs at 0.004 ms, 0.009 ms, and 0.015 ms for $h = 0.5$ m, $h = 1$ m, and $h = 1.5$ m, respectively.

3.4 Differential Measurements: Background Removal

We have learned that the scattered responses from a highly conducting and permeable sphere in a layered conducting medium approach those in free space at late times. However, practical measurements are of total fields that are the sum of the background and scattered fields in Eq. (2). To obtain the scattered responses, one has to remove the background field from the observed field. In terrestrial environments, background measurements are collected in target-free regions that are assumed to be identical with the surroundings of the target-of-interest and background correction is a simple case of subtraction. In this section we experiment with alternative background mitigation strategies that utilise differential measurements across the different receivers.

One potential configuration in Fig. 10 (a) is to positions 4 receiver loops along the z-axis of a Tx loop. Sequentially, the 4 receivers are marked as Rx1, Rx2, Rx3, and Rx4. Their heights relative to the Tx plane are 0.0 m, 0.5 m, 1.0 m, 2 m, respectively. Fig. 10 (b) shows the background (dashed) and scattered (solid) responses. The background responses measured at different heights of Rx are virtually identical for times exceeding 0.01 ms. The target response dominants the background response for the centered Rx after $\sim$ 1 ms. To subtract the background signals from the measurements, we form the differential combinations of Rx1-Rx2, Rx1-Rx3, and Rx1-Rx4. The corresponding quantities, e.g., between Rx1-Rx4, will be referred to as `D14ZZ-sca`, `D14ZZ-bkg`, and `D14ZZ-tot` to represent the differential scattered, background, and the total z-components, respectively. The same notation rule applies to the other Rx combinations. Fig. 10 (c) and (d) shows the differential responses derived from the three combinations. The differential scattered responses become stronger than the differential background earlier than 1 ms. The differential total response overlaps well with the the the differential scattered response after 0.3 ms. These experiments show that the top-bottom Rx configuration provides a possible way to mitigate the background signals.

Next we look at an alternative way to remove background signals by using radially distributed receivers. As expressed in the spectral representations in Sec. 2.2 the background EM fields from
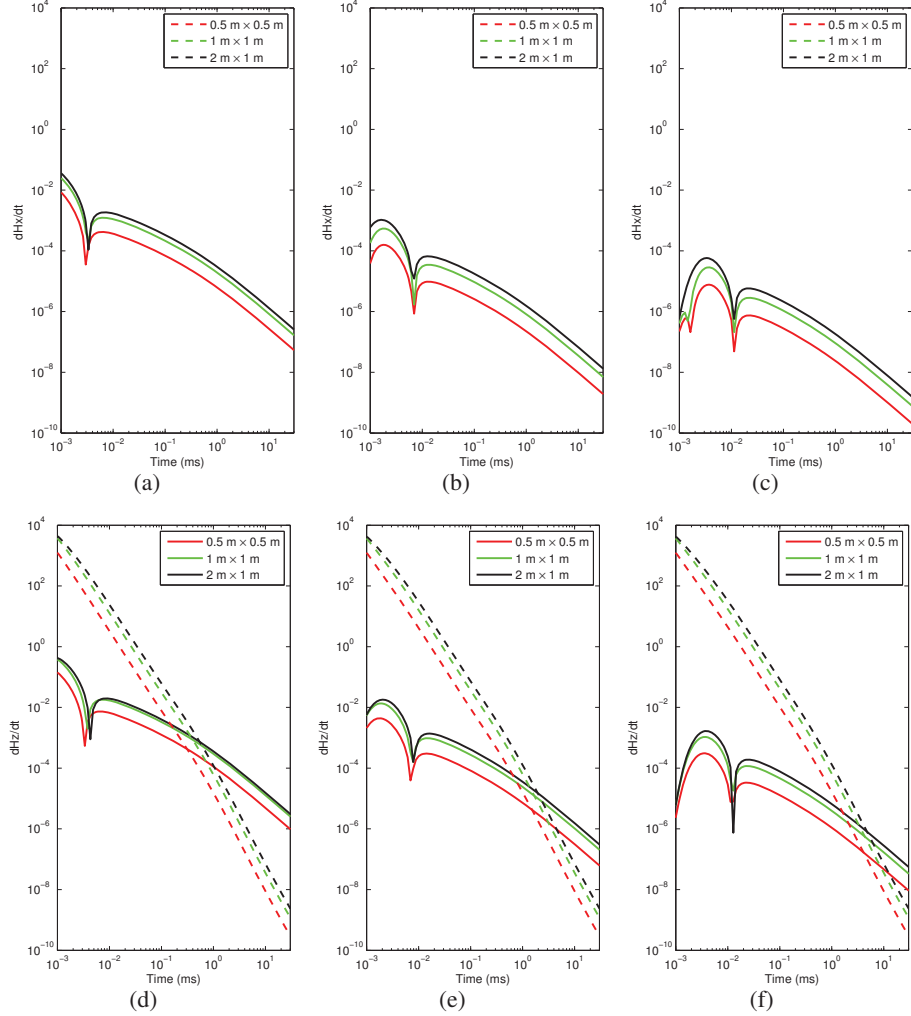
Figure 9: Background (dashed) and scattered (solid) responses varying with Tx loop size and sensor height h in Fig. 6 (c). dH_x/dt: (a) h = 0.5 m; (b) 1 m; (c) 1.5 m. dH_z/dt: (d) h= 0.5 m; (e) 1 m; (f) 1.5 m. The centers of the Tx and the Rx are $\mathbf{r}_{Tx} = \mathbf{r}_{Rx} = (0.0, 0.0, h)$ m. The parameters of the sphere and the Rx loop are the same as those used in Fig. 8. Notice that the geometrical symmetry of the centered Rx w.r.t the Tx makes the background response dH_x/dt vanished.

both the dipole and loop source excitations are the superposition of cylindrical wave functions that propagate vertically in the form of $e^{\pm\gamma z}$ and are modulated by an oscillatory Bessel function $J_0(\lambda\rho)$ or $J_1(\lambda\rho)$ at a radial distance ρ. This means that, for a given excitation, the observed background fields would be the same at two different points as long as they are at the same height and keep the same distances ρ to the source. Using this distance-dependent EM field characteristic we can develop ca background suppression method. Previously we used point transmitters and receivers to demonstrate background removal feasibility by arranging two receiver cubes so they are radially symmetric with respect to a transmitter loop (Song et al., 2016). Following that numerical experiment, we conceived a prototype marine concept [2] shown in Fig. 11, which consists of a loops with a size 1.8 m × 1.8 m and multiple receivers cubes that are 0.15 m × 0.15 m × 0.15 m. The receivers are arranged symmetrically about the transmitter.

[2]The Tx-Rx arrangement shown is just one part of a larger multi-Tx, multi-Rx system
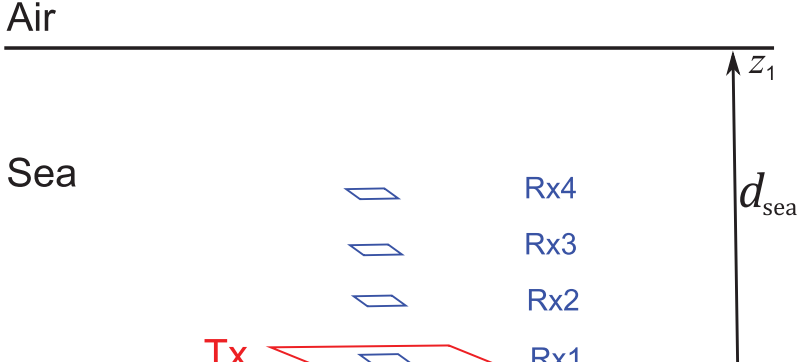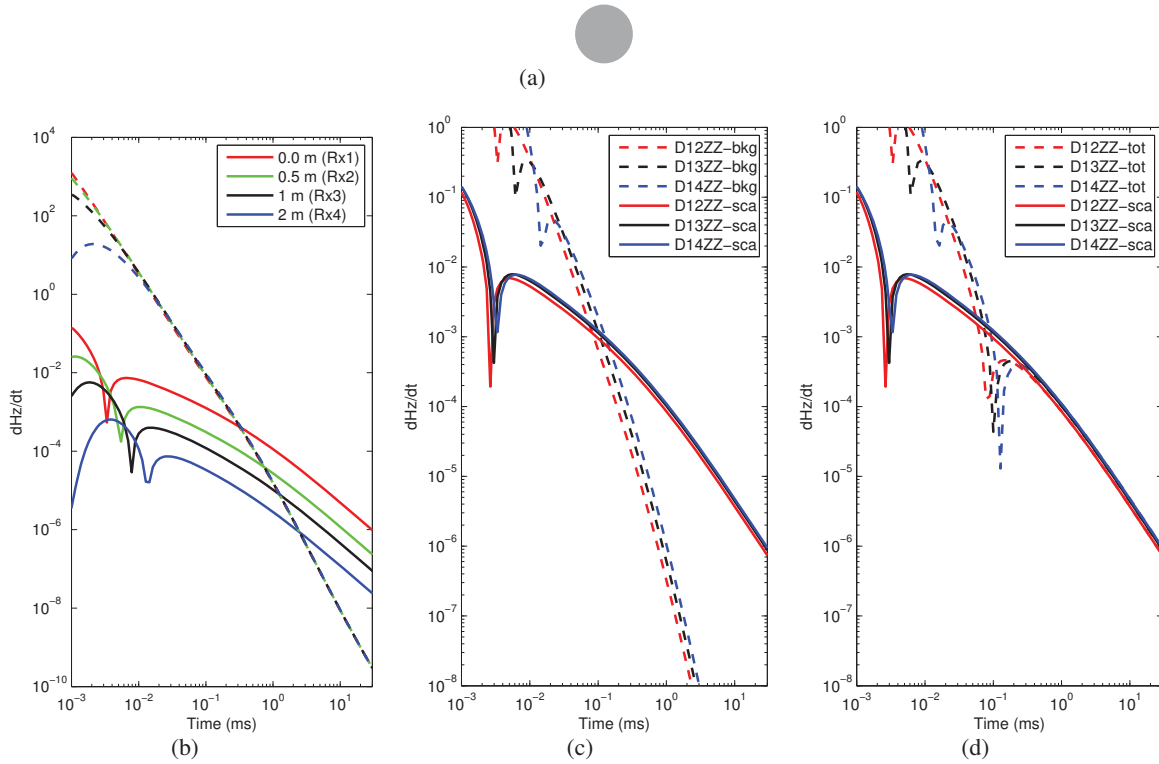
Figure 10: Experiment of differential measurements. (a) Setup of vertical offsets of a small Rx coil of 0.15 m × 0.15 m at $z_{Rx} = 0.0$ m, 0.5 m, 1.0 m, 2 m relative to the Tx loop of of 2 m × 1 m. (b) Background (dashed-lines) and scattered (solid-lines) responses for all Rxs. (c) Differential background and scattered responses. (d) Differential total and scattered responses. The three-layer parameter: $\sigma_1 = 0$ S/m, $\sigma_2 = 4$ S/m, $\sigma_3 = 0.4$ S/m; $d_{sea} = 10$ m. `D12ZZ-bkg`, `D12ZZ-sca`, and `D12ZZ-tot` denotes the differential responses between the the background, the scattered, and the total z-components in the three-layered medium. The same notation rule applies to other Rx pairs. The parameters of the sphere are the same as those used in Fig. 8.

For illustration, we assume in Fig. 11 that the small red circle in the figure represents the projected position of a spherical object. With respect to this Tx, we can form many pairs of symmetric receivers that theoretically have the same EM background fields due to the symmetrical distribution of receivers. For example, the pairs of Rx1 and Rx5, and of Rx7 and Rx9. In each subplot of Fig. 12, the gray
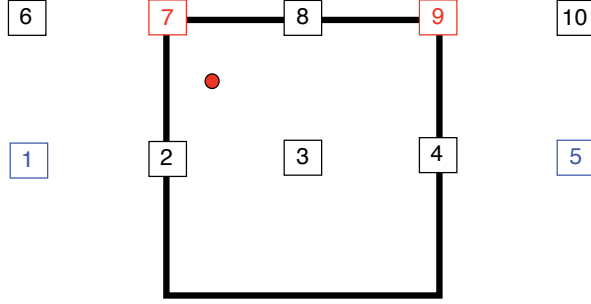
Figure 11: A plane view of marine sensor system concept that consists of a 1.8 m × 1.8 m transmitter and multiple receiver cubes (each 0.15 m × 0.15 m × 0.15 m) distributed symmetrically about the transmitter loop. The center of the Tx is at $\mathbf{r}_{Tx1} = (0.0, 0.9, h)$ m. The sensor height $h = 0.3$ m. The parameters of a conducting and permeable sphere: $a = 0.25$ m; $\sigma = 3.5 \times 10^7$; $\mu_r = 300$. Its center is at $\mathbf{r} = (-0.71, 1.45, d_{\text{sea}} + 2)$ m and $d_{\text{sea}} = 10$ m. The small circle denotes the projected position of a spherical object in the experiment.

curves represent all measured responses and red and black curves are used to highlight the responses associated with a particular Rx. We see that the background fields can significantly mask the scattered fields before 1 ms or even later. Yet the strong background fields are identical across Rx1 and Rx5, as well as across Rx7 and Rx9. Conceptually, combining recordings between these cubes could provide a gradiometer type measurement which would completely remove the background signals.

Fig. 13 presents the differential responses between the receivers of Rx1 and Rx5. In the subplots, `D15XX-sca` denotes the differential measurements between the scattered x-components in the three-layered medium, `D15XX-tot` the total $x-$ component in the three-layered medium. The same notation rule applies to the y- and z-components and other receiving combination like Rx7 and Rx9.

Since the background fields in the marine enviroment can be canceled out across the two symmetrical receivers, the three differential components derived from the *total fields* of Rx1 and Rx5 overlap completely with the differential ones from the pure *scattered responses* at the two receivers (Fig. 13 (a)-(c)). The same differential results for Rx7 and Rx9 can be achieved for the three components (Fig. 13 (d)-(f)). The experiments show that the differential measurements from a pair of symmetrical receivers completely suppress the background fields from the conductive seawater. We know that within the interesting time range of 0.1 ms $\sim$ 25 ms, the scattered responses in a layered conducting medium approach those in free space. Thus differential responses can be modelled as if the measurements occur in free-space. Therefore their use can make underwater EMI inversion processing as simple as the land-based case.

3.5   Dispersion of Electromagnetic fields in seawater

In the above modelling and simulation work, we characterized the fundamental background and scattered responses to a conducting layered medium and a target under an ideal step-off current excitation. In reality, a realizable current source generates an exponentially increasing current flow within a transmitter loop. The electromagnetic response due to a pulse-like excitation has been known to be dispersed in a conducting medium (Wait, 1953). The resulting broadening and delay due to conductivity and observation distance may impact underwater EMI sensing of metallic objects. To clarify these questions and better understand the propagation of the transient response due to a pulse excitation, we present a dispersion analysis with a VMD or a loop transmitter embedded in uniform conducting medium (conductivity of 4 S/m) and a three-layered medium (air-seawater-sediment).

Consider the transient response to an arbitrary current excitation $I(t)$ and a causal step-off re-
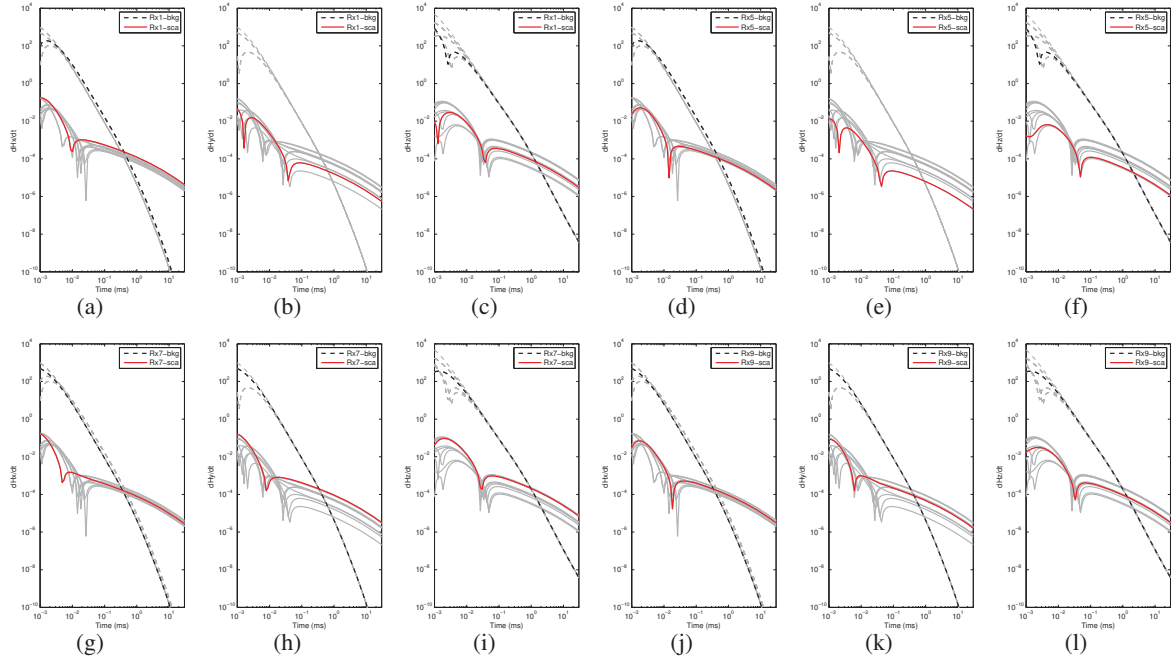
Figure 12: Background and scattered responses in all three components measured from the marine system in Fig. 11. Rx1: (a)-(c). Rx5: (d)-(f). Rx7: (g)-(i). Rx9: (j)-(l).

sponse for a system $a(t)$ (Song et al., 2008), the field $b(t)$ and its time-derivative are given by

$$b(t) = -\int_0^t a'(t - \tau)I(\tau)d\tau - a(0)I(t), \tag{29}$$

and

$$\frac{db(t)}{dt} = -\int_0^t a'(t - \tau)I'(\tau)d\tau - a(0)I'(t) - a'(t)I(0). \tag{30}$$

The prime $'$ denotes differentiation. The above equations are sufficiently general for computing either the off-time or on-time response for an arbitrary transmitter waveform. Here the terms off- and on-time represent measurement times taken when the transmitter current source is either on or off. The pulse $I(t)$ function we consider can be rectangular, trapezoidal, or mixed with an exponential rise time and a linear ramp-off time.

To begin, we consider a simple case where the field response can be described by an analytical expression. That is, a VMD embedded in a uniform conducting medium is excited by a unit rectangular current function $I(t)$

$$I(t) = \begin{cases} 0 & \text{for } t < 0, \\ 1 & \text{for } 0 < t < t_w, \\ 0 & \text{for } t > t_w \end{cases} \tag{31}$$

where t_w is the pulse width. In the spherical coordinate system, the magnetic field response at a distance r from the VMD in $\hat{\theta}$ direction is given by (Wait, 1953)

$$H_\theta(r, t) = \frac{m_0}{4\pi r^3} \sin\theta R_\theta(t), \tag{32}$$
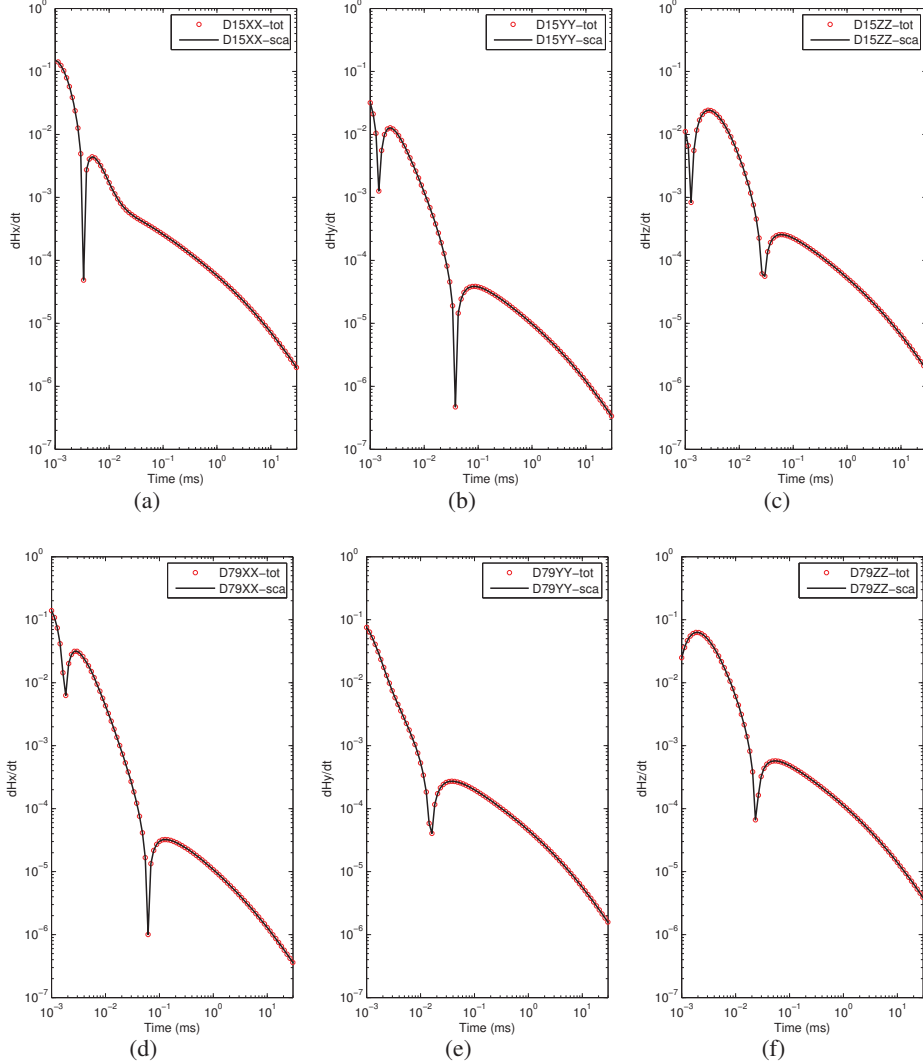
Figure 13: Differential Responses derived from those in Fig. 12. For Rx1-Rx5 pair: (a) x-component; (b) y-component; (c) z-component. For Rx7-Rx9 pair: (d) x-component; (e) y-component; (f) z-component. `D15XX-tot` and `D15XX-sca` denote the differential responses between the scattered and the total x-components in the three-layered medium. The same notation rule applies to the y- and z-components.

where m_0 is the dipole moment and θ is the polar angle. The transient characteristics of the field are described by the function $R_\theta(t)$:

$$R_\theta(t) = \begin{cases} C_\theta(t) & \text{for } 0 < t < t_w \\ C_\theta(t) - C_\theta(t - t_w) & \text{for } t > t_w, \end{cases} \qquad (33)$$

where $C_\theta(t)$ is a step-on response function (Wait, 1953). Eq. (33) shows that the field responses for a dipole excited by a rectangular current can be expressed as a superposition of the two step-function responses. The function $C_\theta(t)$ with $\beta = \frac{\sigma \mu r^2}{4t}$ is given by

$$C_\theta(t) = \text{erfc}(\beta) + 2\pi^{-\frac{1}{2}}(\beta + 2\beta^3)\exp(-\beta^2), \qquad (34)$$

where $\mathrm{erfc}(\beta)$ is the complement of the error function of argument β. Thus we can use $R_\theta(t)$ to examine the behavior of an electromagnetic wave pulse propagating in a conducting medium.

For an exciting rectangular pulse width of $t_w = 10$ ms in Eq. (31), Fig. 14 presents $R_\theta(t)$ for different host media conductivities of $\sigma = 0, 0.2, 1, 2, 4$ S/m. When $r = 20$ m, we can see from Fig. 14 (a) that the shape of the on-time responses for a conductive medium is not rectangular initially. Rather it surges to exceed the source current value and then gradually falls back and settles down. As the conductivity of the host increases, the on-time fields become more spread out and the peak amplitude response is pushed to later in time. Fig. 14 (b) shows these same plots with a logarithmic x-axis. For the off-time responses shown in Fig. 14 (c), we see that the effects of increasing conductivity delay the responses and sign reversals to a later time. These analytical off-time results are consistent with those of the numerical simulation (Song et al., 2016). When considering a smaller observation distance $r = 2$ m and contrasting with Figs. 14 (a) and (b), we observe that in Figs. 14 (d) and (e) that the on-time field disperses in a narrow early time range and quickly approaches that of the source waveform. For a near-field observation, the decaying off-time responses in Fig. 14 (f) also shift toward
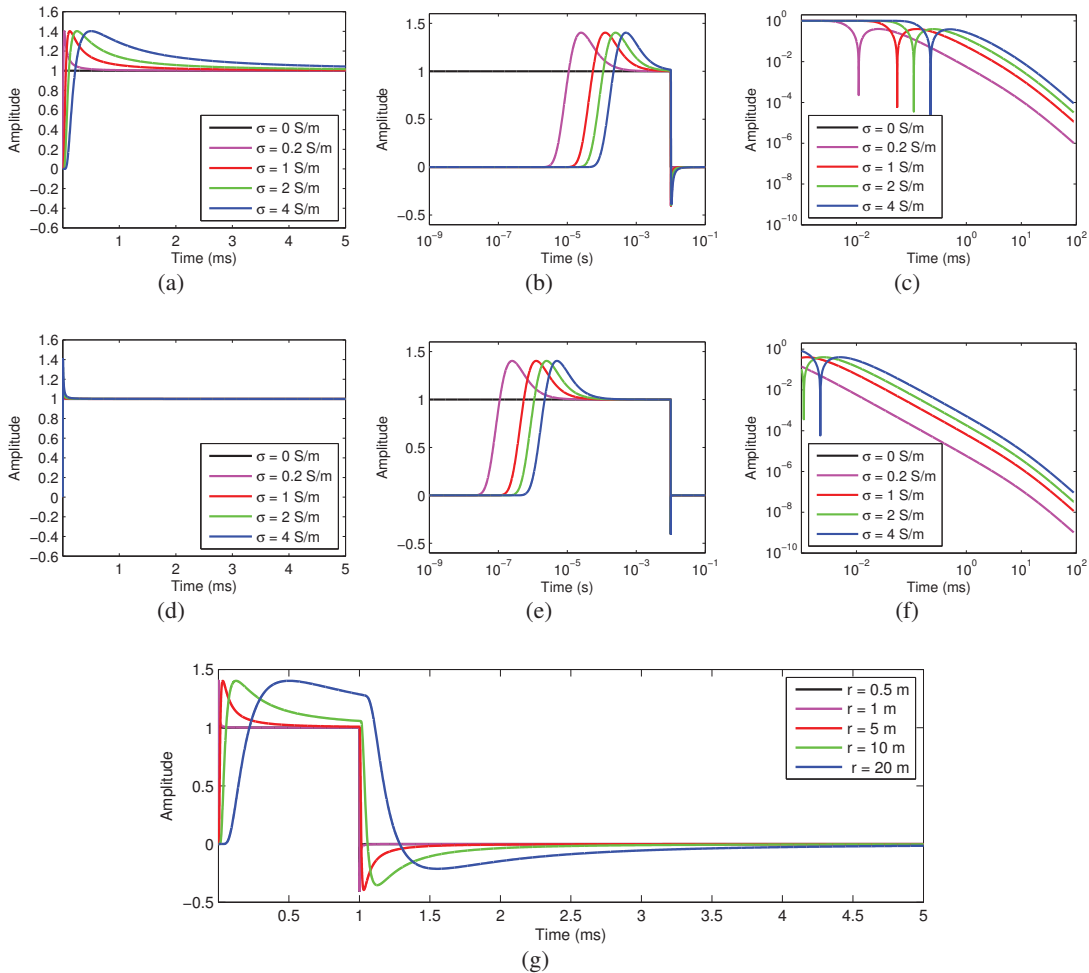
Figure 14: Field dispersion function $R_\theta(t)$ w.r.t. conductivities for $t_w = 10$ ms. $r = 20$ m: (a) Linear scale. (b) Semilogx scale. (c) Off-time response. $r = 2$ m: (d) Linear scale. (e) Semilogx scale. (f) Off-time response. (g) Field dispersion function $R_\theta(t)$ w.r.t. distances for conductivity of 4 S/m and $t_w = 1$ ms.

early times as compared with Fig. 14 (c). This shows that propagation effects in a conducting medium displays similar characteristics to the stand-off distance effects studied in Sec. 3.2 using a step-off waveform.

For a short rectangular pulse of 1 ms, Fig. 14 (g) shows the dispersion with different observation distances from 0.5 m to 20 m for the medium conductivity of 4 S/m. These results indicate that, for a given conductivity, the field dispersion phenomena can become significant for larger observation distances. But for our typical sensing range within 1 or 2 m, the on-time dispersion virtually disappears by the end of the on-time for pulse width as short as 1 ms. This means the on-time field dispersion is unlikely to be of concern when dealing with rectangular pulse source functions.

Let us now examine an more realistic pulse waveform comprising an exponentially rising on-time and linear-ramp off defined as:

$$
I(t) = \begin{cases}
0 & \text{for } t < 0, \\
1 - e^{-t/\tau} & \text{for } 0 < t < t_w, \\
1 - \frac{1}{t_b}(t - t_w) & \text{for } t_w \leq t < t_w + t_b, \\
0 & \text{for } t > t_w + t_b
\end{cases}
\tag{35}
$$

where τ and t_b are a time constant and slope that control how fast a current is switched on and off. With small τ and t_b values, $I(t)$ in Eq. (35) approaches an ideal rectangular pulse. We simulate four different source waveforms given $t_w = 10$ ms: (a) rectangular; (b) $\tau = 0.5$ ms, $t_b = 50\mu$s; (c) $\tau = 1$ ms, $t_b = 50\mu$s; (d) $\tau = 1$ ms, $t_b = 1$ ms, shown in the top row of Fig. 14. For a VMD transmitter in a uniform conducting background of 4 S/m and an observation at $r = 20$ m, we compute the field with Eq. (29) by convolving the waveform function of Eq. (35) with the step-on response in Eq. (34). For a rectangular pulse, the numerical result (bottom) in Fig. 15 (a) is the same as the analytical one in Fig. 14 (a): a dispersion peak appears in the on-time field and overlaps with the step-on response (gray curve). However when a pulse is turned on exponentially with $\tau = 0.5$ ms, the on-time field (bottom) in Fig. 15 (b) ramps up to a small peak. Increasing $\tau = 1$ ms, the dispersion peak is almost completely smoothed out. On the other hand, the off-time responses visually show little changes from $t_b = 50$ μs to $t_b = 1$ ms. These results show that for realistic pulse-waveforms the on-time field dispersion and peak are greatly diminished.

Next we focus on the off-time responses when varying the pulse width. For a uniform conducting medium of 4 S/m, we compute the off-time fields $H_\theta(t)$ at $\theta = 90^0$ and at different observation distance for three pulse widths of $t_w = 1$ ms, $t_w = 10$ ms, and $t_w = 40$ ms. The results are shown in Figs. 16 (a)-(c). For a given pulse, the off-time fields sign reversal observed at each location occur at about the same time for each pulse-width. Also, the off-time responses at different observations locations (0.5 m - 20 m) are approximately the same after a couple of milliseconds. Again the analytical field behavior is similar to the numerical study of offset effects on measured z-components presented in Sec.3.2. The most significant effect of the changing pulse width is the change is the change in the field decay rate. The decay rate $t^{-5/2}$ of an impulse response is shown in each subplot, and it is evident that the decay of the narrow pulse, $t_w = 1$ ms, follows this same relationship. This is to be expected since a narrow pulse more closely resembles an impulse source excitation that do the longer pulses. When increasing the pulse width to $t_w = 10$ ms and $t_w = 40$ ms, we see that the field decay becomes slower. By viewing a rectangular pulse as a summation of two opposite polarities of step-on functions, we can interpret the field as a superposition due to two excitations of different polarity. For a longer pulse duration, the "destructive" superposition occurs later in time. As a result, the field would behave more like the one due to a step-off excitation.
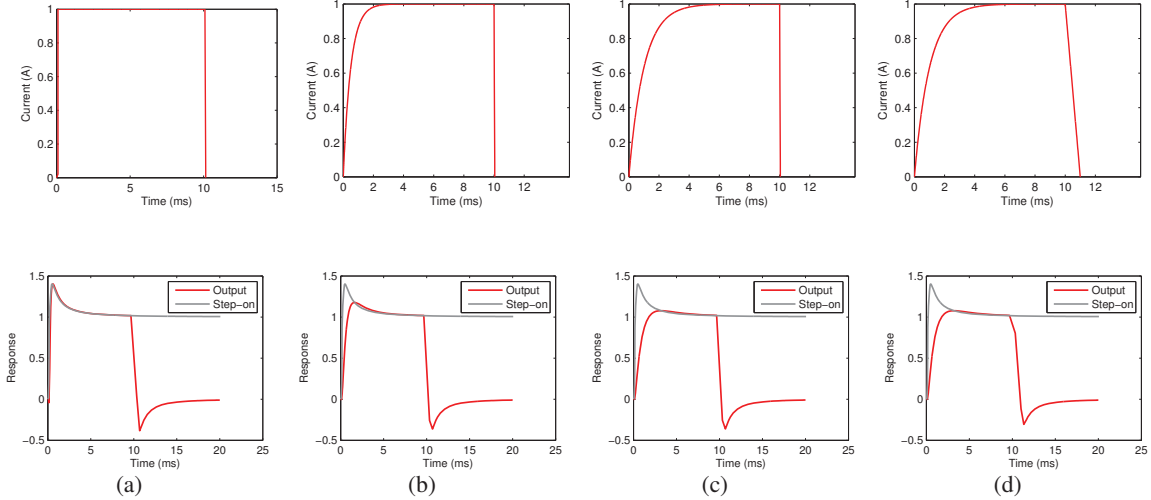
Figure 15: Effects of pulse shape on field dispersion at $r = 20$ m in a uniform medium of $\sigma = 4$ S/m with excitation waveforms on the top and fields on the bottom row. (a) Rectangular pulse. (b) $\tau = 0.5$ ms, $t_b = 50$ μs; (c) $\tau = 1$ ms, $t_b = 50$ μs; (d) $\tau = 1$ ms, $t_b = 1$ ms.
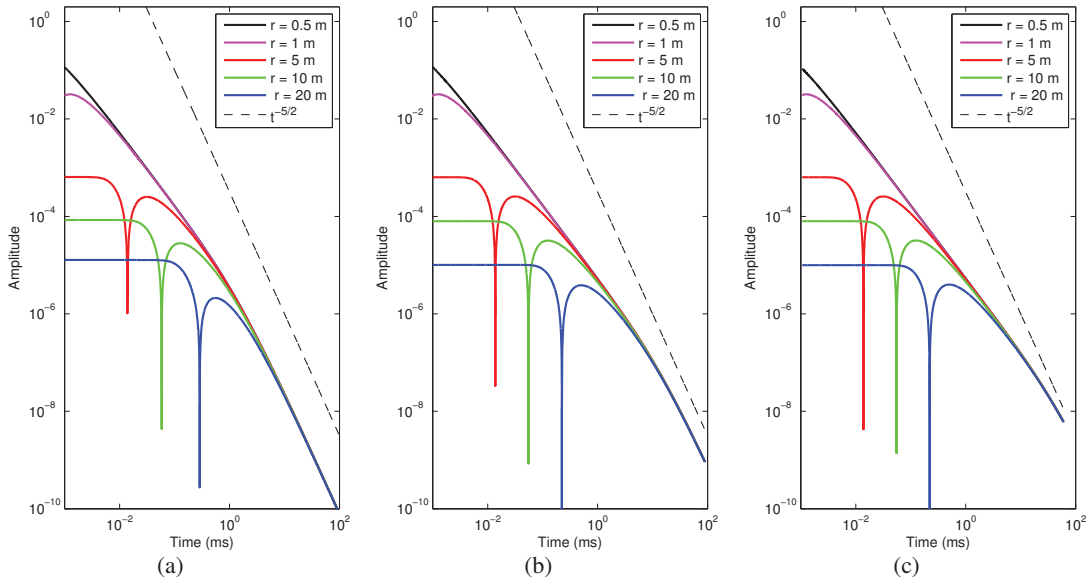
Figure 16: Off-time response $H_\theta(t)$ w.r.t. distances and pulse widths for a uniform conducting medium of 4 S/m. (a) $t_w = 1$ ms. (b) $t_w = 10$ ms. (c) $t_w = 40$ ms.

Next we study the effects of pulse width on the background and scattered fields measured in a marine environment using a rectangular Tx loop. As before, the conductivities of the seawater and sediment are 4 S/m and 0.4 S/m. The sea depth is 6 m and sensor height is 1 m above the sea floor. For a z-directed Tx loop of 2 m $\times$ 1 m and a centered Rx coil of 0.15×0.15 m, we compute the fields with the two rectangular pulse widths of $t_w = 1$ ms and $t_w = 10$ ms by the convolution of Eq. (30). Fig. 17 shows the background and scattered fields including the step-off excitation. Similar to the VMD in an uniform conducting medium, the longer duration of a pulse yields strong or slow decay responses. It also shows that the responses with $t_w = 10$ ms better approximate those of an ideal step-off function and that a longer pulse enhances the target response.
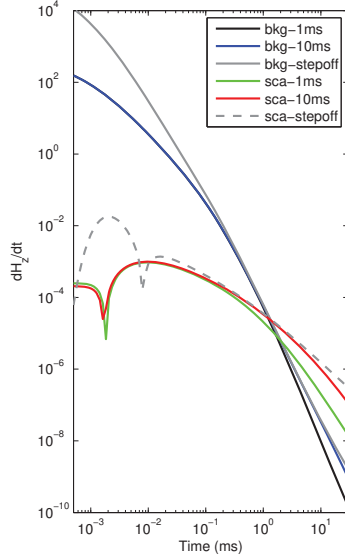
Figure 17: Background and scattered responses with a Tx loop of 2 m $\times$ 1 m and a centered Rx coil of 0.15 m $\times$ 0.15 m. $\mathbf{r}_{Tx} = \mathbf{r}_{Rx} = (0.0, 0.0, d_{\text{sea}} - h)$ m, $h = 1$ m. The three-layer parameters: $\sigma_1 = 0$ S/m, $\sigma_2 = 4$ S/m, $\sigma_3 = 0.4$ S/m, $d_{\text{sea}} = 6$ m. The parameters of a sphere: $\mathbf{r} = (0.05, 0.05, d_{\text{sea}} + 0.30)$ m, $a = 0.05$ m, $\sigma = 3.5 \times 10^7$ S/m, $\mu_r = 300$.

3.6 Inversion of data collected underwater

We have learnt how the duration of a pulse can affect the scattered field from a target with a simulated 2 m $\times$ 1 m Tx loop case. In this section, we re-examine this phenomena by assuming a marine TEMTADS 2x2 sensor system (TT22) excited by ideal step-off, rectangular pulses with $t_w = 1$ ms and $t_w = 10$ ms, respectively. Our goal is to evaluate the effectiveness of inversions using synthetic marine scattered data when a magnetic dipole model in free space is used as a model of the scattered field response.

A TT22 system shown in Fig. 18 consists of four z-directed transmitters of dimension 0.35 m $\times$ 0.35 m and four triaxial receiver cubes of 0.1 m $\times$ 0.1 m $\times$ 0.1 m. We assumed the TT22 is immersed in sea water of $d_{\text{sea}} = 20$ m and is set above the seafloor at a height of 0.2 m to interrogate a sphere buried in the sediment. The sphere has a radius of $a = 0.03$ m with $\sigma = 3.5 \times 10^7$ S/m, $\mu_r = 300$. Its center is at $(0.05, 0.05, d_{\text{sea}} + 0.30)$ m. The conductivities of the three layers are $\sigma_1 = 0$ S/m (air), $\sigma_2 = 4$ S/m (sea), $\sigma_3 = 0.4$ S/m (sediment).

With the different driving source functions, Fig. 19 (a) shows the scattered transient responses measured from all 12 receivers after firing one transmitter, e.g., Tx1. We see that the scattered responses from the pulse width of 10 ms are stronger than those from the pulse width of 1 ms, particularly for late times.

Next we consider a simple inversion test. For terrestrial UXO sensing, an equivalent induced dipole model has been used effectively to describe low frequency EMI scattering of a metal target (Das et al., 1990; Pasion and Oldenburg, 2001; Bell et al., 2001; Smith et al., 2004). In the time domain, a target is mathematically characterized by a 3×3 magnetic polarizability tensor P and has an eigen-decomposition

$$P(t) = \sum_{i=1}^{3} L_i(t) \mathbf{e}_i \mathbf{e}_i^T, \tag{36}$$

where $\mathbf{e}_i (i = 1, 2, 3)$ is the orthonormal eigenvector representing the ith principal direction of dipolar polarization with respect to a reference system and $L_i(t)$ is the principal polarization strength that is a function of the geometry and material properties of a target. The task of EMI sensing of UXO is to recover the principal polarizabilities from measurements.

To solve for the parameters in Eq. (36) the following system of equations (Song et al., 2011) are constructed

$$\mathbf{d}(t) = A(\mathbf{r}, \mathbf{r}_s)\mathbf{q}(t), \tag{37}$$

where $\mathbf{d}(t) = [d_1(t), \cdots, d_M(t)]^T$ is an $M \times 1$ measured data vector at time instant t, and $A(\mathbf{r}, \mathbf{r}_s)$ is a $M \times 6$ matrix denoting the sensitivities of the M sensors at $\mathbf{r}_s$ to the object located at $\mathbf{r}$, and $\mathbf{q}(t)$ a 6×1 column vector whose components are the elements of the polarizability tensor $P(t)$ of an object. They are given by

$$A(\mathbf{r}, \mathbf{r}_s) = \begin{bmatrix} \mathbf{a}_1^T(\mathbf{r}, \mathbf{r}_s) \\ \vdots \\ \mathbf{a}_M^T(\mathbf{r}, \mathbf{r}_s) \end{bmatrix}, \mathbf{a}_i(\mathbf{r}, \mathbf{r}_{Rx_i}, \mathbf{r}_{Tx_i}) = \begin{bmatrix} H_R^x H_T^x \\ H_R^x H_T^y + H_R^y H_T^x \\ H_R^x H_T^z + H_R^z H_T^x \\ H_R^y H_T^y \\ H_R^y H_T^z + H_R^z H_T^y \\ H_R^z H_T^z \end{bmatrix}, \mathbf{q}(t) = \begin{bmatrix} p_{11}(t) \\ p_{12}(t) \\ p_{13}(t) \\ p_{22}(t) \\ p_{23}(t) \\ p_{33}(t) \end{bmatrix}. \tag{38}$$

where $\mathbf{a}_i(\mathbf{r}, \mathbf{r}_{Rx_i}, \mathbf{r}_{Tx_i})$ is 6×1 column vector representing spatial sensitivities of the ith pair of transmitter-receiver to the object located at $\mathbf{r}$. Notice that the primary fields $\mathbf{H}_T = [H_T^x, H_T^y, H_T^z]$ and $\mathbf{H}_R = [H_R^x, H_R^y, H_R^z]$ in Eq. (38) are static and computed for a transmitter and receiver loop in free space.

We are interested to know if Eqs. (37) and (38) be directly used to invert the scattered data in the marine environment without modification. With the simulated marine TT22 in Fig. 18, we proceed to inversion tests by using the three sets of synthetic data in Fig 19 (a): the step-off and two rectangular pulses with widths of 1 ms and 10 ms. At this stage the test is simplified to a linear inverse problem by assuming a known location of the target. Fig 19 (b) shows the recovered polarizabilities for the three excitation waveforms. For each current function, the inversion derives three identical polarizabilties that cannot be discerned in the plot. This is exactly what we expected. In addition, the impact of pulse width is exhibited in the recovered polarizabilities. The longer duration of an excitation, e.g., 10 ms, produces a slower decay polarization in late times than that with 1 ms. The larger width of pulse, the better the recovered polarizabilities approach those from the step-off driving function.

The preliminary inversion test illustrate that a magnetic dipole model in free space is readily adapted to processing the off-time scattered data of a highly conducting and permeable object buried in the sea-bottom with EMI measurements collected in a conducting underwater environment.
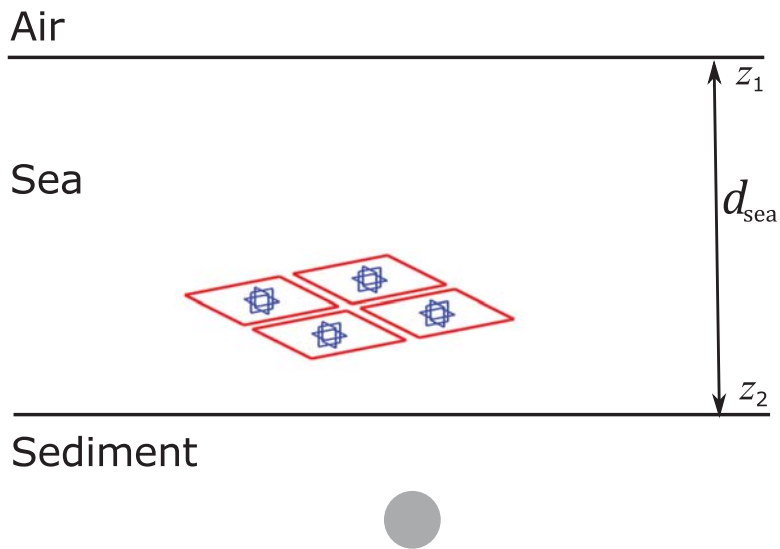
Figure 18: A simulated marine TT22 system consisting of four planar transmitter (each size of 0.35 m $\times$ 0.35 m) and four tri-axial receiving cubes (each size of 0.10 m $\times$ 0.10 m $\times$ 0.10 m). Sensor height $h = 0.2$ m. The center of the sensor is $\mathbf{r}_s = (0.0, 0.0, d_{sea} - h)$ m. The three-layer parameters: $\sigma_1 = 0$ S/m, $\sigma_2 = 4$ S/m, $\sigma_1 = 0.4$ S/m, $d_{sea} = 20$ m. The parameters of a sphere: $a = 0.03$ m, $\sigma = 3.5 \times 10^7$ S/m, $\mu_r = 300$. Its center is $\mathbf{r} = (0.05, 0.05, d_{sea} + 0.30)$ m.
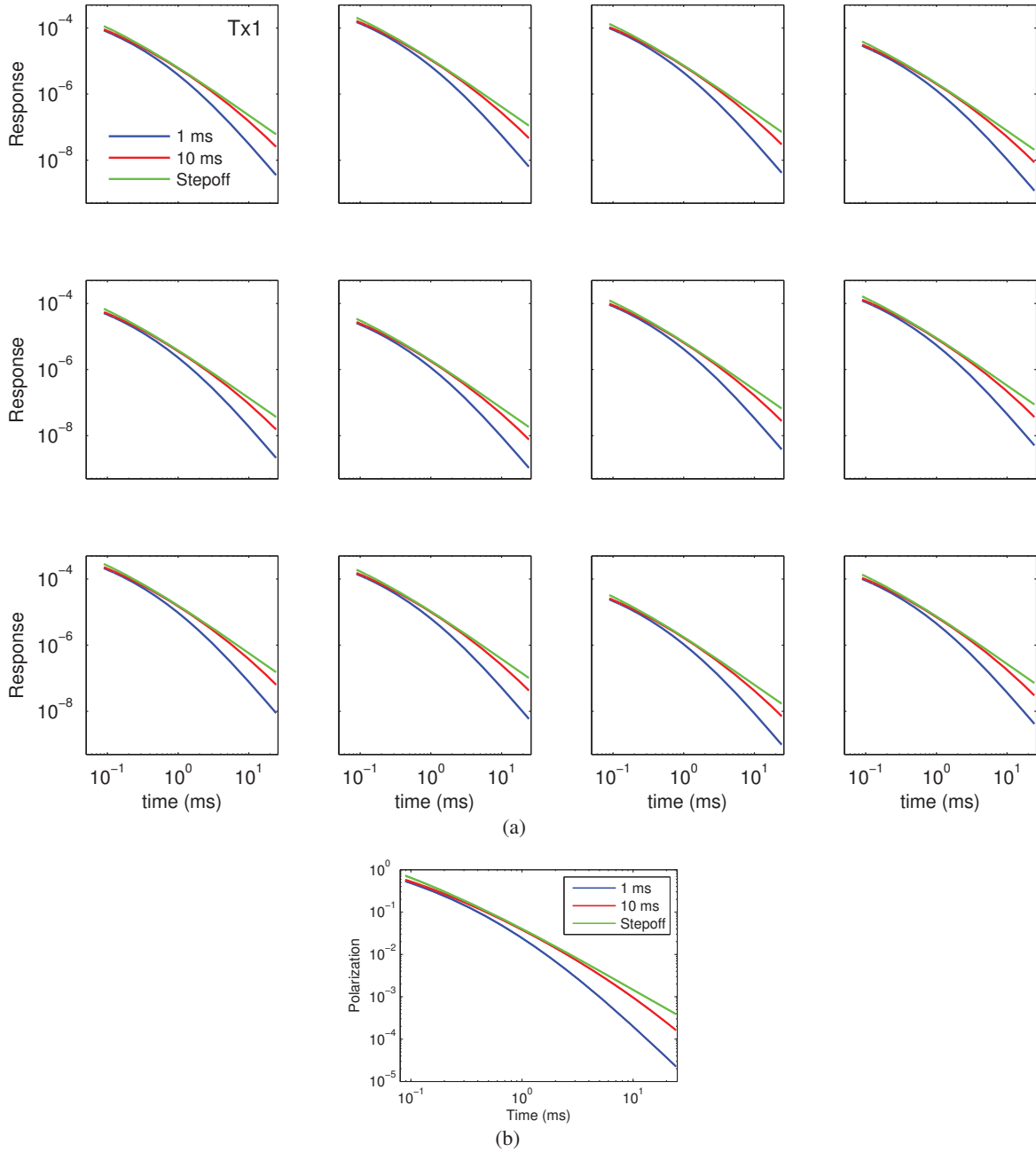
Figure 19: Given the setup in Fig. 18: (a) scattered transient responses under rectangular pulse width of 1 ms, 10 ms, and step-off excitation waveforms; (b) recovered polarizabilities.

4 Numerical investigation of an insulated VMD immersed in a uniform conducting medium

So far, our studies on the transient background and scattered responses have assumed that the dipole or loop source and receiver are contained in a uniform or layered conducting medium. In practice, these sources and receivers are waterproofed and have no direct contact with the medium under study. The fields excited by an insulated loop antenna may be different from those of a similar bare loop antenna. In this section, we investigate the problem by enclosing a VMD transmitter in a spherical cavity that is immersed in a uniform conducting medium.

Consider a magnetic dipole situated at the origin and oriented in the polar direction in a spherical co-ordinate system of (r, θ, ϕ) in Fig. 20. According to Wait (1952), the magnetic dipole in this situation will generate transverse-electric spherical waves inside and outside the spherical cavity. For the background and cavity with the electrical parameters of $(\epsilon_1, \sigma_1, \mu_1)$ and $(\epsilon_2, \sigma_2, \mu_2)$, respectively, the resulting non-zero component fields at r in the frequency domain are

$$H_{lr} = \frac{m_l}{2\pi r^3} \cos\theta (1 + \gamma_l r) \exp(-\gamma_l r)$$

$$H_{l\theta} = \frac{m_l}{4\pi r^3} \sin\theta (1 + \gamma_l r + \gamma_l^2 r^2) \exp(-\gamma_l r) \tag{39}$$

$$E_{l\phi} = -j\omega\mu_l \frac{m_l}{4\pi r^2} \sin\theta (1 + \gamma_l r) \exp(-\gamma_l r),$$

where $l = 1, 2$ and $\gamma_l = [j\omega\mu_l(\sigma_l + j\omega\epsilon_l)]^{1/2}$. For $l = 1$, Eq. (39) describes the primary fields of the magnetic dipole inside the spherical cavity with $m_1 = IdA$ with a current of I and the differential

(a)
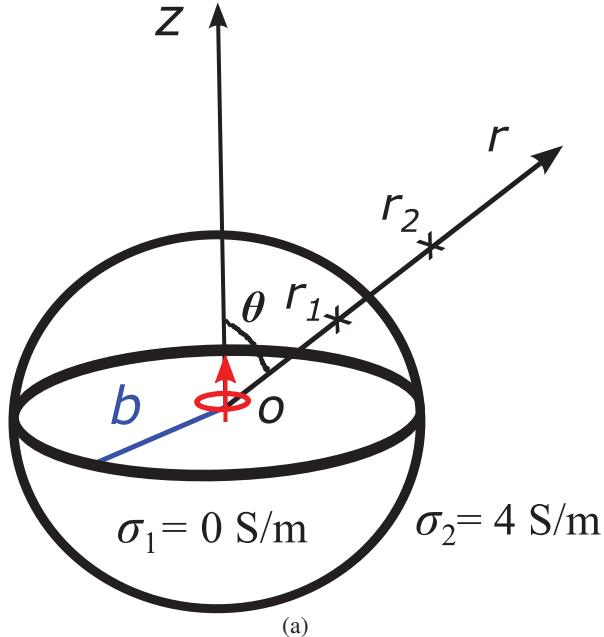
Figure 20: Schematic setup for a VMD insulated by a spherical cavity that is immersed in an uniform conducting medium. The radius of the cavity is b. The radial distances of $r_1 < b$ and $r_2 > b$ at a polar angle of θ denote the observations inside and outside the cavity.

area dA. For $l = 2$, Eq. (39) describes the fields in the region exterior to the cavity with an equivalent dipole moment m_2 contained within the spherical cavity. The ratio between m_2 to m_1 is given by

$$\frac{m_2}{m_1} = \frac{\gamma_1 B}{\gamma_2 C}.$$ (40)

The secondary fields inside the cavity due to the insulation boundary are given by

$$H_{1r,s} = \frac{A}{j\omega\mu_1} \cos\theta [i_1''(\gamma_1 r) - i_1(\gamma_1 r)]\gamma_1^2$$

$$H_{1\theta,s} = -\frac{\gamma_1 A}{j\omega\mu_1}\frac{1}{r} \sin\theta i_1'(\gamma_1 r)$$ (41)

$$E_{1\phi,s} = -\frac{A}{r} \sin\theta i_1(\gamma_1 r),$$

where i_1 is a spherical Bessel function of order one of the first type, defined as $i_1(z) = \cosh z - \sinh z / z$. The primed quantities indicate a differentiation with respect to the argument of the function. The coefficients A and B in above equations are determined by imposing the continuities of the tangential electric and magnetic fields E_ϕ and H_θ across the boundary at $r = b$:

$$B = C\frac{\gamma_1[\kappa_1(\gamma_1 b)i'(\gamma_1 b) - \kappa_1'(\gamma_1 b)i_1(\gamma_1 b)]}{\gamma_1\kappa_1(\gamma_2 b)i'(\gamma_1 b) - \gamma_2\kappa_1'(\gamma_2 b)i_1(\gamma_1 b)}$$

$$A = \frac{B\kappa_1(\gamma_2 b) - C\kappa_1(\gamma_1 b)}{i_1(\gamma_1 b)}$$ (42)

$$C = j\omega\mu_1 m_1\gamma_1 / 4\pi,$$

where $\kappa_1(z) = (1 + z)\exp(-z)/z$ is the spherical Bessel function of order one of the third type.

For a spherical cavity with a radius of $b = 20$ cm immersed in a uniform conducting medium of 4 S/m, Fig. 21 shows the VMD-generated fields at $r = b$ and $\theta = 45^0$ satisfying the boundary conditions: $E_{1\phi,s} + E_{1\phi} = E_{2\phi}$ and $H_{1\theta,s} + H_{1\theta} = H_{2\theta}$ in frequency domain, which involve Eqs. (39), (41), and (42).

To investigate the effect of the cavity we compute the ratio of m_2/m_1 using Eq. (40) across a wide frequency range (Fig. 22). For a 20 cm cavity (Fig. 22a) the real part of the ratio at $b = 20$ cm has the constant value of 1 across a wide range of frequencies and the imaginary part is less than 1, linearly increasing with logarithmic frequencies. The ratio starts to oscillate at high frequencies > 10 MHz. When decreasing the size of the cavity to $b = 10$ cm and $b = 5$ cm, the oscillation in the ratio moves toward higher frequencies after 100 MHz and the amplitude becomes smaller. At sufficiently low frequencies, the equivalent dipole moment m_2 for an insulated VMD approaches m_1 for an uninsulated VMD. We conclude that the cavity has little effect on observed fields in the exterior region.

We now turn our attention to the fields inside the cavity. Referring to Fig. 20, for $b = 0.2$ m and $\theta = 45^0$ we compute the transient fields inside the cavity at $r_1 = 0.1$ m and the fields outside the cavity at $r_2 = 1$ m, $r_2 = 5$ m and $r_2 = 10$ m. Fig. 23 presents vertical magnetic fields inside and outside of the cavity. The fields outside with and without the cavity are the same, consistent with our analysis in the frequency domain. For the fields inside, we plot the primary and scattered field separately for better visualization of their behavior. The results shows that the primary field inside is far weaker than
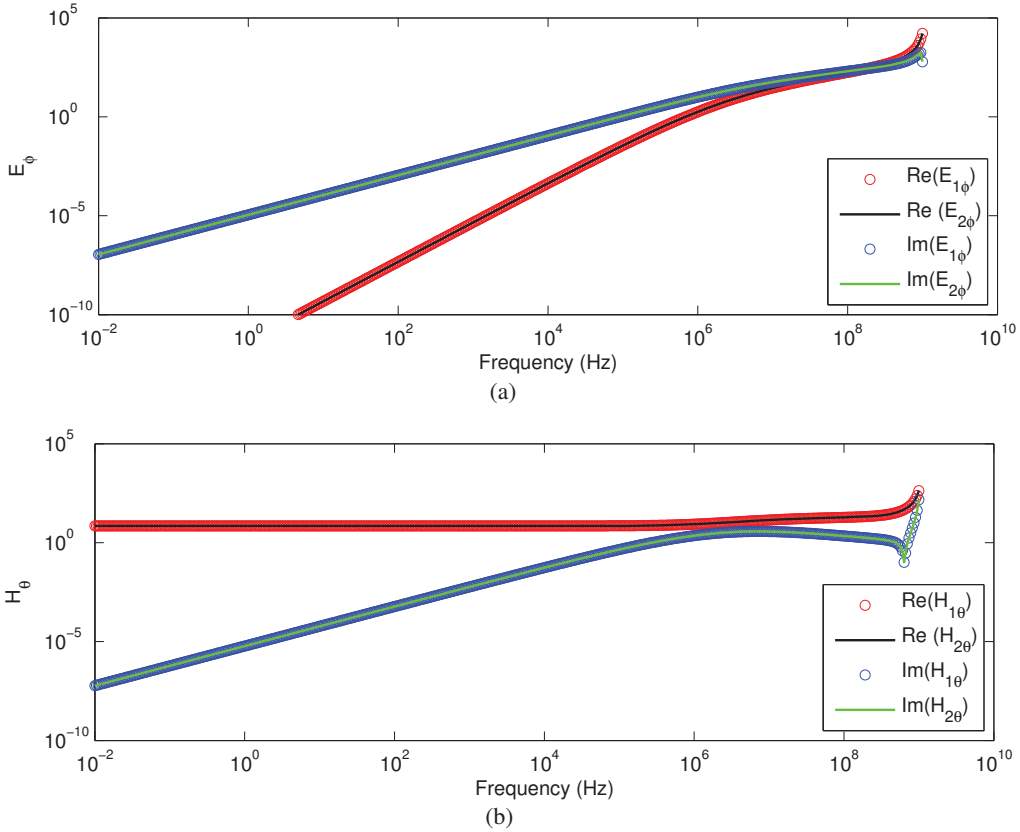
Figure 21: A check of boundary conditions of an insulated VMD in frequency-domain for $\theta = 45^0$ and $b = 0.2$ m. (a)E_ϕ. (b)H_θ.

the scattered field inside. Surprisingly, the scattered field inside at $r_1 = 0.1$ m (thick curve) almost overlaps with the field outside at $r_2 = 1$ m roughly beginning with 0.01 ms. Increasing r_2 to 5 m and 10 m, we see that it takes longer for the fields inside and outside to overlap with convergence occurring somewhere between 0.5 ms and 1 ms. This correspondence of background fields across widely offset observation distances is similar to what we have observed in previous sections when numerically and analytically studying the offset effects of bare loops or VMD in layered or uniform conducting media. The cavity insulation appears to have little effect on the vertical fields both inside and outside the cavity.
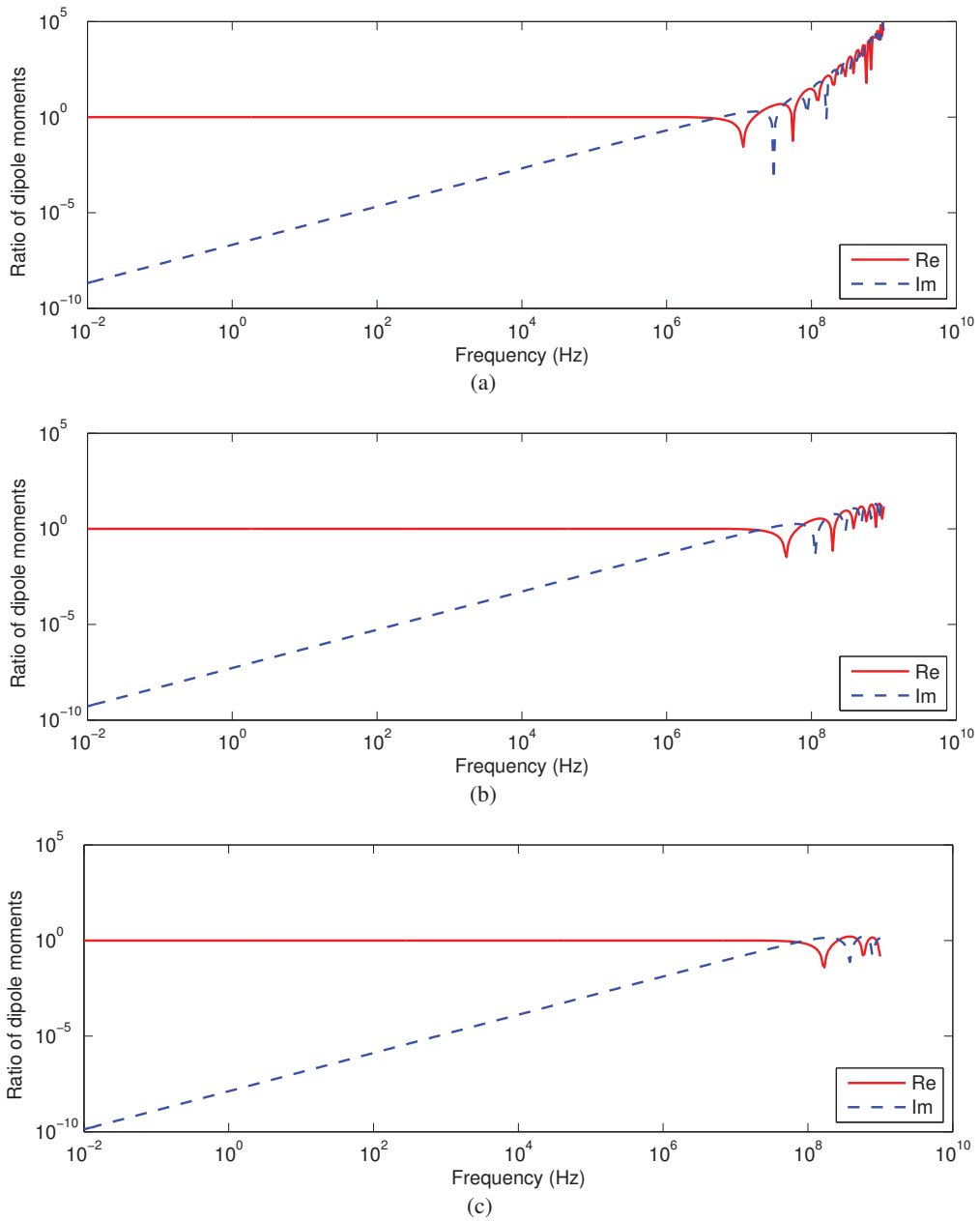
Figure 22: Ratio of dipole moments m_2/m_1 for an insulated VMD. The radius b of a spherical cavity: (a) 20 cm; (b) 10 cm; (c) 5 cm.
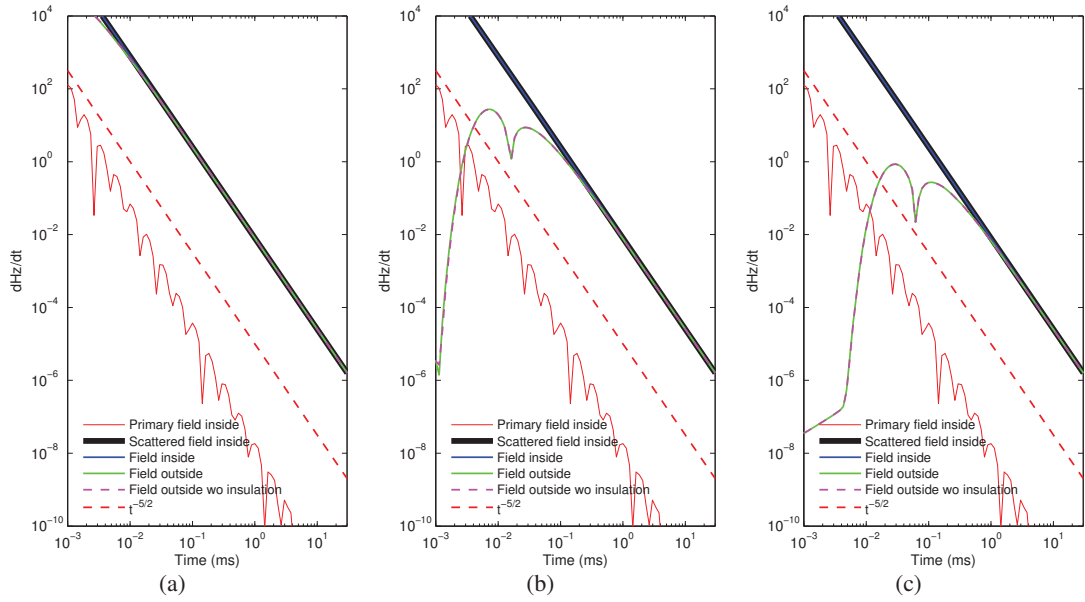
Figure 23: dH_z/dt responses inside and outside a spherical cavity defined in Fig. 20. With $b = 0.2$ m, $\theta = 45^0$, and $r_1 = 0.1$ m, $r_2 =$ (a) 1 m; (b) 5 m. (c) 10 m. Field inside = Primary field inside + Scattered field inside.

5 Underwater measurements

The original intent of this project was to utilize data collected by marine sensors under development as part of other funded SERDP/ESTCP projects. However, those projects have been delayed and suitable data was not available. Through Black Tusks interactions with Gap Explosive Ordnance Detection (GapEOD) in Brisbane, Australia, an opportunity arose to collect some marine data with an EM system.

For the marine measurements, GapEOD built a 2 m x 1 m x 1 m fiberglass frame and encased two receiver cubes in epoxy to make them waterproof (Fig. 24.) The transmitter loop comprised 12 turns of wire arranged in a 2 m by 1 m rectangle at approximately the same vertical level as the base of the receiver cubes. A 24V power-supply was used to provide a maximum current of 11.4 A (at 23.4 V) to a Gap LPTX-25 transmitter that operated at a 25 Hz base-frequency with a 50% duty cycle waveform. Four separate measurements campaigns were conducted either within Moreton Bay, close to Brisbane or the Gold-Coast Seaway near Surfers Paradise:

1) Measurements over a range of ordnance items between water depths of 2.5 and 14 m conducted over two days (13 and 16 March 2015);

2) Terrestrial and marine measurements conducted over a 105 mm projectile at exactly the same locations relative to the sensor frame (July 2015).

3) More controlled measurements over a 105 mm projectile in shallow water (April 2016);

4) Terrestrial and marine coil and B-field full-waveform measurements to better understand the underwater noise environment and primary field distortions caused by the conductive sea-water (June 2016).

5.1 Measurement campaign 1: Background and proof of concept

For the first measurement campaign we chartered a small vessel (Fig. 25) and collected background data at various different water depths (Fig. 26) within Moreton Bay. Water samples taken during the

Figure 24: Frame built for the underwater tests, comprising two receive cubes and a 2 m x 1 m transmitter coil.

UltraTEM measurements revealed that the sea-water had a conductivity of 6 S/m. For the measurements the two receivers were placed 80 cm apart and equally offset by 40 cm from the transmitter loop center. The background signal in the horizontal components is quite weak: this is because at times greater than 100 μs, the background behaves as if it were generated by a propagating *smoke-ring* (Nabighian, 1979) whose dimensions are several times larger than the size of the transmitter. The field near the center of that smoke ring is predominantly vertical. The observations show that the vertical component field decays relatively rapidly with time: at a rate of between $t^{-5/2}$ and t^{-3}. The amplitude of the decay increases with water-depth but converges to a steady state value equivalent to an infinite half-space. These decay rates agree with theoretical predictions and modeling results developed within this project that account for sea-water interface effects (section 3.1). The interface effects account for the slightly faster decay rate of the measurements collected in shallower water.

We also collected data with ordnance items placed inside the PVC tube with the sensor frame positioned on the sea-bottom. For those measurements we first collected a background measurement, then raised the frame to the surface and inserted the ordnance item or surrogate into the PVC tube, before the frame was lowered over approximately the same location. Measurements were then taken with the frame stationary for at least a minute per sample location. Photos of some of the items measured during Measurement Campaign 1 are shown in Fig. 27 with the resulting receiver data shown in Fig. 28 . All these measurements were collected when the ordnance item or surrogate was at either end of the PVC tube (Pos. 1 directly under the transmitter wire, or Pos 2. 1 m outside the transmitter frame). In each case, we plot the data from the closest receiver which is still always at least 1 m away from the object being measured. At early times the metal and background signals are comparable, but the sea-water response dies down much faster than the response from the metallic items. Hence, good strong signals from the metallic items are evident at later times. These results demonstrate that detection of metallic ordnance in sea-water is possible using a large transmitter loop and three-component receiver cubes.

(a)

(b)
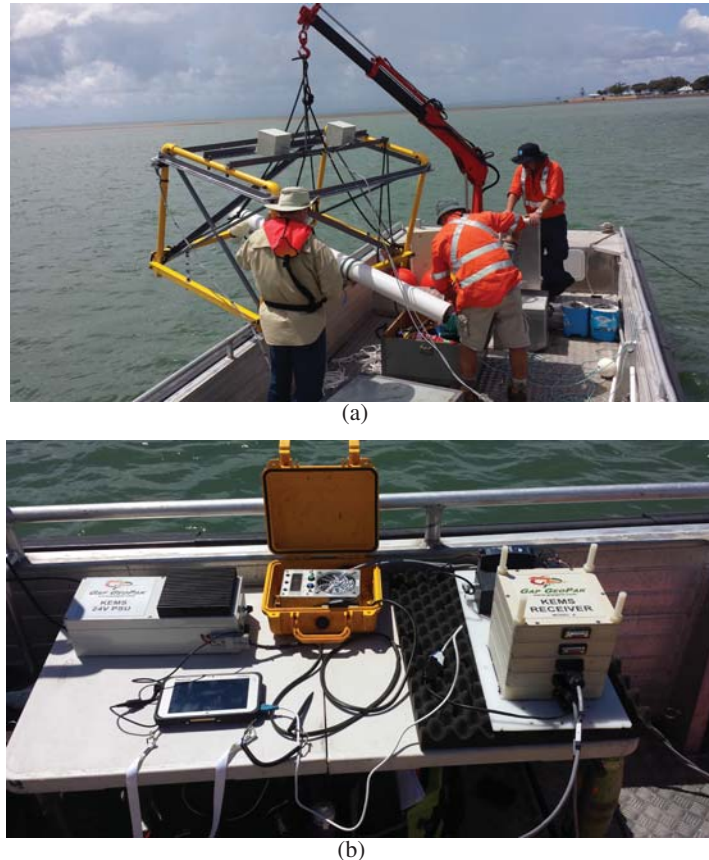
Figure 25: Underwater tests were conducted in Moreton Bay near Brisbane. (a): System being moved over the side of the vessel prior to lowering into the water; (b) Components of the EM system including power-supply, LPTX-25 transmitter, Toughpad for display of data and UltraTEM receiver system.
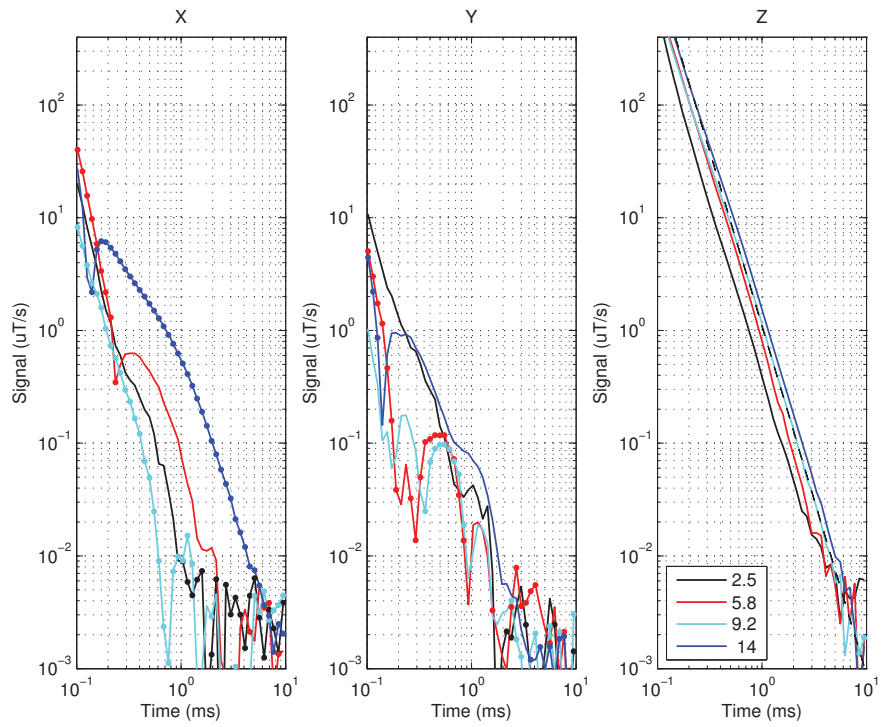
Figure 26: Background signals at different water depths as measured by the UltraTEM system (left X-component, center Y-component and right Z-component).

Figure 27: Items measured during phase 1, including 81 mm mortar (top left), ferrous cylinder (top right) and 105 mm projectile (bottom left). An image of the sample tube with a 105 mm projectile present is at the bottom right.
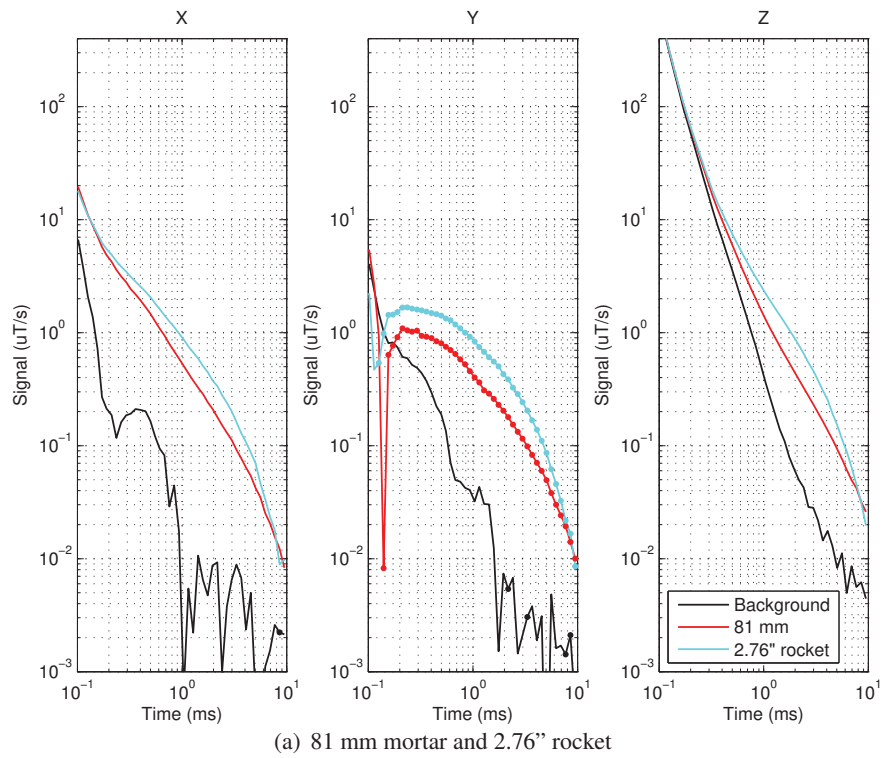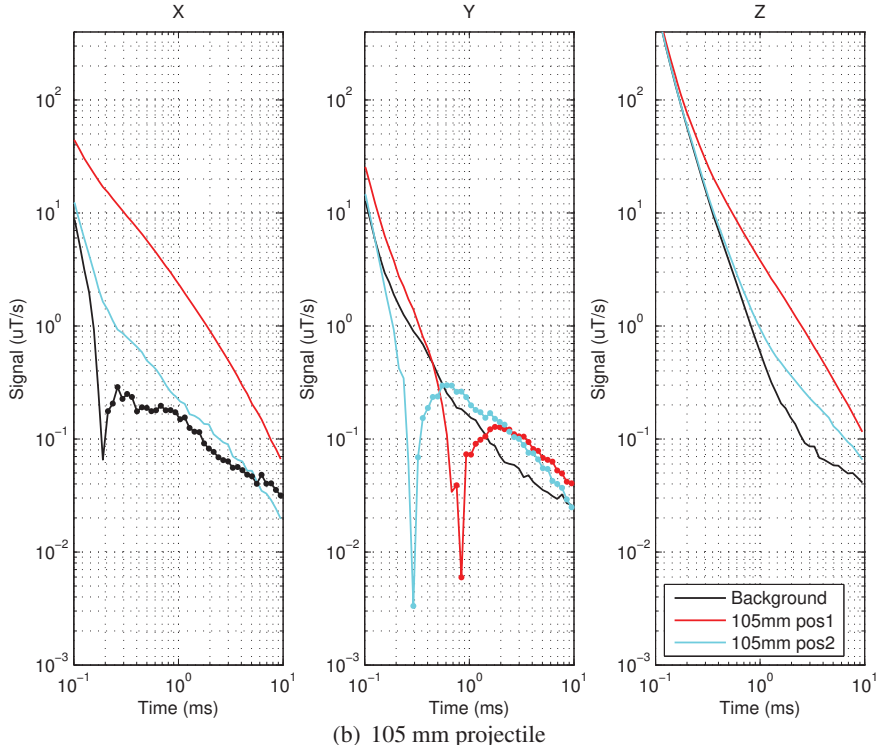
Figure 28: Underwater measurements over several test items at Pos 1 (under the edge of transmitter coil) for (a) and first measurement in (b) with second measurement at Pos 2 (1 m from edge of the transmitter coil and outside the loop).

5.2 Measurement campaign 2: Comparison of terrestrial and marine measurements

During measurement campaign 2 we collected data with exactly the same transmitter/receiver/object geometry in both the terrestrial and marine environments (Fig. 29). All measurements were collected over a 105 mm projectile. At later times (beyond 0.5 to 1 ms) the terrestrial and marine results are virtually identical (Figs. 30 & 31). This means that from a modeling perspective, these later time data can be treated the same in both the terrestrial and marine environments, which agrees with the conclusions from our modelling study and previous SERDP sponsored research. The measurements with the 105 mm in the marine environment undershoot the background measurements at early time (Fig. 31(a)), meaning that background subtraction reveals negative transients from the projectiles (Fig. 31(a)). This interaction phenomenon has been observed previously (e.g. Shubitidze, 2011) and increases with increasing offset between the object and receiver. However, the interaction effects evident in these measurements are much later in time than have been observed previously. We suspect these are due to incorrect background measurement caused, in part, by the requirement to lift and then reposition the frame between measurements.
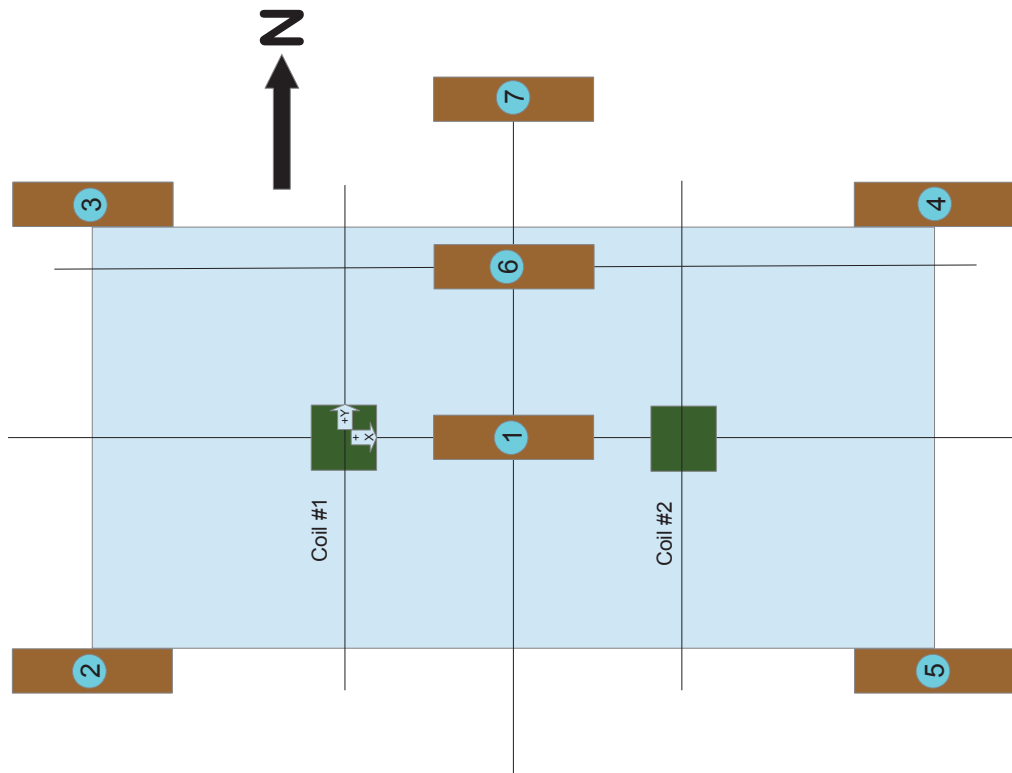
Figure 29: Layout of the frame used for the second measurement campaign showing the locations of measurements collected over a 105 mm projectile in both the terrestrial and marine environments.
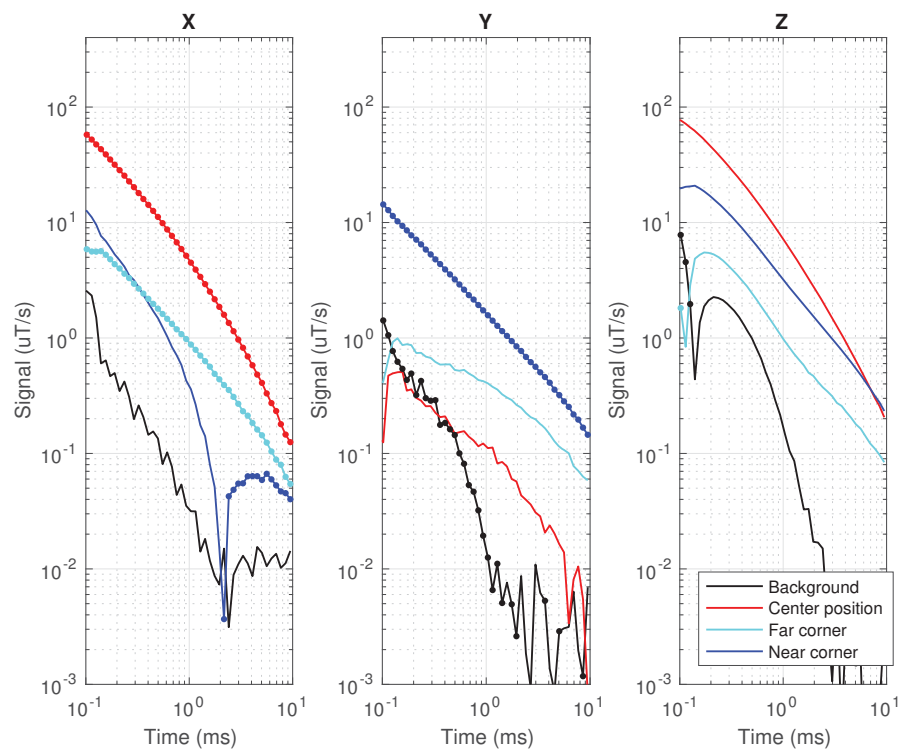
Figure 30: Terrestrial measurements of a 105 mm projectile at three different positions under the sensing frame.
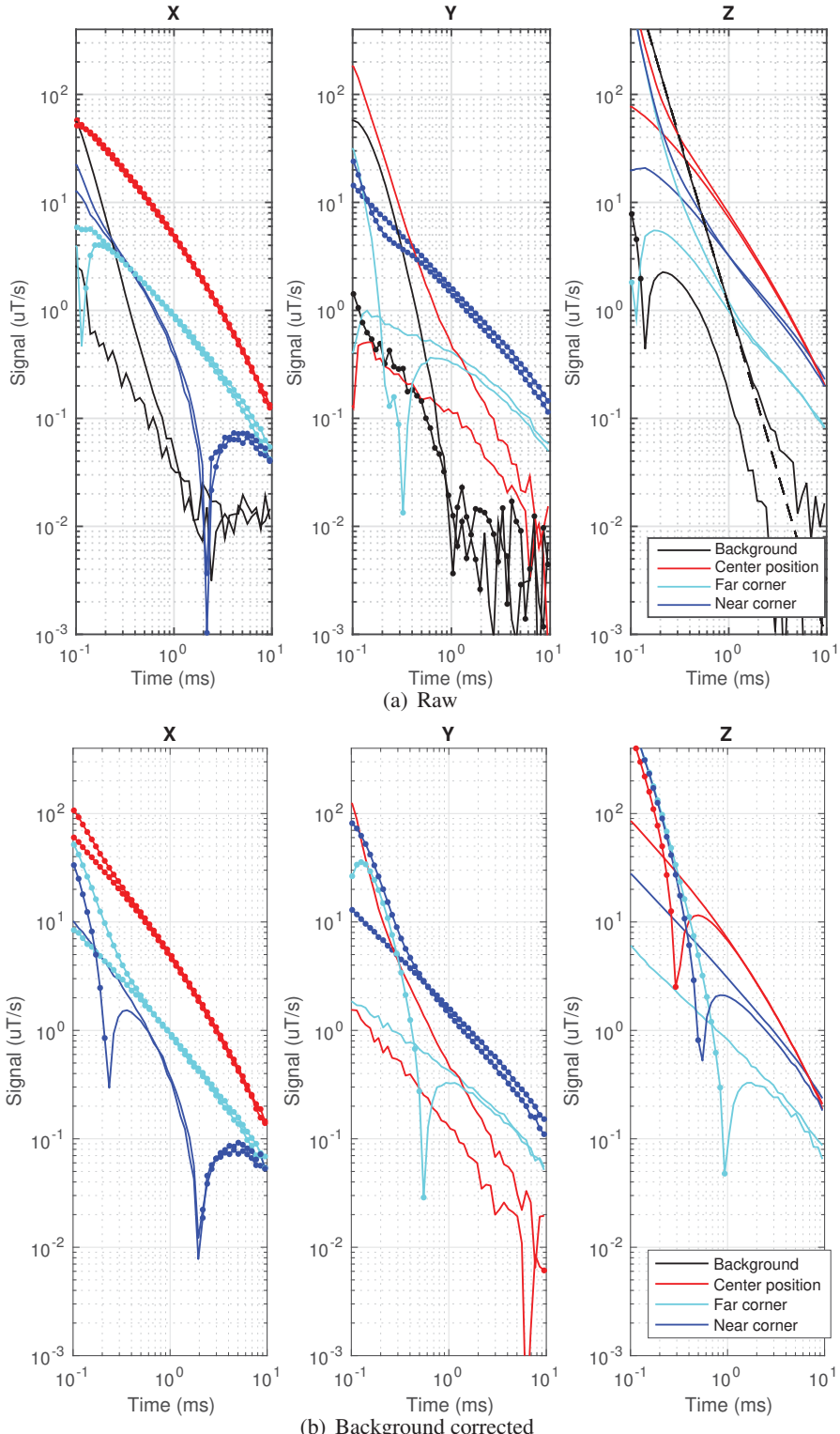
Figure 31: Marine and terrestrial measurements are virtually identical from about 0.5 to 1 ms and later in time, with the seawater effects predominantly occurring at early time. We suspect that the undershoots that occur at early time are due to poor background removal and are not indicative of the true response from the object.

5.3 Measurement campaign 3: Early time effects

In the third measurement campaign we focused on understanding the early-time effects that were apparent in the second measurement campaign but which we suspected were due to poor background removal. The transmitter and receiver set-up was the same as the previous two campaigns but this time we installed the receiver cubes and transmitter loop onto a smaller, more portable fiberglass frame (Fig. 32). In addition, rather than retrieving the frame between measurements, we kept the frame in a fixed location and used a diver to move the ordnance item (a 105 mm projectile) to the different measurements positions shown in Fig. 33. Between each measurement on the 105 mm projectile we collected a background measurement so were better able to remove backgrounds than we were in the second campaign. One receiver cube was placed in the center of the transmitter, and the second was placed outside the transmitter footprint, 2.0 m from the center of the system on the left side of the system. The ordnance item was moved between three different lateral position, 0.505 m right of the center, 0.495 m left of the center and then 1.5 m left of the center (0.5 m from the second receiver cube). Measurements were conducted in 3.3 to 4 m water-depth (the tidal variation during the measurement period) with the frame on the sea-bottom and then with the frame raised 50 cm above the sea-bottom, but the ordnance item kept on the sea-bottom. Water salinity was again quite high with a measured conductivity reading of $6.16\ \mathrm{S/m}$ (similar to the values observed in Moreton Bay in the previous measurement campaigns).

The response from cube 1 for the 105 mm projectile in position 2 when the system is elevated 50 cm above the sea-floor, shows almost identical responses in X- and Z-component data for the 105 mm projectile insulated (inside a thick plastic bag) and not-insulated[3] (Fig. 34). The Y-component data are different but we suspect that is due to slight orientation differences between the insulated and non-insulated samples. The background corrected responses are indistinguishable from what they would be for the equivalent terrestrial measurement. Any early time effects of the sea-water (like CCR) would be more pronounced for larger receiver to object offsets. Fig. 35 and 36 show the responses of cubes 1 position 1 and cube 2 position 3 for the insulated and non-insulated 105 mm projectiles. These measurement scenarios correspond to increased receiver to object offset, in one case with the

---

[3]The projectile has a layer of paint so is already partly insulated

Figure 32: Test frame used for the third measurement campaign. A diver placed the 105 mm projectile at each of the test locations and background measurements were collected before and after each measurement.
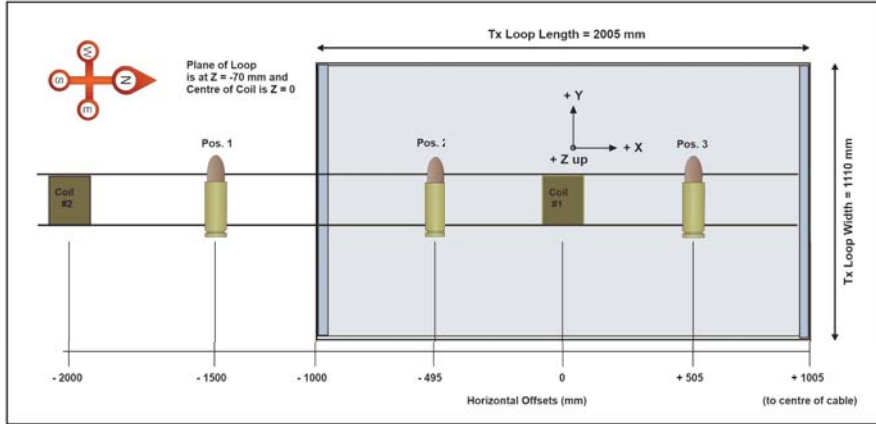
Figure 33: Plan view of the system and source locations for the third measurement campaign.

object outside the transmitter and receiver inside and the other with the reverse. Insulated and non-insulated responses are again virtually identical to each other and to the equivalent terrestrial response with small deviations at early time. These deviations are likely due to imperfect background removal (the background is more than 2 decades larger than the UXO response at early time).

Based on the measurements obtained in measurement campaign 3 we conclude that background corrected terrestrial and marine measurements are indistinguishable at times less than 200 microseconds (and probably even earlier), and the 105 mm projectile with paint covering does not exhibit any significant CCR.

As part of the third measurement campaign we also collected several minutes of data with the transmitter on and the frame on the beach and again when it was underwater. Fig. 37 compares the sensor noise of the underwater and terrestrial measurements. The noise levels are comparable with a very slight increase in early time noise for the Z-component receiver data when the system was underwater.
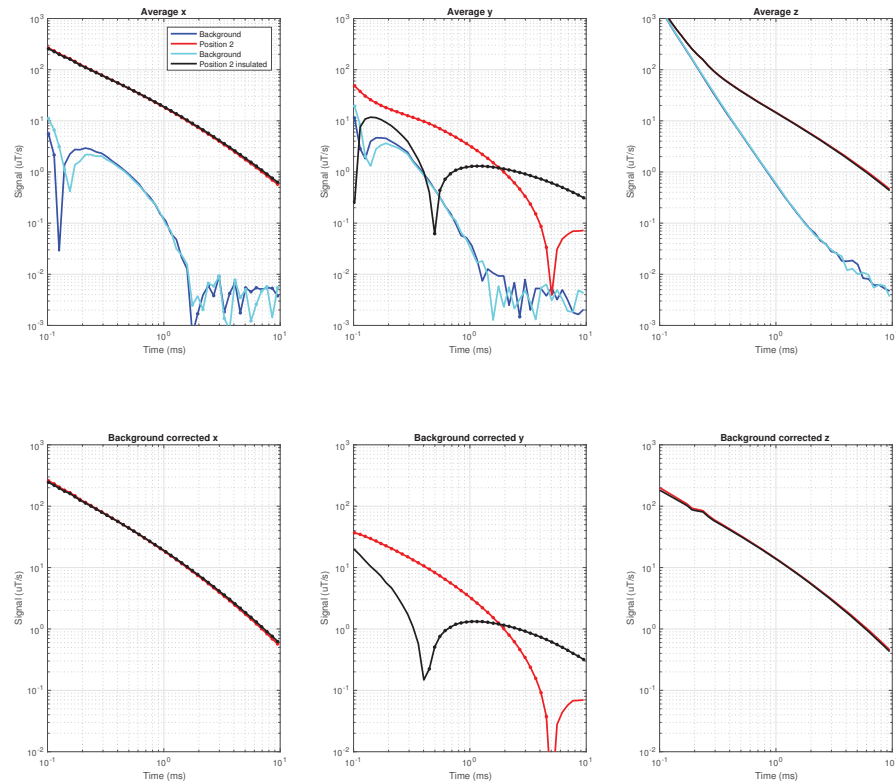
Figure 34: Comparison of insulated and non-insulated response for position 2, cube number 1 (cube and object close together) with the system elevated above sea-floor. Top plots are raw data and bottom plots are after background correction. The mismatch in Y-components is probably due to orientation differences between the two sets of measurements.
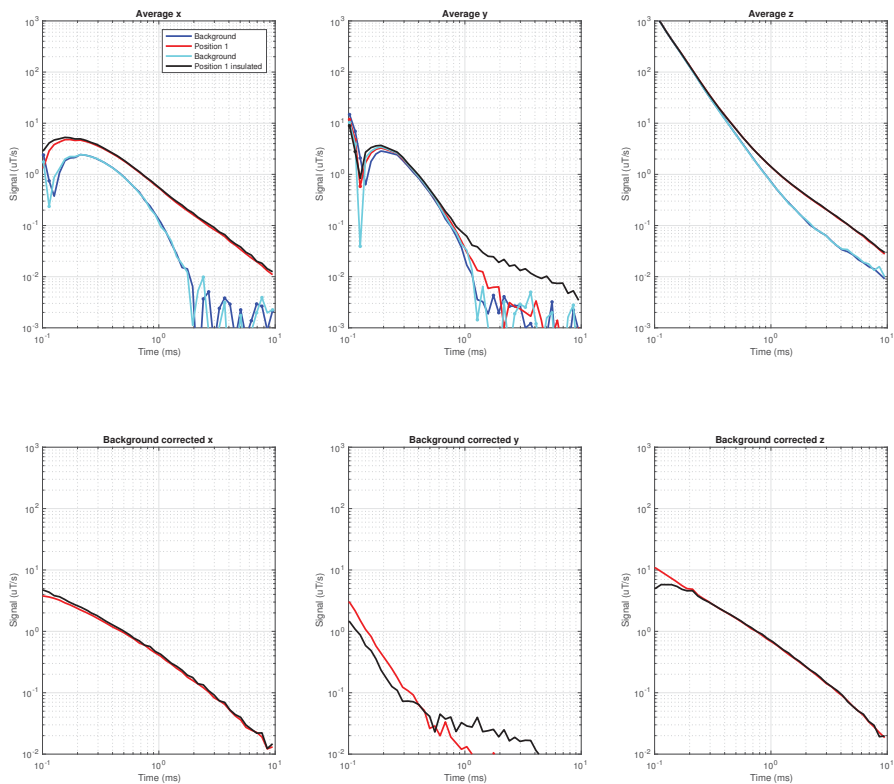
Figure 35: Comparison of insulated and non-insulated response for position 1, cube number 1 (cube and object medium distance apart) with the system on the sea-bottom. Top plots are raw data and bottom plots are after background correction.
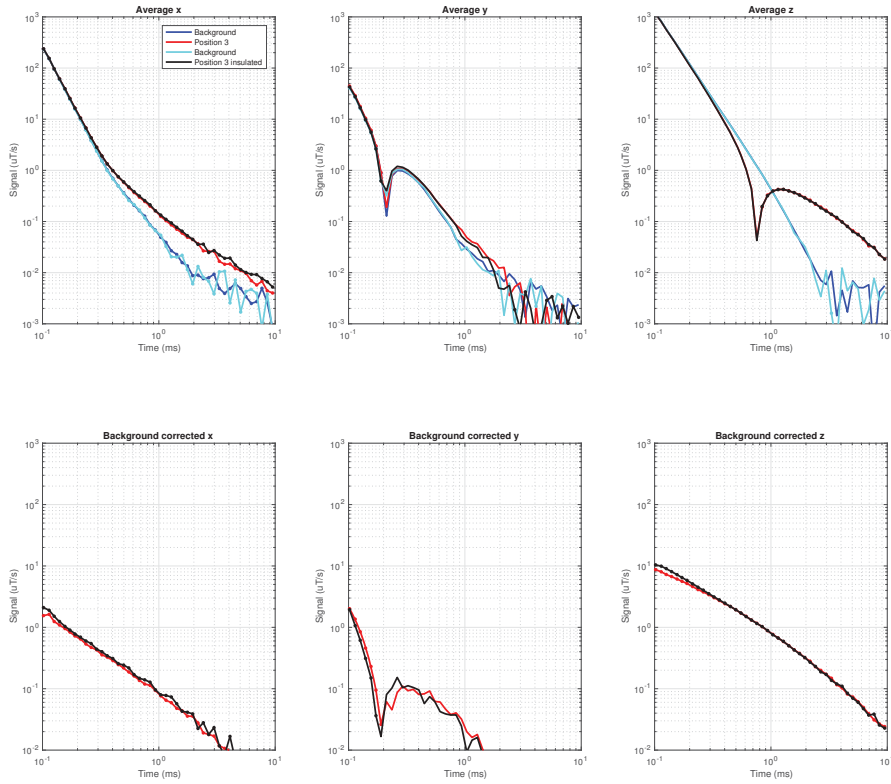
Figure 36: Comparison of insulated and non-insulated response for position 3, cube number 2 (cube and object far apart)with the system on the sea-bottom. Top plots are raw data and bottom plots are after background correction.
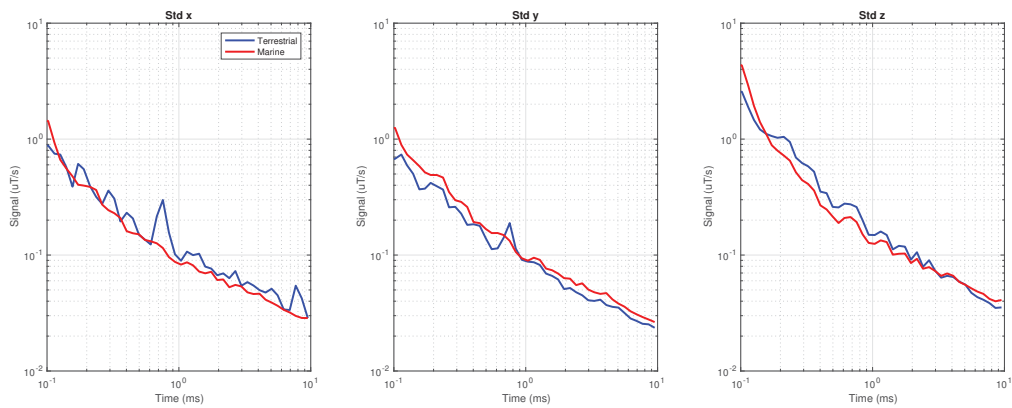
Figure 37: Comparison of sensor noise with the system in air on the beach and underwater: from left to right are the X, Y and then Z-component data.

5.4 Measurement campaign 4: Noise and primary field distortion

For the forth measurement campaign we returned to the same beach-side environment of the third campaign. Our objectives with these measurements were to (1) better understand the noise spectra in the underwater environment; and (2) verify the primary field dispersion calculations derived in Sec. 3.5. We used the same transmitter set-up as previous campaigns but augmented our coil measurements with flux-gate magnetometer measurements. Both the coil and flux-gate data were recorded with an Electromagnetic Imaging Technology (EMIT) SMARTem24 receiver: for the coil the sample rate was 120 kHz while for the flux-gate the sample rate was 24 kHz. We used a Bartington MAG-03MSSL70 flux-gate for the measurements and a nulling control box (to null the Earth's magnetic field) built by EMIT. A series of measurements were collected on land and in water at increasing lateral offset distances from the transmitter loop.

5.4.1 Noise and primary field oscillations

One motivation for collecting the noise spectra were some results reported in Bell et al. (2016) where a significant increase in noise was reported when a thinly insulated transmitter loop was immersed in salt-water. In simple terms the transmitter can be modelled as a parallel RLC circuit (Fig. 38) with damping factor

$$\zeta = \frac{1}{2R}\sqrt{\frac{L}{C}} \tag{43}$$

with L the inductance, C the capacitance and R the resistance. When $\zeta > 1$ the response of the transmitter is overdamped and the field decays exponentially on transmitter shut-off. The resistor value for the transmitter is typically chosen so that the system is either critically damped ($\zeta = 1$) or overdamped ($\zeta > 1$). The wire used for our transmitter loop comprised 12 turns of 1 mm^2 wire with a measured inductance of 630 μH and in-air capacitance of 200 pF. For critical damping, a damping resistance of approximately 890 Ω is required.
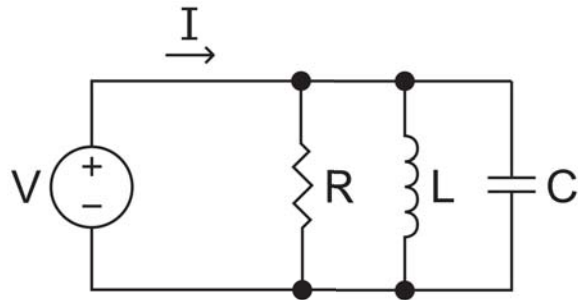
Figure 38: Parallel RLC Circuit.

The sea-water increases the capacitance of the loop through increased turn-to-core capacitance (stray capacitance between the transmitter wires and the core material). When a poorly insulated transmitter wire that is critically damped is immersed in sea-water the increase in C causes ζ to decrease to less than one and the system becomes under-damped. When the transmitter turns off it oscillates at the natural resonance frequency of an RLC circuit of

$$\omega = \sqrt{\frac{1}{LC}} \tag{44}$$

Based on the inductance and capacitance values measured in air, the resonant frequency of our transmitter loop is approximately 450 kHz. These oscillations can be avoided either by insulating the transmitter loop (as found by Bell et al., 2016) or by increasing the damping resistor in the system. To test this latter assertion, we collected measurements with a coil on land and in-water using our thinly insulated transmitter loop with and without a damping resistor. [4] For each case studied we collected a minute of data with the receiver coil in the center of the 2 m x 1 m transmitter loop. Fig. 39 shows the first 200 µs after transmitter turn-off (at 10 ms). For both the on land and in-water measurements with no-damping resistor, oscillations are evident and of increased magnitude in sea-water (ζ decreases with increasing C). Unfortunately, the band-width of the system was insufficient to accurately resolve the resonance frequency (the oscillations are under-sampled but clearly present). When the damping resistor is reintroduced into the system, the oscillations disappear for both the on-land and in-water measurements and all that remains is the self-response from the transmitter and/or receiver coil. On-land and in-water responses are almost identical.

With the damping resistor in the system, we collected additional coil measurements at increasing lateral offsets from the transmitter coil center (Fig. 40). The horizontal component response increases as the coil is moved towards the edge of the transmitter wire, then flips sign (as does the vertical component response) once measurements are collected outside the coil. The off-time responses (at least on the linear scale and limited time-range shown) for the on-land and in-water measurements are

---

[4]The case of no damping resistor is equivalent to $R \to \infty$ and $\zeta \to 0$ and hence underdamped.
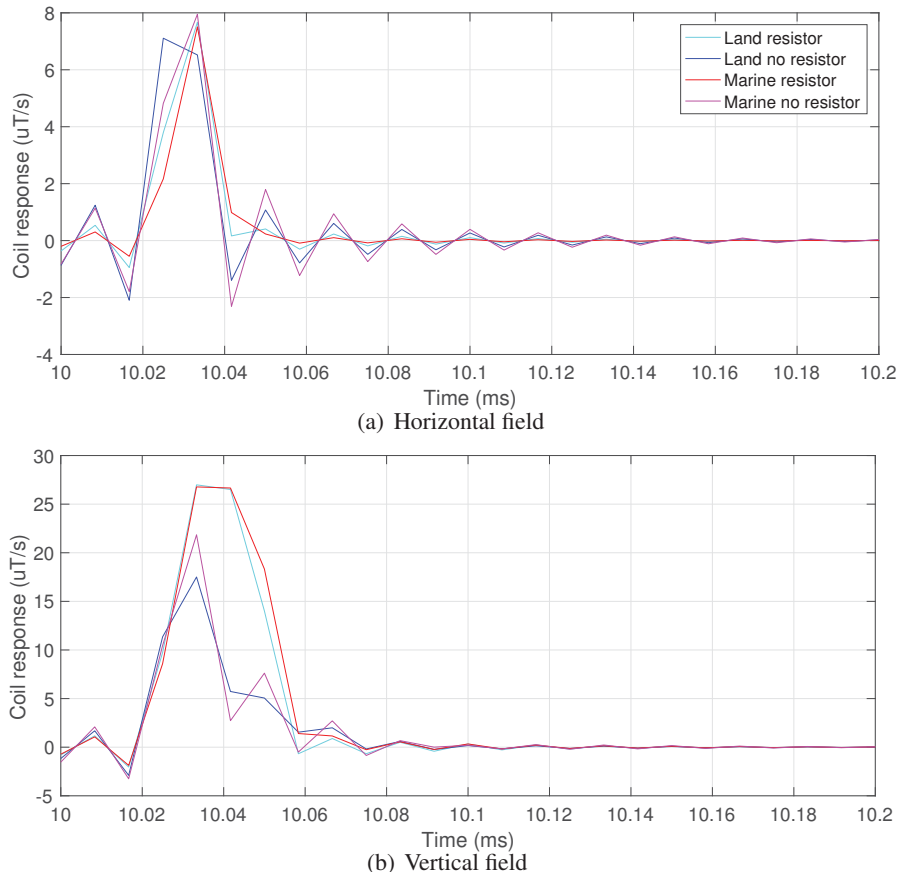
Figure 39: Off-time coil response in the horizontal (a) and vertical (b) directions for a transmitter loop with and without a damping resistor on-land and in sea-water.

almost identical for all offset locations.

(a) Horizontal field

(b) Vertical field
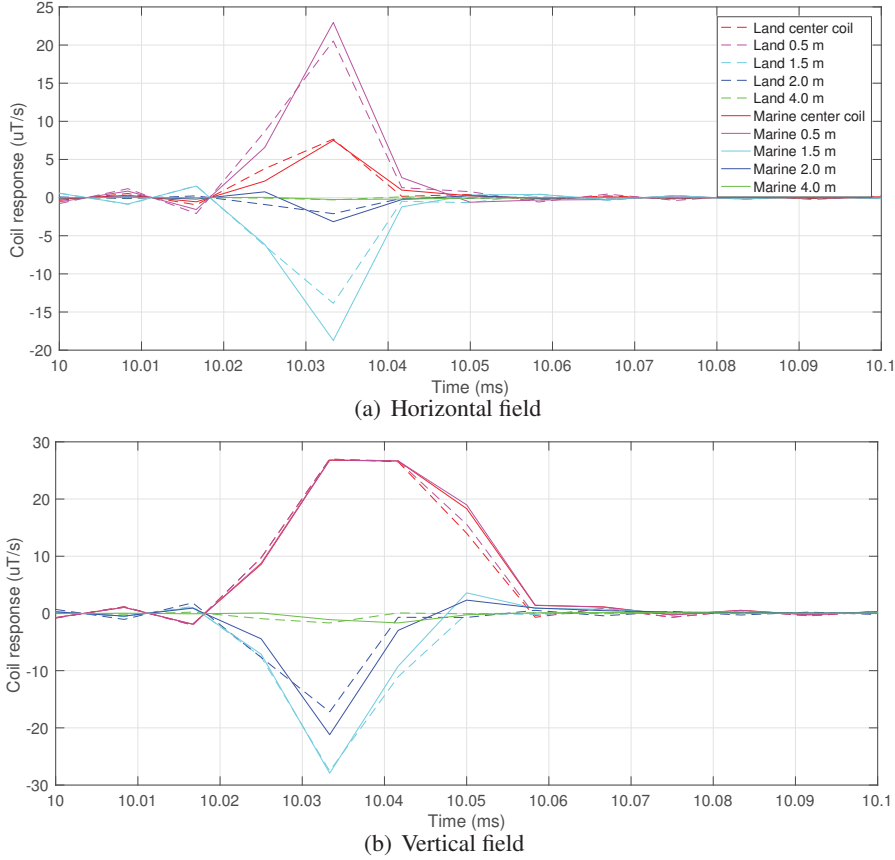
Figure 40: Off-time coil response at different horizontal offsets on land and in sea-water in the horizontal (a) and vertical (b) directions for a transmitter loop with damping resistors.

We also computed estimates of the power-spectral density (PSD) for the loop with and without a damping resistor present, for the system on land and in-water, as well as without the transmitter present (Fig. 41). With the transmitter off, the marine environment is lower noise than the adjacent terrestrial environment. The 50 Hz power-line noise and its harmonics are clearly evident but so also are a number of other lower frequency noise sources (of around 15 Hz and harmonics). For the vertical field, the PSD as a function of frequency is almost identical for on-land, in-water, damping resistor present or absent. However, for the horizontal component there is a marked increase in spectral energy in both the on-land and in-water measurements with no-damping resistor, consistent with the results reported in Bell et al. (2016).

Finally, we computed the PSD for the same lateral offset positions of Fig. 40. For both the horizontal and vertical-field the on-land and in-water PSD responses at each offset are almost identical. From these results we can conclude that there are no significant differences between on-land and in-water sensing from the perspective of the frequency content of the noise and signal (for the low-frequency range considered here).

5.4.2 Primary field dispersion

In Sec. 3.5 we considered the dispersion of the primary field waveform in the conductive seawater environment. Our modelling of an ideal step-off waveform in Fig. 14 showed a significant dispersion
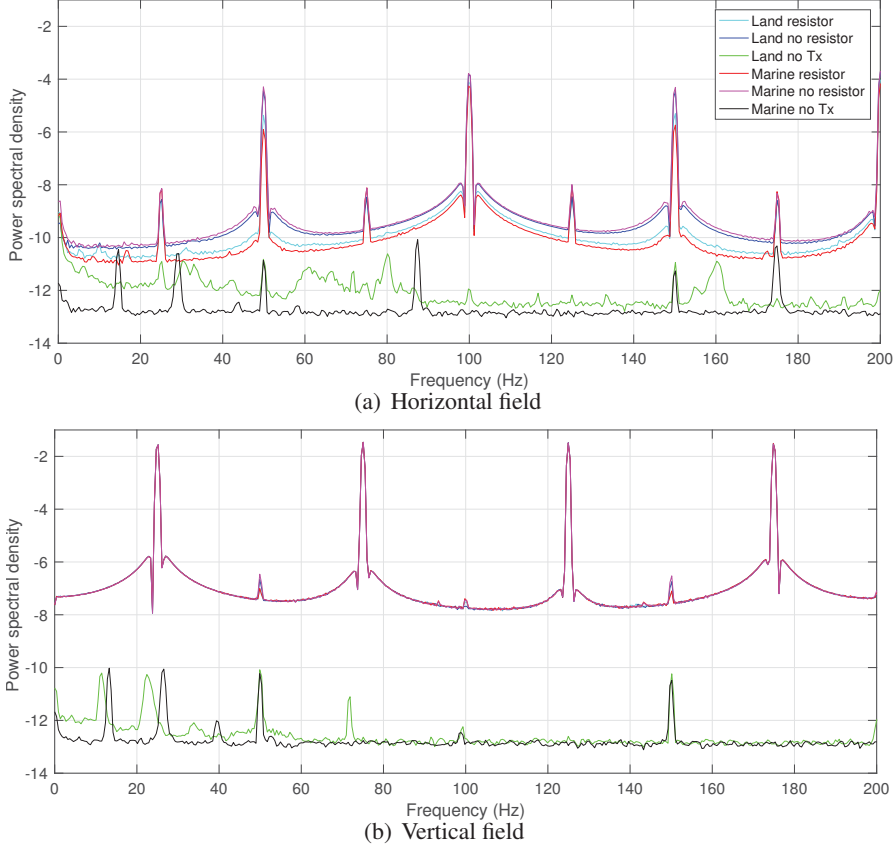
Figure 41: Power spectral density in the horizontal (a) and vertical (b) directions for receiver coil at the center of a transmitter loop with and without a damping resistor on-land and in sea-water. Also shown are the power spectral densities for the coil in land and in sea-water with no transmitter present.

of the primary field with increased lateral distance from the transmitter. This effect was considerably diminished when accounting for the exponential rise time of a transmitter loop (Fig. 14(c) & (d)). To confirm these theoretical predictions we collected one minute of flux-gate data in the center of the loop and at 1 m lateral offset distances out to 6 m away from the loop both underwater and on land. In all cases the transmitter was operated at 25 Hz base-frequency at 50% duty cycle and approximately 2.6 A of current[5]. The flux-gate dynamic range was exceeded for the center loop and 1 m lateral offset distances so these were excluded from the plots in Fig. 43. As was found in Sec. 3.5 the primary field dispersion increases with increasing lateral offset in the conductive underwater environment but remains virtually unchanged in the terrestrial environment. For the in-water measurements, even at the maximum lateral offset distance of 6 m, the effect on the transmitter on-time is marginal, with the largest impact occurring during the rapid shut-off of the primary field at the end of the transmit cycle. In most UXO detection scenarios, the transmitter, receiver and object would typically be within several meters of each other and we conclude that the primary field dispersion is not an important practical consideration.

---

[5]We used this low value of current to minimize the range where the flux-gate dynamic range was exceeded

(a) Horizontal field

(b) Vertical field
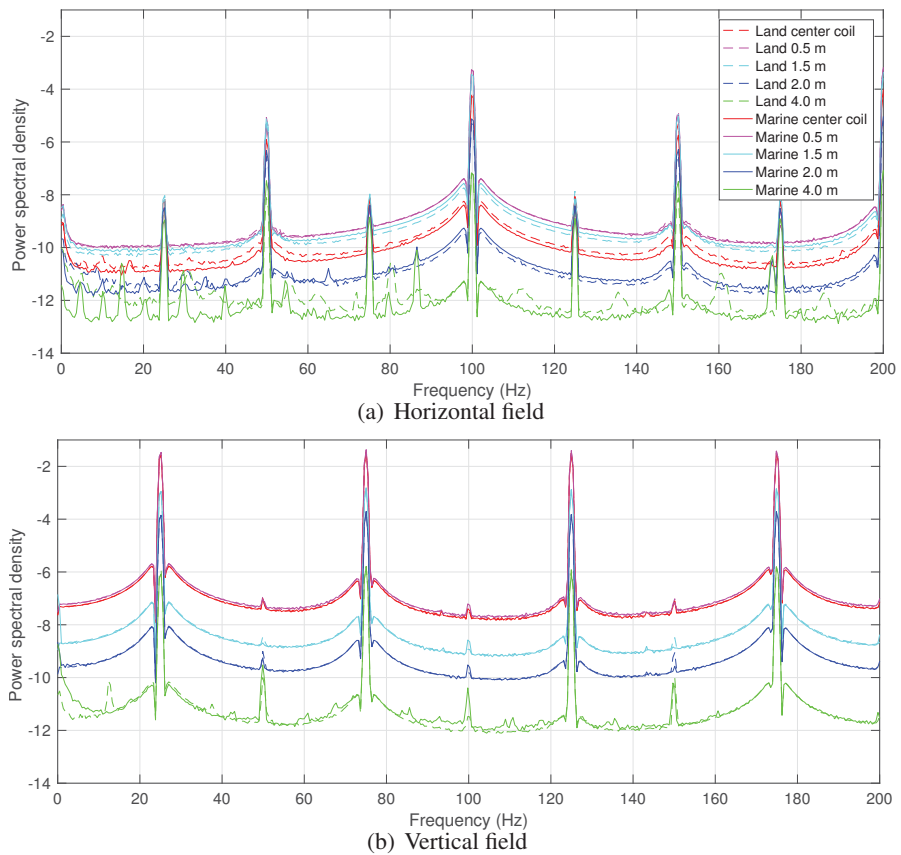
Figure 42: Power spectral density for the same offset locations as Fig 40.
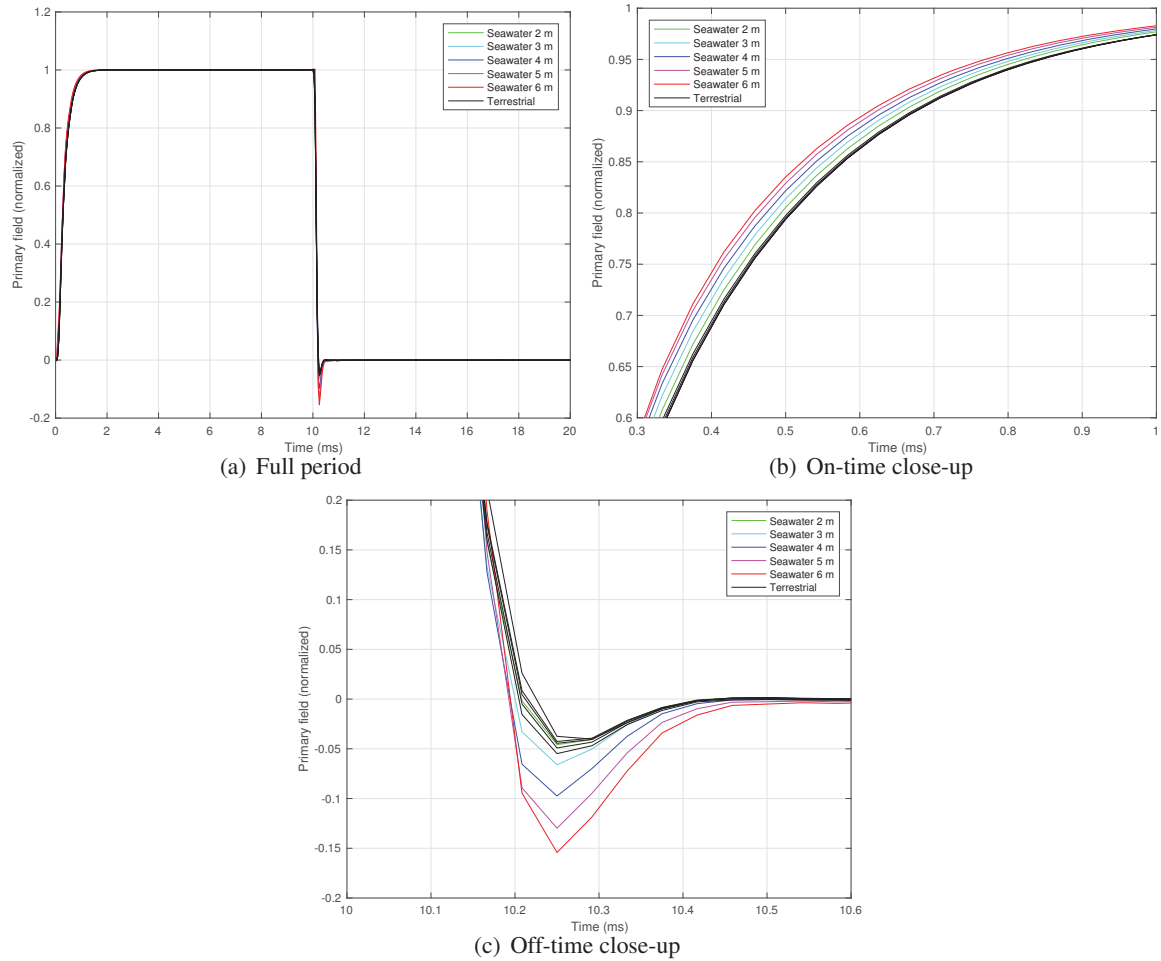
Figure 43: Normalized magnetic field recorded over (a) one full period of a 25 Hz 50% duty cycle transmitter waveform on land and in water at lateral offset distances of 2, 3, 4, 5 and 6 m both underwater (colored lines) and on land (black lines). All terrestrial measurements are shown with the same color as they are almost identical. (b) is a close-up of the on-time waveform and (c) shows the early off-time.

6   Conclusions

In this report, we adapted the integral equation approach to calculate EMI responses of the background and scattered objects in a marine setting. In the formulation, underwater environments are treated as a three-layer conducting medium that consists of the air, the sea, and the ground. A highly conducting and permeable sphere, which has EMI scattering properties expressed analytically in the frequency domain, is used as a buried target in sea sediments. The transient fields are obtained by digital filtering techniques over the harmonic fields for either dipole or loop transmitters and receivers. A range of synthetic experiments were conducted with respect to various factors that might influence the background and scattered responses, including the sea depth, the size of a loop, offset, host conductivity, excitation waveforms and receiver and transmitter insulation. These simulation studies were augmented by a number of measurements using a custom built fibreglass frame with a 2 m $\times$ 1 m transmitter loop and two receiver cubes.

We can summarize the main conclusions of this report as follows:

1) *Effect of sea-depth.* Simulation studies and measurements showed that the background response in a shallow sea decay faster than in a deep sea (water depth 50 m or more). In a deep sea where the sensor is far away from the air-sea interface, the corresponding background responses asymptotically approaches the response of a half-space. Observed decay rates were between $t^{-5/2}$ and t^{-3} depending on water depth.

2) *Effect of conductive environment on scattered response.* We found that dispersion effects due to conductivity and any current channel response, were more important at early times and large receiver to object distances. However, within the interesting time range of 0.1 ms - 25 ms, the CCR contributes little to the target signals and thus can be ignored. At times beyond several hundred microseconds, the ECR response approaches the value for the same object embedded in free space.

3) *Transmitter geometry and receiver position.* The background responses measured inside and outside of a transmitter loop are very similar and at later times vary little with offset distance from the transmitter center. A large transmitter loop can excite a strong scattered response from a buried object but also induces a larger background response. Due the small variation of the background response with position, a number of different background suppression methods can be applied to make measurements with large loops feasible. Receivers distributed with radial symmetry around the transmitter loop experience exactly the same background field from the conductive sea-water. Thus differential measurements are one way to effectively suppress the response of the seawater.

4) *Field dispersion.* Increasing host conductivity and offset distances increases dispersion of the primary field. But for our typical sensing range within 1 or 2 m, the on-time dispersion virtually disappears by the end of the on-time for pulse width as short as 1 ms. This means the on-time field dispersion is unlikely to be of concern for practical UXO sensing. Results with a simulated marine TEMTADS system showed that the scattered responses excited from a long pulse of 10 ms are stronger than those from a short pulse of 1 ms in particular for late times. This demonstrates one method to further enhance target signals, which is equally effective and equivalent in the terrestrial realm.

5) *Inversion tests.* Tests with simulated marine TEMTADS data showed that a terrestrial dipole polarizability model could be used to successfully characterize the scattered data from a buried metallic object in the conducting underwater environment.

6) *Insulation of transmitter and receiver.* Our preliminary numerical investigation showed that any insulation of the transmitter or receiver will have negligible effect on marine UXO sensing (assuming the transmitter loop has been adequately damped).

7) *Noise and spectral measurements.* Underwater measurements with no transmitter present were lower noise across most of the frequency spectrum compared to the on-land measurements. When the transmitter was operating and sufficiently damped by a resistor, the spectrum and off-time behaviour on land and in water were virtually identical. From these results we can conclude that there are no significant differences between on-land and in-water sensing from the perspective of the frequency content of the noise and signal.

6.1 Future research directions

Based on the results of this limited scope project, we conclude that underwater detection and characterization of buried metal using EMI based sensor is feasible. While the conductive sea-water introduces complications to the measurement process, there are numerous practical options for mitigation of these effects. The conductive sea-water can impact the scattered field from a buried metallic object, but typically only at very early times and at large receiver to object offsets. Neither of these conditions are commonly encountered in practice. Thus apart from the practical considerations of operating underwater, the modelling techniques and methods that have been successfully demonstrated in terrestrial environments can be utilized for marine detection and characterization.

Once we had obtained an understanding of the impact of the marine environment on detection and characterization of buried munitions, the original intent of this project was to apply that knowledge to the processing and interpretation of marine data collected by other groups sponsored by SERDP and ESTCP. However, the relevant hardware based projects have been delayed or cancelled and we have not yet obtained any data from other projects. We expect that once good quality marine data are available that additional research challenges will arise. At this stage we believe that the main challenges associated with practical use of EMI sensing to the underwater environment are centered around the logistics of operating a sensor underwater in close proximity to the sea-bottom. Specific challenges to address include:

1) Deploying the EMI system so that it remains within about 1 m of the sea-bottom.

2) Maintaining good detection performance at large standoffs in the presence of conductive sea-water. This will require the use of larger transmitter loops which in turn cause a large conductive response from the sea-water. Either differential measurements or other background subtraction methods would be required for background subtraction.

3) Accurately positioning the EMI system across a wide range of water depths and subsurface conditions where existing methods based on layback calculations or Ultra Short Baseline (USBL) acoustics are not always accurate.

4) For operation in a cued mode, there are significant challenges associated with relocating the anomaly of interest, and physically positioning and holding the sensor over the correct location for the duration of the measurements.

As with the terrestrial environment a range of different configurations of sensors will be required to address the wide range of marine conditions that can be encountered.

References

W. L. Anderson. Fast hankel transforms using related and lagged convolutions. *ACM Transactions on Mathematical Software*, 8:344–368, 1982.

G. B. Arfken and H. J. Weber. *Mathematical methods for physicists*. San Diego: Academic Press, 1995.

B. Barrow and H. H. Nelson. Model-based characterization of electromagnetic induction signatures obtained with the MTADS electromagnetic array. *IEEE Trans. Geoscience and Remote Sensing*, 39 (6):1279–1285, 2001.

T. Bell, B. Barrow, D. Steinhurst, G. Harbaugh, C. Friedrichs, and G. Massey. Empirical investigation of the factors influencing marine applications of EMI. Technical report, 2016.

T. H. Bell, B. J. Barrow, and J. T. Miller. Subsurface discrimination using electromagnetic induction sensors. *IEEE Trans. Geoscience and Remote Sensing*, 39(6):1286–1293, 2001.

L. Beran, B. Zelt, L. R. Pasion, S. D. Billings, K. Kingdon, N. Lhomme, L.-P. Song, and D. W. Oldenburg. Practical strategies for classification of unexploded ordnance. *Geophysics*, 78(1):E41–E46, 2013.

S. D. Billings, L. R. Pasion, L. Beran, N. Lhomme, L.-P. Song, D. W. Oldenburg, K. Kingdon, D. Sinex, and J. Jacobson. Unexploded ordnance discrimination using magnetic and electromagnetic sensors: Case study from a former military site. *Geophysics*, 75(3):B103–B114, 2010.

L. Carin, H. Yu, Y. Dalichaouch, A.R. Perry, P.V. Czipott, and C.E. Baum. On the wideband EMI response of a rotationally symmetric permeable and conducting target. *IEEE Trans. Geoscience and Remote Sensing*, 39(6):1206–1213, 2001.

A. D. Chave, S. Constable, and R.N. Edwards. Electrical exploration methods in applied geophysics. *Electrical Exploration Methods for the Seafloor*, 2:Chapter 12, 1991.

W. C. Chew. *Waves and Fields in Inhomogenous Media*. Wiley-IEEE Press., 1999.

Y. Das, J. McFee, J. Toews, and G. Stuart. Analysis of an electromagnetic induction detector for real-time localization of buried objects. *IEEE Trans. Geoscience and Remote Sensing*, 28:278–287, 1990.

C.G. Farquharson, K. Duckworth, and D.W. Oldenburg. Comparison of integral equation and physical scale modelling of the electromagnetic responses of models with large conductivity contrasts. *GEOPHYSICS*, 71(4):G169G177, 2006.

Erika Gasperikova, J. Torquil Smith, H Frank Morrison, Alex Becker, and Karl Kappler. UXO detection and identification based on intrinsic target polarizabilities. a case history. *Geophysics*, 74(1): B1–B8, 2008.

F. S. Grant and G. F. West. *Interpretation Theory in Applied Geophysics*. McGraw-Hill Inc., 1965.

Roger F. Harrington. *Time-Harmonic Electromagnetic Fields*. Wiley-IEEE Press, 2001.

S. Keenan, Young J. A., C. P. Foley, and Du. J. A high-tc flip-chip squid gradiometer for mobile underwater magnetic sensing. *Superconductor Science and Technology*, 23(2):025029, 2010.

J. T. Miller, T. Bell, J. Soukup, and D. Keiswetter. Simple phenomenological models for wideband frequency-domain electromagnetic induction. *IEEE Trans. Geoscience and Remote Sensing*, 39(6): 1294–1298, 2001.

M. N Nabighian. Quasi-static transient response of a conducting half-space- an approximate representation. *Geophysics*, 44:1700–1705, 1979.

G. A. Newman, Hohmann G. W., and Anderson W. L. Transient electromagnetic response of a three-dimensional body in a layered earth. *Geophysics*, 51(8):1608–1627, 1986.

S. J. Norton, SanFilipo W. A., and Won I. J. Eddy-current and current-channeling response to spheroidal anomalies. *IEEE Transactions On Geoscience And Remote Sensing*, 43(10):2200–2209, 2005.

L. Pasion and D. W. Oldenburg. A discrimination algorithm for UXO using time domain electromagnetics. *J. Eng. Environ. Geophys.*, 28:91–102, 2001.

L. R. Pasion. Inversion of time domain electromagnetic data for the detection of unexploded ordnance. *Ph.D dissertation, The University of Bristish Columbia*, 2007.

A. Schwartz and E. Brandenburg. An overview of underwater technologies for operations involving underwater munitions. *Marine Technology Society Journal*, 43(4):62–75, 2009.

SERDP-Workshop. On acoustic detection and classification of UXO in the underwater environment. Technical report, 2013.

F. Shubitidze. EMI modeling for UXO detection and discrimination underwater. Technical report, 2011.

F. Shubitidze, K. O'Neill, S.A. Haider, K. Sun, and K.D. Paulsen. Application of the method of auxiliary sources to the wideband electromagnetic induction problem. *IEEE Trans. Geoscience and Remote Sensing*, 40(4):928–942, 2002.

F. Shubitidze, K. O'Neill, K. Sun, I. Shamatava, and K.D. Paulsen. A hybrid full mas and combined mas/tsa algorithm for electromagnetic induction problems sensing. *Applied Computational Electromagnetic Society Journal*, 19(1b):112–127, 2004.

F. Shubitidze, B. Barrowes, I. Shamatavaa, J. P. Fernandez, and K. ONeilla. Underwater UXO detection and discrimination: Understanding EMI scattering phenomena in a conducting environment. *SPIE*, 2008.

F. Shubitidze, B. Barrowes, I. Shamatava, J. P. Fernandez, and K. O'Neill. Underwater UXO discrimination studies: adapting EMI forward models to marine environments. *SPIE*, 7303, 2009.

J.T. Smith, H. F. Morrison, and A. Becker. Resolution depths for some transmitter-receiver configurations. *IEEE Trans. Geoscience and Remote Sensing*, 42(6):1215–1221, 2004.

L.-P. Song and Q. H. Liu. A new approximation to three-dimensional electromagnetic scattering. *IEEE Geoscience And Remote Sensing Letters*, 2(2):238–242, 2005.

L.-P. Song, F. Shubitidze, L. R. Pasion, D. W. Oldenburg, and S. D. Billings. Computing transient electromagnetic responses of a metallic object using a spheroidal excitation approach. *IEEE Geoscience and Remote Sensing Letters*, 5(3):359–363, 2008.

L.-P. Song, Leonard R. Pasion, Stephen D. Billings, and Douglas W. Oldenburg. Non-linear inversion for multiple objects in transient electromagnetic induction sensing of unexploded ordnance: Technique and applications. *IEEE Trans. Geoscience and Remote Sensing*, 49(10):4007–4020, 2011.

L.-P. Song, S. D. Billings, L. R. Pasion, and Douglas W. Oldenburg. Transient electromagnetic scattering of a metallic object buried in underwater sediments. *IEEE Trans. Geoscience and Remote Sensing*, 54(2):1091–1102, 2016.

J. R. Wait. A conducting sphere in a time-varying magnetic field. *Geophysics*, 16:666, 1951.

J. R. Wait. The magnetic dipole antenna immersed in a conducting medium. *PROCEEDINGS OF THE I.R.E.*, pages 1244–1245, 1952.

J. R. Wait. A transient magnetic dipole source in a dissipative medium. *Journal of Applied Physics*, 24(3):341–343, 1953.

J. R. Wait. *Electromagnetic Waves in Stratified Media*. Pergamon Press, 1970.

J. R. Wait. *Geo-electromagnetism*. New York, Academic Press, 1982.

P. E. Wannamaker, Hohmann, G. W., and SanFilipo W. A. Electromagnetic modeling of three-dimensional bodies in layered earths using integral equations. *Geophysics*, 49:60–74, 1984.

S. H. Ward. unique determination of conductivity, susceptibility, size, and depth in multifrequency electromagnetic exploration. *geophysics*, XXIV(3):531–546, 1959.

S. H. Ward and G. W. Hohmann. *Electromagnetic Theory for Geophysical Applications*, volume 1. Society of Exploration Geophysicists, Tulsa, Oklahoma, 1988.

Publication:

Song, L.-P., S. D. Billings, L. R. Pasion, and Douglas W. Oldenburg, Transient electromagnetic scattering of a metallic object buried in underwater sediments, IEEE Trans. Geoscience and Remote Sensing, 54 (2), 1091-1102, 2016